1. Astronomical Photometry at Wavelengths of 8.5, 10.5 and 11.6 μm

2. Infrared Emission from Asteroids at Wavelengths of 8.5, 10.5 and 11.6 μm

Thesis by

Dennis Ludwig Matson

In Partial Fulfillment of the Requirements

For the Degree of

Doctor of Philosophy

California Institute of Technology

Pasadena, California

1972

(Submitted October 29, 1971)

To my parents for their love and

help throughout my education

ACKNOWLEDGEMENTS

It is a pleasure to thank Dr. Bruce C. Murray, my thesis and research adviser, for suggesting that infrared observations of asteroids would be an interesting and productive line of research. I am indebted to him for his aid and well-timed encouragement and optimism which largely carried this project through its dark periods.

Dr. Andrew Ingersoll has given willingly of his time in the course of many discussions and critical evaluation of several generations of thesis drafts. I thank Dr. Gerry Neugebauer and Dr. Eric E. Becklin for providing constructive criticism and good advice, and for discovering important photometric errors in the first draft of Part1. I am greatful for their continued interest in this project.

I am indebted to my colleagues, Dr. Joe Veverka and Dr. David A. Allen, for many helpful discussions and knowledgeable comments. They also did the writer great service through their meticulous reviews of the penultimate draft of this thesis.

Over the past years I have profited from Professors James A. Westphal and Eugene M. Shoemaker who have provided intellectual stimulation and have helped to review and discuss important steps of this research. I also thank Professor Westphal for evaluation and constructive criticism of several previous drafts of this thesis.

I thank Mr. Justin J. Rennilson and Dr. Henry Holt for conversations. Dr. Holt has also graciously made his unpublished data available to me. Dr. Brian G. Marsden and Dr. Joachim Schubart helped by giving their evaluation of errors likely to be involved in some of the mass determinations. I also acknowledge productive discussions with Dr. Clark Chapman, Dr. Torrence Johnson, Dr. Duane Muhleman, Dr. Hugh H. Kieffer and Dr. Donald S. Burnett.

Dr. Kieffer also kindly made his computer program available to me. Dr. Paul Herget in Cincinnati, and Dr. S. G. Makover in Leningrad, have assisted by providing ephemerides.

I acknowledge profitable conversations with Dr. Deane M. Peterson, Dr. Frank Low, Dr. Gido Münch and Mr. Robert D. Gehrz. Also, discussions with Dr. Thomas B. McCord, Dr. J. Beverley Oke, Dr. Martin Schmidt and Mr. Carl Vesely were useful.

I have incurred a number of special debts during the instrument construction and observation phases of this thesis. The considerable talent and energy of Mr. Sol Giles were in large part responsible for the design and building of the instrumentation. I am greatful to Mr. Victor Nenow and Mr. Devere Smith for assistance with the electronic instrumentation. Mr. Gordon Hoover participated in the equipment building and assisted with all of the telescope observations. Thanks goes to the Hale Observatories Astroelectronics Laboratory for their assistance with equipment set-up on Mt. Wilson and for the loan of a voltage-to-frequency converter. I thank Dr. Arthur Vaughan, Mr. Thomas Cragg,

Mr. Larry Bornhurst and the staff of the Mt. Wilson Observatory for aid at the telescope and for the many courtesies that they rendered. I thank my sister Dorothy for typing rough and intermediate drafts for this thesis.

This research was supported by the National Aeronautics and Space Administration Grant NGL 05-002-003. The observing time with the Mt. Wilson 60-inch telescope was provided by the Hale Observatories.

ABSTRACT

The purpose of this thesis is to present new observations of thermal-infrared radiation from asteroids. Stellar photometry was performed to provide standards for comparison with the asteroid data. The details of the photometry and the data reduction are discussed in Part 1. A system of standard stars is derived for wavelengths of 8.5, 10.5 and 11.6 μm and a new calibration is adopted. Sources of error are evaluated and comparisons are made with the data of other observers.

The observations and analysis of the thermal-emission observations of asteroids are presented in Part 2. Thermal-emission lightcurve and phase effect data are considered. Special color diagrams are introduced to display the observational data. These diagrams are free of any model-dependent assumptions and show that asteroids differ in their surface properties.

On the basis of photometric models, (4) Vesta is thought to have a bolometric Bond albedo of about 0.1, an emissivity greater than 0.7 and a true radius that is close to the model value of 300^{+50}_{-30} km. Model albedos and model radii are given for asteroids 1, 2, 4, 5, 6, 7, 15, 19, 20, 27, 39, 44, 68, 80, 324 and 674. The asteroid (324) Bamberga is extremely dark with a model (~bolometric Bond) albedo in the 0.01 - 0.02 range, which is thought to be the lowest albedo yet measured for any solar-system body. The crucial question about such low-albedo asteroids is their number and the distribution of their orbits.

TABLE OF CONTENTS

TABLE OF CONTENTS

TABLE OF CONTENTS

LIST OF ILLUSTRATIONS

PART 1

PART 2

LIST OF ILLUSTRATIONS

PART 2 (Contd) Page

LIST OF ILLUSTRATIONS

PART 2 (Contd)

APPENDIX II

LIST OF ILLUSTRATIONS

LIST OF TABLES

LIST OF TABLES

PART 1. ASTRONOMICAL PHOTOMETRY AT WAVELENGTHS OF 8.5, 10.5 and 11.6 μm

1. INTRODUCTION

The first half of this thesis develops the stellar photometry system which is used later, in Part 2, to measure radiation from asteroids. Here the observations of five stars (α Boo, μ Cep, α Her, α Tau and α Ori) are reduced to form a set of standards. The methods of data reduction are discussed in detail and a new calibration is introduced. Finally, this part concludes with an account of how sources of unknown irradiance are measured with respect to the standards.

Other narrow band photometry in the 8-14 μm region for these same stars is already available in the literature (Gehrz and Woolf 1971, Gillett et al 1971). The bandpasses used here differ slightly from those of the above authors and, in principle, the standards must be determined anew because some of these stars have spectral features at wavelengths of 8-14 μm.

In the following Beer's Law is found to adequately describe the terrestrial atmospheric extinction. The relative irradiances assigned to the standards are consistent at about the ten to twenty percent level with the results obtained by other observers. A new calibration is introduced. It is independent of, but in good agreement with, the commonly used value which was worked out by Johnson (1965).

II. OBSERVATIONAL METHOD

The observations were made with the Hale Observatories' 60-inch telescope on Mt. Wilson. A double-beam (sky subtraction) photometer was mounted at the telescope's f/16 cassegrain focus. The photometer beams defined two fields of view which were separated on the plane of the sky by one minute of arc. One beam was fixed to be always directly north of the other and each beam subtended a field of view 16 seconds of arc in diameter. In the photometer an optical chopper allowed the detector to alternately receive light from the two beams.

The bandpasses of the photometer are centered at 8.5, 10.5 and 11.6 μm and have widths at fifty percent transmission of 0.5, 0.5 and 1.0μm respectively. The detector is a mercury doped germanium photoconductor which is operated at a temperature of ~20°K. For photons with more than a certain threshold energy, the conductivity of the detector varies directly with the number of light quanta incident upon it. The chopping between the two fields of view, induces an alternating conductivity of an amplitude proportional to the difference in the photon flux. Appendix II describes how this signal is electronically amplified and processed. The end product is a direct current voltage signal which, within instrumental error, is directly proportional to the difference between the number of photons reaching the detector from the two beams. The output is monitored on a strip-chart recorder and is also fed to a voltage-to-pulse frequency converter. The pulses from this converter are counted electronically for fixed intervals of time in order to measure the integrated, or average voltage. Ten seconds is the length of the interval used

for all of the observations and at the end of each interval the total number of counts is printed on a paper tape.

Measurements or deflections are taken by first placing the source to be measured in one beam and counting for ten seconds. After the end of the interval the telescope is moved, and the source is placed in the other field and another ten-second integration interval is started. The difference between the two count totals, 1 and 2, is the measurement. The telescope is then returned to its initial position and the second measurement is obtained from count print-outs, 2 and 3. If the polarity of the first measurement is defined to be positive then the second measurement is negative and must be multiplied by minus one. The telescope is repositioned and the counting sequence 1-2-1-2-1....is continued until anywhere from twelve to thirty measurements have been made.

In the far-infrared great care must be taken in making these measurements in order to be sure that the background radiation from the sky and the telescope is separated from the signal. On occasion faint sources are found to have negative irradiance. This is probably due to the inclusion of small uncompensated amounts of background radiation in the measurements. Thus there are non-photometric conditions under which spurious signals can be obtained, as well as the classical non-photometric conditions under which the correct extinction corrections cannot be applied (e.g. clouds).

The matter of rejecting "anomalous" data is a subject of concern because of the risk of introducing bias. Of course, those measurements that are spurious

due to some specific and identifiable cause can be and are discarded. Perhaps the process should stop with that. However, there are things that happen to cause bad measurements, such as objects (e.g. birds), passing through the fields of view, electrical transients and other things. Although the cause cannot be identified in each instance, it is desirable to mitigate the effect of the large errors so as not to completely upset the observations during which they occur. Concomitantly, it is realized that rejection of outlying values is at the expense of some good data.

The adopted criterion is first to reject deflections more than three standard deviations from the mean and then to re-compute the mean and discard those at a distance of more than two standard deviations. The result is that from a total of 16,230 deflections, 63 are discarded by the first step and 654 are removed by the second. In all, 4.42% are rejected and, by way of comparison, a two-standard-deviation criterion applied to a gaussian distribution would reject 4.54%. It would seem that the number of data rejected is not excessive. For a typical observation of twenty deflections this means that slightly less than one deflection is thrown away.

III. STANDARD STARS

Now observations of α Tau, α Ori, α Boo, μ Cep and α Her are to be reduced to form a standard star system. The problems of atmospheric extinction and of the accuracy of the standards will be discussed.

A. Atmospheric Extinction

The correction of observations for the effects of extinction by the Earth's atmosphere is a very complicated and difficult problem, inasmuch as several different effects occur simultaneously. The vast amount of observational and theoretical studies in the literature are reviewed by Plass and Yates (1965) and the reader is referred to that reference for discussion. Here the problem of correcting data for extinction is treated empirically.

On the best photometric nights the dependence of extinction upon airmass is obvious. Some of the best data are shown in Fig. 1. Beer's Law is:

$$E = E_o \exp(-kx) \qquad (1)$$

E = observed irradiance
E_o = irradiance above the Earth's atmosphere
k = extinction coefficient
x = path length in airmass units

It adequately describes the data in Fig. 1 to an accuracy of better than one percent. In making nominal corrections of the observations, values of $k = 0.25$, 0.10 and 0.04 are used for the bandpasses at 8.5, 10.5 and 11.6 μm respectively. These values are used because it is thought that they are typical for average nights. The error introduced by any difference, Δk, between the true and the adopted values of k can easily be estimated. Accordingly, for the ratio of two extra-terrestrial irradiances, one obtains from Eqn. 1:

Fig. 1. Comparison of some of the best data with Beer's Law. The ordinate is in counts which correspond to the instrumental response. The curves are fit to the data by the method of least squares. All observations except one are within one percent of the curves. The "spurious observation" was rejected because of its large internal standard deviation which was taken as an indication of lack of good agreement among the measurements comprising the observation. Since several causes for such erroneous data are known there is no special reason to regard this observation as an improbable statistical event. The values observed for k on these nights do not necessarily correspond to values that are typical for an average night.

Fig. 1.

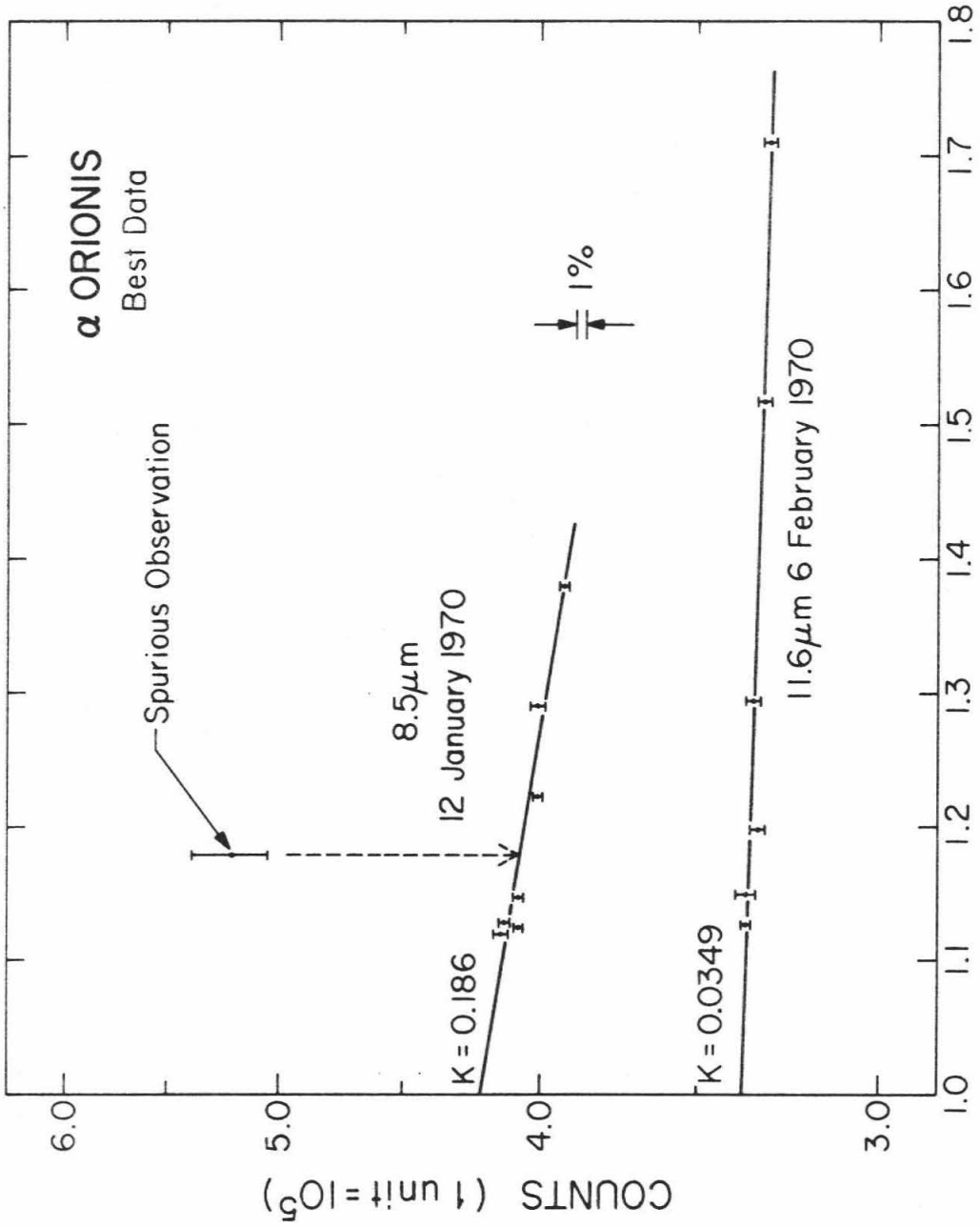
α ORIONIS
Best Data
Spurious Observation
8.5μm
12 January 1970
K = 0.186
11.6μm 6 February 1970
K = 0.0349
± 1%
COUNTS (1 unit = 10⁵)
AIR MASS
6.0
5.0
4.0
3.0
1.0
1.1
1.2
1.3
1.4
1.5
1.6
1.7
1.8

$$\frac{E'_o}{E_o} = \frac{E'}{E} \exp\,(k(x'-x)) \tag{2}$$

and

$$\Delta\left(\frac{E'_o}{E_o}\right) = \frac{d\left(\frac{E'_o}{E_o}\right)}{dk} \cdot \Delta k. \tag{3}$$

$$= (x'-x)\frac{E'}{E} \exp\,(k(x'-x)) \cdot \Delta k. \tag{4}$$

The estimated error is

$$\text{Extinction error} \sim \frac{\Delta\left(\frac{E'_o}{E_o}\right)}{\frac{E'_o}{E_o}} = (x'-x) \cdot \Delta k \tag{5}$$

or

$$\sim 5\% \tag{6}$$

when one uses values of $(x'-x) = 0.5$ and $\Delta k = 0.1$.

The results of the application of this type of nominal extinction correction on several typical nights are shown in Figs. 2 and 3.

B. Irradiance Ratios

For each night's data, the mean and the standard deviation are calculated from the extinction-corrected observations of each star. The irradiance ratios between the various stars are formed using the mean values. The errors for these ratios are taken as the larger of either the formal error or five percent of the ratio itself. The arbitrary five percent is used because it is believed that this is the limit for accuracy on typical nights. If a star is observed only once, then the mean and

Fig. 2. Data for April 3, 1970 after the nominal corrections have been made for extinction. The ordinate is the instrumental response measured in thousands of counts.

Fig. 2.

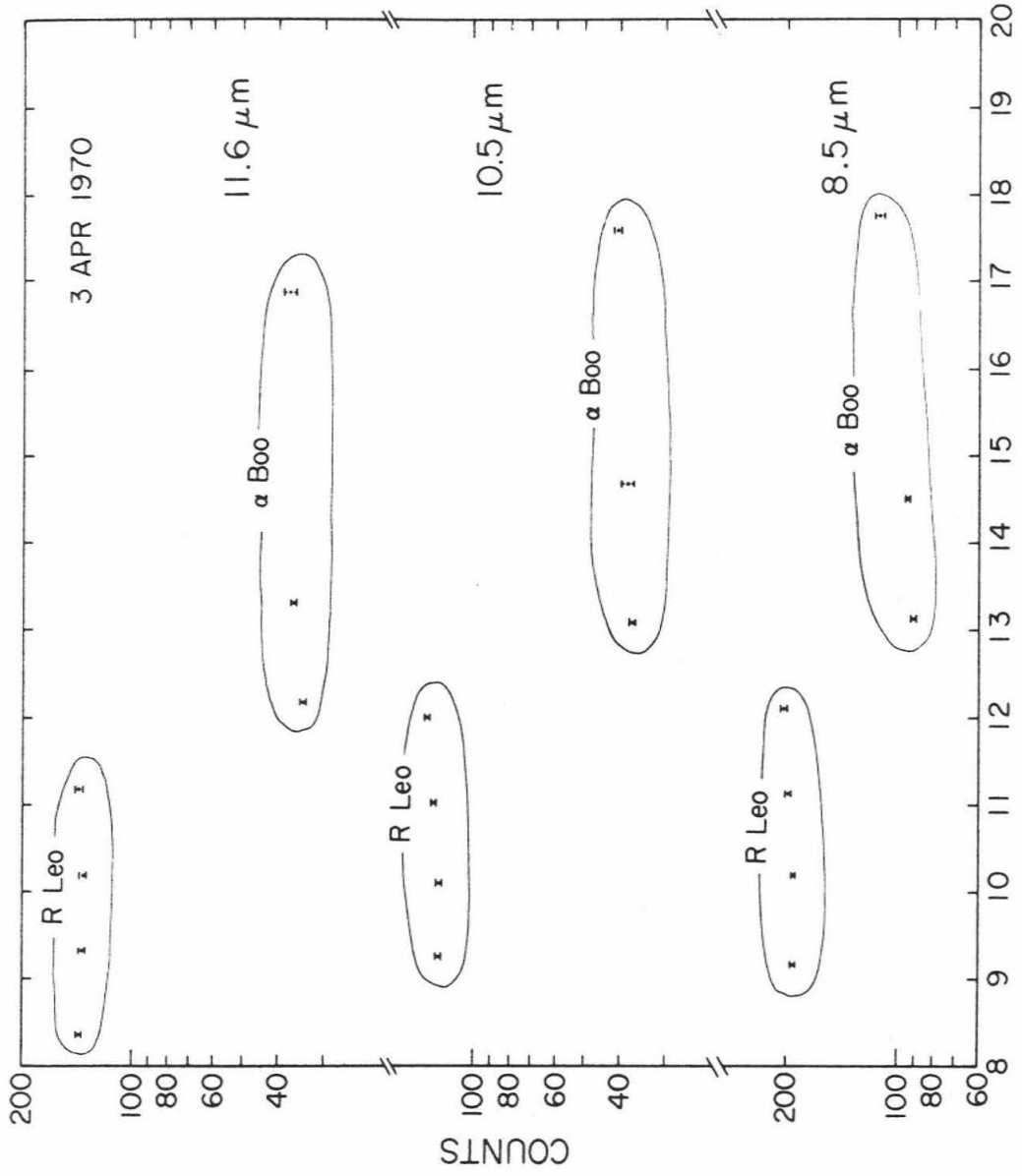
3 APR 1970
11.6 μm
10.5 μm
8.5 μm
α Boo
R Leo
COUNTS
L.S.T.
200
100
80
60
40
8
9
10
11
12
13
14
15
16
17
18
19
20

Fig. 3. Data for July 26, 1970 after the nominal corrections have been made for extinction. The ordinate is the instrumental response measured in thousands of counts.

Fig. 3.

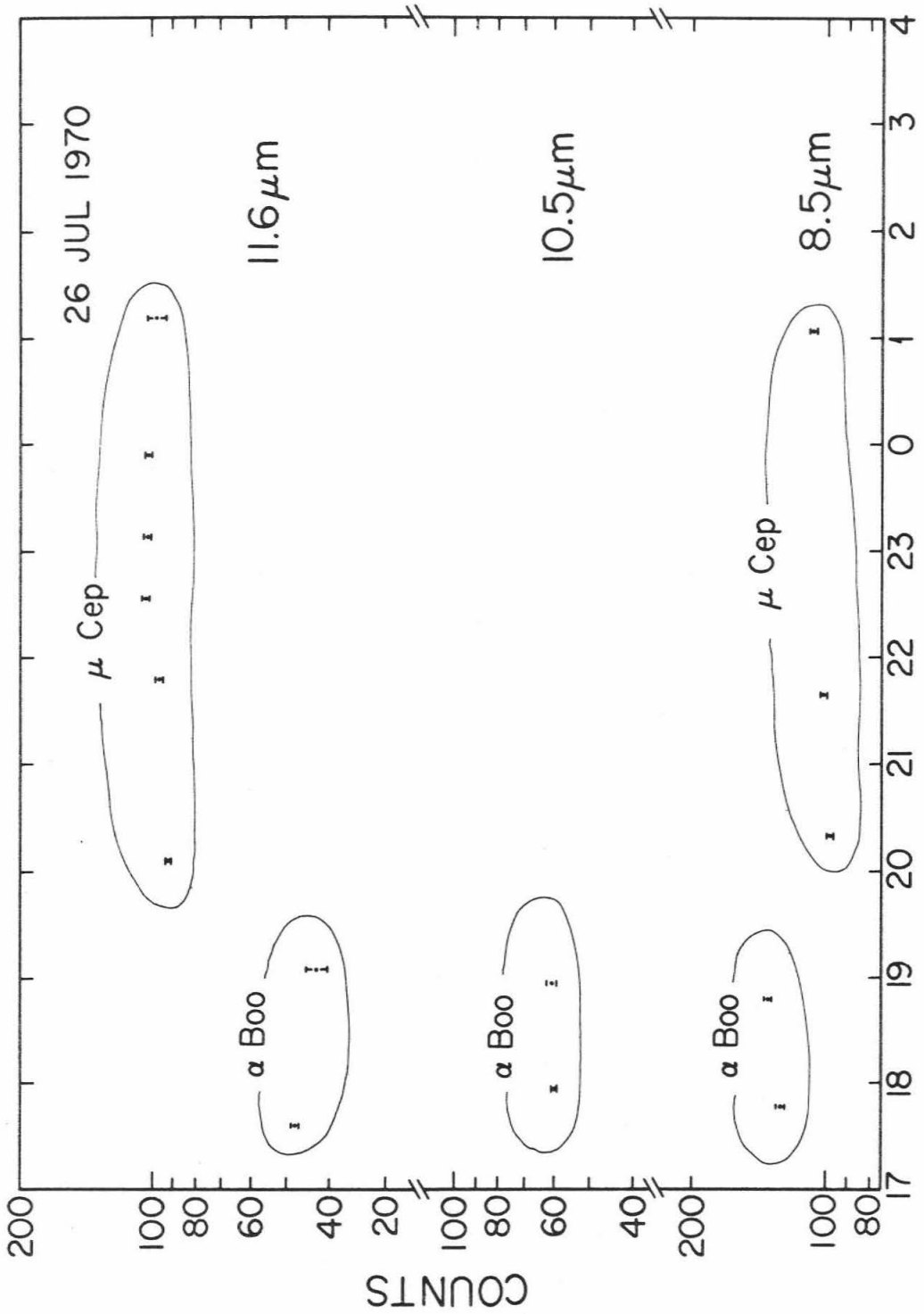
26 JUL 1970
11.6μm
10.5μm
8.5μm
μ Cep
α Boo
COUNTS
L.S.T.
200
100
80
60
40
20
17
18
19
20
21
22
23
0
1
2
3
4

the standard deviation of the mean, as formally computed from the deflections of the observation, are used. On the whole, the ratios are found to repeat from night-to-night to roughly ten percent precision. The ratios and the assigned errors are listed in Tables 1-3.

The adopted values for the ratios are the averages of the nightly values with double weight assigned to the data from nights on which both stars of a ratio are observed more than once. The final standard deviations are set to be the larger value of either the formally propagated standard deviation or ten percent of the ratio. The ten percent lower limit for the standard deviation is chosen because this is approximately the precision to which the most frequently (and therefore best) observed ratios repeat.

One way to test the adopted irradiance ratios is to compute products of the form:

$$\frac{\text{Star A}}{\text{Star B}} \cdot \frac{\text{Star B}}{\text{Star C}} \cdot \frac{\text{Star C}}{\text{Star A}} = 1. \qquad (7)$$

All of the ratios can be obtained directly from the data and the closeness to unity of Eqn 7 is a measure of the internal consistency. Table 4 tabulates the appropriate three star products. With two exceptions, products with the ratios involving α Boo and μ Cep vary five percent or less from unity. Other ratios easily approach to within ten percent of unity.

A second test involves comparison of the adopted ratios with the photometry of Gillett et al (1971) and Gehrz and Woolf (1971). The published magnitudes for

TABLE I. 11.6 μm IRRADIANCE RATIOS

Date	μ Cep / α Boo	α Ori / α Boo	α Tau / α Boo	α Her / α Boo
(1969)				
Aug. 23	1.93±0.10			1.91±0.18
24				
25				
26				
Sept. 17				
18				
Oct. 11				
Nov. 30				
Dec. 3				
(1970)				
Jan. 12				
Feb. 6		7.95±0.40*	0.893±0.045*	2.18±0.17*
7		9.81±0.49	0.846±0.054*	
Apr. 1		10.4 ±1.2		2.32±0.32*
2	2.31±0.28	8.63±1.04*	0.951±0.117	2.18±0.27*
3		8.05±0.46		
4	2.75±0.14			2.29±0.11
Jul. 24	2.13±0.20		0.988±0.074	
25	2.21±0.11*			
26	2.18±0.19*			
27				
ACCEPTED VALUES	2.24±0.24	8.78±1.01	0.903±0.09	2.23±0.22

* Double weight

TABLE 2. 10.5 μm IRRADIANCE RATIOS

Date	$\frac{\mu \text{ Cep}}{\alpha \text{ Boo}}$	$\frac{\alpha \text{ Ori}}{\alpha \text{ Boo}}$	$\frac{\alpha \text{ Tau}}{\alpha \text{ Boo}}$	$\frac{\alpha \text{ Her}}{\alpha \text{ Boo}}$
(1969)				
Aug. 23	2.63±0.16			2.09 ± 0.11
24	2.77± 0.23			2.06±0.15
25				
26				
Sept. 17				
18				
Oct. 11				
Nov. 30				
Dec. 3				
(1970)				
Jan. 12				
Feb. 6				
7				
Apr. 1				
2				
3		8.06± 0.62		
4	2.66±0.37			
July 24	2.43± 0.25*		0.817±0.074	
25	2.62± 0.13*			
26	2.35±0.12			
27				
ACCEPTED VALUES	2.56± 0.26	8.06±0.81	0.817± 0.082	2.07±0.21

* Double Weight

TABLE 3. 8.5 μm IRRADIANCE RATIOS

Date	$\frac{\mu \text{ Cep}}{\alpha \text{ Boo}}$	$\frac{\alpha \text{ Ori}}{\alpha \text{ Boo}}$	$\frac{\alpha \text{ Tau}}{\alpha \text{ Boo}}$	$\frac{\alpha \text{ Her}}{\alpha \text{ Boo}}$
(1969)				
Aug. 23	0.871±0.044			1.69±0.08
24				
25				
26				
Sept. 17				
18				
Oct. 11				
Nov. 30				
Dec. 3				
(1970)				
Jan. 12		4.80±0.24*		
Feb. 6				
7				
Apr. 1				
2	0.837± 0.042	4.57±0.29	0.810± 0.040	1.64±0.08
3		5.07± 0.25		
4	0.910± 0.046			
July 24	0.851± 0.043*		0.794±0.040	
25	0.880± 0.044			
26	0.777± 0.047*			
27				
ACCEPTED VALUES	0.844±0.084	4.81±0.48	0.801±0.080	1.66±0.16

* Double Weight

TABLE 4. LOOP SUMMARY

Product	Bandpass 11.6 μm	8.5 μm	10.5 μm
$\frac{\mu\ \text{Cep}}{\alpha\ \text{Boo}} \cdot \frac{\alpha\ \text{Ori}}{\mu\ \text{Cep}} \cdot \frac{\alpha\ \text{Boo}}{\alpha\ \text{Ori}}$	0.97	0.96	0.97
$\frac{\mu\ \text{Cep}}{\alpha\ \text{Boo}} \cdot \frac{\alpha\ \text{Tau}}{\mu\ \text{Cep}} \cdot \frac{\alpha\ \text{Boo}}{\alpha\ \text{Tau}}$	1.08	1.00	0.98
$\frac{\mu\ \text{Cep}}{\alpha\ \text{Boo}} \cdot \frac{\alpha\ \text{Her}}{\mu\ \text{Cep}} \cdot \frac{\alpha\ \text{Boo}}{\alpha\ \text{Her}}$	0.96	0.99	0.96
$\frac{\alpha\ \text{Ori}}{\alpha\ \text{Boo}} \cdot \frac{\alpha\ \text{Tau}}{\alpha\ \text{Ori}} \cdot \frac{\alpha\ \text{Boo}}{\alpha\ \text{Tau}}$	1.05	1.06	0.87
$\frac{\alpha\ \text{Ori}}{\alpha\ \text{Boo}} \cdot \frac{\alpha\ \text{Her}}{\alpha\ \text{Ori}} \cdot \frac{\alpha\ \text{Boo}}{\alpha\ \text{Her}}$	1.03	1.04	0.92
$\frac{\alpha\ \text{Ori}}{\mu\ \text{Cep}} \cdot \frac{\alpha\ \text{Tau}}{\alpha\ \text{Ori}} \cdot \frac{\mu\ \text{Cep}}{\alpha\ \text{Tau}}$	0.94	1.02	0.86
$\frac{\alpha\ \text{Ori}}{\mu\ \text{Cep}} \cdot \frac{\alpha\ \text{Her}}{\alpha\ \text{Ori}} \cdot \frac{\mu\ \text{Cep}}{\alpha\ \text{Her}}$	1.04	1.01	0.94
$\frac{\alpha\ \text{Tau}}{\alpha\ \text{Boo}} \cdot \frac{\alpha\ \text{Her}}{\alpha\ \text{Tau}} \cdot \frac{\alpha\ \text{Boo}}{\alpha\ \text{Her}}$	0.96	1.03	0.98
$\frac{\alpha\ \text{Tau}}{\mu\ \text{Cep}} \cdot \frac{\alpha\ \text{Her}}{\alpha\ \text{Tau}} \cdot \frac{\mu\ \text{Cep}}{\alpha\ \text{Her}}$	1.08	1.04	1.01
$\frac{\alpha\ \text{Tau}}{\alpha\ \text{Ori}} \cdot \frac{\alpha\ \text{Her}}{\alpha\ \text{Tau}} \cdot \frac{\alpha\ \text{Ori}}{\alpha\ \text{Her}}$	0.98	1.05	0.93

these stars are listed in Table 5 along with the magnitudes for the present observations. The differences between the reported magnitudes are generally in the range of 10 to 20 percent. Upon inspection of this table, however, it is obvious that errors in the irradiance reported for an unknown source could differ between observers by as much as 30 percent if these stars are used as standards (e.g. μ Cep at 8.5 μm). The differences between the magnitudes assigned to two different stars can also be large. Some of these differences with respect to α Boo are shown in Fig. 4. This general level of agreement is not good compared with the (8-14μm) N-photometry. For these same stars, the Arizona and CIT N-bandpass photometries agree to within a few percent (Low 1970, Neugebauer and Becklin, private communication). Similar precision should be achievable through the narrower bandpasses; presumably this is just a matter of collecting a statistically significant number of observations. In the meantime measurements of unknown sources will suffer from more scatter than is necessary.

TABLE 5. STELLAR MAGNITUDES

		Bandpass and Reference							
		Low (1970)	Gehrz and Woolf (1971)		Gillett et al (1971)		This Work		
B.S.	Name	N	8.4μm	11μm	8.4μm	11.0μm	8.5μm	10.5μm	11.6μm
1457	α Tau	-3.11	-2.97	-2.99	-2.78	-2.97	-2.96	-3.01	-3.13
2061	α Ori	-5.25	-4.76	-5.56	-4.79	-5.51	-4.91	-5.50	-5.60
5340	α Boo	-3.28	-3.19	-3.27	-3.32	-3.24	-3.20	-3.23	-3.24
6406	α Her	-4.00	-3.80	-4.06	—	—	-3.75	-4.02	-4.11
7001	α Lyr	-0.06	-0.05	-0.03	—	—	—	—	—
8316	μ Cep	-3.61	-2.85	-4.17	-2.72	-4.03	-3.02	-4.25	-4.12

Fig. 4. Comparison between observers. The abscissa is the ratio between each star and α Boo as used in this thesis. The ordinates are the differences between these ratios and those used by other authors. Bandpasses differ slightly between observers and the wavelengths at the right margin are for this work. The 10.5 and 11.6 μm data are compared with 11.0 μm observations from other observers. The 8-14 μm data that are not plotted fall off scale. The N photometry is from Low (1970).

Fig. 4.

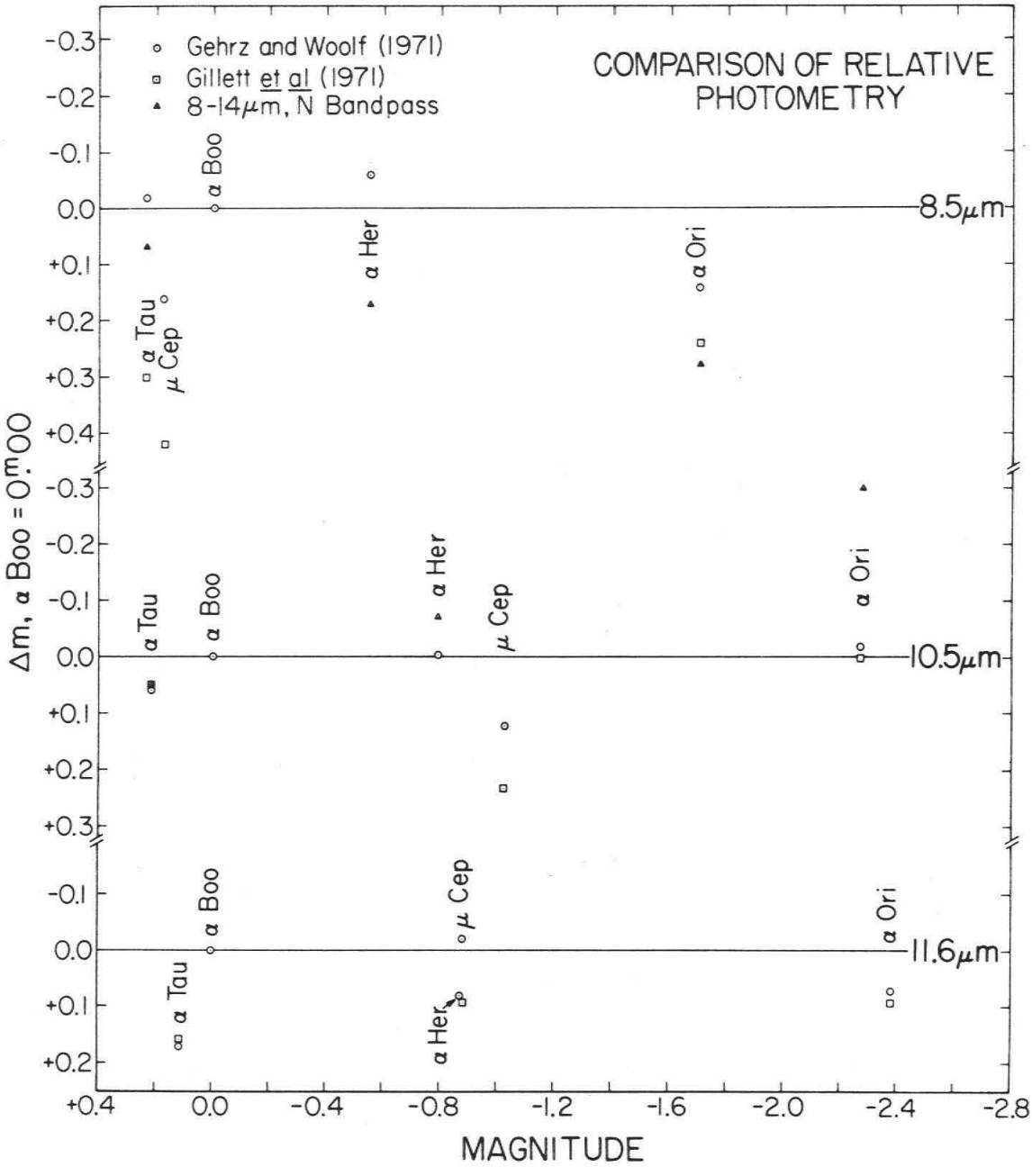
Gehrz and Woolf (1971)
Gillett et al (1971)
8-14μm, N Bandpass
COMPARISON OF RELATIVE PHOTOMETRY
8.5μm
10.5μm
11.6μm
α Boo
α Her
α Ori
α Tau
μ Cep
Δm, α Boo = 0.m00
MAGNITUDE
-0.3
-0.2
-0.1
0.0
+0.1
+0.2
+0.3
+0.4
+0.4
0.0
-0.4
-0.8
-1.2
-1.6
-2.0
-2.4
-2.8

IV CALIBRATION

The absolute irradiance of α Boo will now be derived. This derived calibration is based upon absolute, visible-wavelength measurements of α Lyr from Oke and Schild (1970), the model for Vega by Schild et al (1971), the N-magnitude of (α Lyr-α Boo) from Low (1970) and an assumed spectrum for α Boo.

Oke and Schild (1970) report their absolute spectrophotometric observations of Vega with respect to two blackbodies and a standard lamp. They give the 5480 Å spectral irradiance of α Lyr above the Earth's atmosphere as 3.53×10^{-20} erg sec^{-1} cm^{-2} Hz^{-1} (or 3.52×10^{-9} erg sec^{-1} cm^{-2} Å^{-1}) and estimate that the accuracy of this value is 2 percent. In comparing their results at $\lambda = 5556$ Å with older determinations, they find that their result is six percent lower than that of Willstrop (1965) and nine percent less than that adopted by Code (1960).

Another recent absolute calibration has been made by Hayes (1970). The differences between Hayes (1970), and Oke and Schild (1970) have been studied by Hayes, Oke and Schild (1970). They "...conclude that the two calibrations are essentially identical." (op cit p362)

The spectrum of α Lyr is assumed to be as predicted by the model of Schild et al (1971). For their model, Schild et al find that the continum flux at 12μm is formed at essentially the same optical depth as $\Delta\lambda = 1$ Å from the core of the H_α line. Upon the expectation that the uncertainty in the extrapolated flux may be of the same order as the discrepancy between the observed and computed H_α

profiles, they estimate the uncertainty in the emergent model flux at 12 μm to be ~7 percent.

The 8-14 μm spectrum of α Boo assumed to have the shape of a 4000°K blackbody. Errors in the chosen temperature are not critical. Furthermore, low resolution spectral observations from $\lambda = 7.5$ to 13 μm by Gillett et al (1968) show no significant departure of the data from this assumed shape. This is true to about the 10 or 15 percent level which is the amount of their observational scatter.

For wavelengths at 8-14 μm let the shape of the α Lyr spectrum be represented by a 10,000°K blackbody and take the difference between α Boo and Vega as -3.22 magnitudes as observed by Low (1970) in the N bandpass. This is in excellent agreement with -3.2 mag observed by Neugebauer and Becklin (private communication). Let $E(\lambda)$ represent the spectral irradiance above the atmosphere at wavelength λ; $B(\lambda,T)$ be the spectral radiant emittance at wavelength λ of a blackbody of temperature T; and let C be a constant whose value is to be determined. The prime notation denotes the quantity referring to α Lyr. The observed ratio, r, is then:

$$r = \frac{\int_8^{13.5} E(\lambda)\,d\lambda}{\int_8^{13.5} E'(\lambda)\,d\lambda} = C\,\frac{\int_8^{13.5} B(\lambda,4000)\,d\lambda}{\int_8^{13\,5} B(\lambda,10000)\,d\lambda} \qquad (8)$$

$$C = r \frac{\int_8^{13.5} B(\lambda, 10000)\, d\lambda}{\int_8^{13.5} B(\lambda, 4000)\, d\lambda} \qquad (9)$$

Equation 9 is evaluated numerically using steps of $\Delta\lambda = 0.1$ μm from 8.0 to 13.5μm. This equation is a reasonable approximation because the two spectra are very similar. The ratio $B(\lambda, 10000)/B(\lambda, 4000)$ varies by ~6 percent between the two limits. If the spectra were grossly dissimilar then Eqn. 9 would have to include the spectral sensitivity of the equipment and the atmospheric transmission.

The difference of -3.22 magnitudes corresponds to r = 19.4 and evaluation of Eqn. 9 yields C = 54.6. Now, the spectral irradiance of the two stars are related by:

$$E(\lambda) = E'(\lambda)\, C \frac{B(\lambda, 4000)}{B(\lambda, 10000)} \qquad (10)$$

The resulting spectral irradiances, $E(\lambda)$, for α Boo are 4.06, 1.81 and 1.24 $\times 10^{-15}$ W cm^{-2} μm^{-1} for 8.5, 10.5 and 11.6 μm respectively.

Now these values are to be compared with data that are available from other workers. Their magnitudes and calibrations are used to compute the absolute irradiance that they assign to α Boo.

The calibration of the N-photometry system is discussed by Johnson (1965). He bases his calibration upon absolute measurements for the Sun from Saiedy (1960) and C. W. Allen (1963); upon stellar magnitudes from Code (1960) and Stebbins and Kron (1964). As the effective wavelengths for his

bandpasses, Johnson uses,

$$\lambda_o = \frac{\int_o \lambda \varphi(\lambda)\, d\lambda}{\int_o \varphi(\lambda)\, d\lambda} \qquad (11)$$

where $\varphi(\lambda)$ is the instrumental response. Johnson obtains the color of the sun by interpolation among the available data. Using V = -26.74 as the solar magnitude, he reduces the solar data to $V = 0.^m00$, yielding the irradiance of a solar-type star with $V = 0.^m00$. Correction for the solar color of $V-N = +1.^m46$ produces 1.23×10^{-16} W cm^{-2} μm^{-1} as the absolute calibration for zero N-magnitude. His effective wavelength, $\lambda_o = 10.2\ \mu$m, and (α Lyr - α Boo) $= -3.^m22$ mag as observed by Low, yield the position of Johnson's calibration in Fig. 5.

All other previously existing calibrations either depend directly upon these results of Johnson (1965) or use the same methods and/or data that he used. Table 6 lists the other data used in Fig. 5. The details of the methods by which these values are derived are not discussed in the literature. Both Gehrz and Woolf (1971) and Gillett et al (1971) use the same calibration (Gehrz 1971, private communication). Their calibration was obtained by extrapolating the spectral shape of A-type stars to the longer wavelengths on the basis of their UBV colors. The absolute calibration of UBV was taken from Johnson (1965) and they place the accuracy of their calibration at 10 percent. The data that are tabulated and plotted for D.A. Allen are the calibrations and the magnitudes that he used for his observations of Vesta (D.A. Allen 1971, private communication).

TABLE 6. CALIBRATION DATA FOR FIGURE 5

λ (μm)	λ^{-1} (μm^{-1})	E(λ) for Zero Mag. (W cm^{-2} μm^{-1})	α Boo Magnitude	Reference
8.4	0.119	2.45×10^{-16}	-3.32	Gillett et al 1971
8.5	0.118	2.5×10^{-16}	-3.20	Allen (1971, private communication)
8.5		2.13×10^{-16}	-3.20**	Present Work
10.2*	0.098	1.23×10^{-16}	———	Johnson 1965
		———	-3.22	Low 1970
10.5	0.095	9.25×10^{-17}	-3.23**	Present Work
11.0	0.091	8.6×10^{-17}	-3.24	Gillett et al 1971
11.5*	0.087	7.2×10^{-17}	-3.22	Allen (1971, private communication)
11.6	0.086	6.24×10^{-17}	-3.24**	Present Work

*Effective Wavelength
**Adopted but not observed

Fig. 5. Nominal values for the absolute spectral irradiance of α Boo above the Earth's atmosphere. The plotted points show the irradiances currently used for this star. The curve has the shape of a 4,000°K blackbody and is included for reference only. It is set to pass through the points of the present calibration and does not involve the angular diameter of α Boo.

Fig. 5.

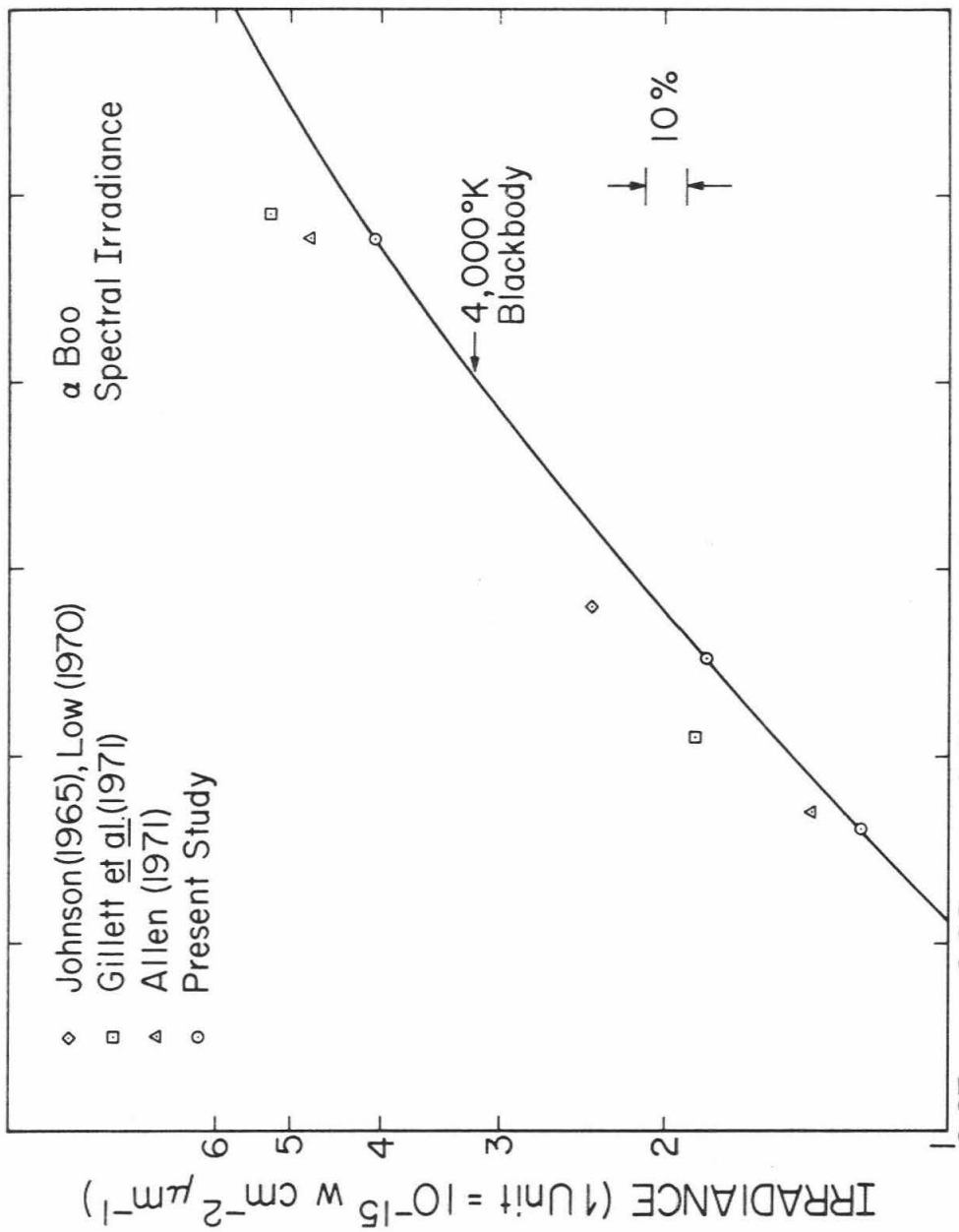
α Boo
Spectral Irradiance
◇ Johnson(1965), Low (1970)
□ Gillett et al.(1971)
△ Allen (1971)
○ Present Study
4,000°K
Blackbody
10%
IRRADIANCE (1 Unit = 10^{-15} w cm^{-2} μm^{-1})
1/λ (μm^{-1})
1
2
3
4
5
6
0.07
0.08
0.09
0.10
0.11
0.12

Table 6 and Fig. 5 show the values that are currently in use. However, the real differences between the infrared calibrations are less than these data suggest. This is because of a ten percent discrepancy in the absolute calibrations for the V filter. For zero V magnitude, Oke and Schild (1970) obtain 3.64×10^{-12} W cm^{-2} μm^{-1} whereas Johnson's (1965) value is 3.92×10^{-12} W cm^{-2} μm^{-1}. So, if all observers use the same V calibration, then the differences in Fig. 5 between the Johnson-dependent calibrations and the present calibration would be reduced to about ten percent or less.

All of the preceding calibrations are monochromatic and a classical problem is to relate these calibrations to the responses of instruments with finite bandpasses. For example, because of the absorption lines and other spectral features of the light that is measured, the absolute calibration of wide-band photometry cannot be expected to yield absolute fluxes that are identical with those obtained from spectrophotometry or even narrow-band photometry for the same objects. Stated another way, one wishes to measure

$$\int_{8}^{14} E(\lambda)\, d\lambda \qquad (12)$$

above the atmosphere but the instrumental deflection, d, is given by

$$d = \int_{8}^{14} E(\lambda)\, Q(\lambda)\, \varphi(\lambda)\, d\lambda \qquad (13)$$

where $Q(\lambda)$ is the atmospheric transmission and $\varphi(\lambda)$ is the instrumental response or the sensitivity. The problem is now demonstrated by letting $E(\lambda)$ be a delta

function with, of course, unit irradiance. The value of (12) is always unity for $8\ \mu m < \lambda < 14\ \mu m$, whereas the instrumental deflection, d, is variable depending upon the wavelength. The advantages of uniform instrument response, $\varphi(\lambda)$ = constant, and clear atmospheric windows, $Q(\lambda) \sim$ constant, are obvious.

It is noted that Eqn. 11 is not the best evaluation of the effective wavelength because it accounts for neither the atmospheric transmission nor the spectrum of the observed radiation above the atmosphere. Hansen (1971, private communication) has taken these factors into account and uses 10.7 μm as the effective wavelength for his bolometric 8-14 μm stellar observations. Fortunately, α Lyr and α Boo do not differ greatly in spectral shape so if Johnson (1965) did use a poor value for effective wavelength it would not invalidate the comparison in Fig. 5. For example, if one takes $\lambda_o = 10.7\ \mu m$, then Johnson would have assigned a corresponding lower value to the irradiance of α Lyr.

The wavelengths used in this work correspond to the center of the bandpass. Effective wavelengths are not employed because the bandpasses are fairly narrow and because the effective wavelengths for the stars and the asteroids observed in Part 2 (effective temperatures of 170 to 250°K) are different.

TABLE 7. CALIBRATION DATA
FOR CONVERSION OF OBSERVED MAGNITUDES INTO IRRADIANCE

λ (μm)	E (λ) for Zero Magnitude (W $cm^{-2} \mu m^{-1}$)
8.5	2.1×10^{-16}
10.5	9.2×10^{-17}
11.6	6.2×10^{-17}

V. PHOTOMETRY OF SOURCES OF UNKNOWN IRRADIANCE

A. Sensitivity

At the telescope the observations of sources with unknown irradiances are alternated with observations of standard stars in such a way that a standard is observed at least once an hour.

The sensitivity of the photometer and telescope is defined by :

$$m_s = -2.5 \log I + m_o \qquad (14)$$

I = observed number of counts

m_o = calibration magnitude

Using the mean data from July 25, 1970, the arbitrary reference levels are set to the values in Table 8.

The sensitivity typically varies by 0.1 mag. on a given night with as much as 0.2 mag. variation likely in the event of marginal or poor nights. Systematic variations between observing runs (i.e. different equipment set-ups) have a peak-to-peak range of several tenths of a magnitude. These systematic variations are presumably instrumental.

B. Data Reduction Method for Unknown Irradiances

All of the observations of sources of unknown irradiance are corrected for nominal extinction. The sensitivity at the time of observation is obtained by

TABLE 8. SENSITIVITY REFERENCE LEVELS

λ (μm)	Counts Corresponding to $m_o = 0.0$ for α Boo
8.5	114,320
10.5	54,948
11.6	45,622

interpolating linearly between the values calculated from standard star observations. The data are reduced to zero magnitude sensitivity and thence to irradiance using the α Boo calibration. That is:

$$\left(\begin{matrix}\text{Unknown}\\ \text{Irradiance}\end{matrix}\right) = \frac{\alpha \text{ Boo Irradiance}}{\alpha \text{ Boo Counts}} \times \left(\begin{matrix}\text{Counts for}\\ \text{Unknown}\end{matrix}\right) \qquad (15)$$

The errors for these measured irradiances are estimated using the formula:

$$\sigma^2 = \sigma^2_{stat} + \sigma^2_{10\%} + \sigma^2_{night} \qquad (16)$$

σ_{stat} is the formal standard deviation carried through the data reduction. $\sigma_{10\%}$ is ten percent of the measured value. This takes into account the errors in the magnitude of the standard stars and in the extinction coefficient. σ_{night} accounts for the quality of the night and is the fractional error of the peak-to-peak variation of the standard star observations, times the measured value of the unknown. To some extent this whole procedure is arbitrary. In Part 2 of this thesis where data for (4) Vesta are examined it is concluded that for 11.6 μm Eqn. (16) gives a reasonable error estimate but that for 8.5 μm and perhaps 10.5 μm the error bars are too large, thus degrading the data.

VI. SUMMARY

Magnitudes quoted for narrow-band photometry at 8.5, 10.5 and 11.6 μm cannot be expected to have an absolute accuracy of better than twenty percent. The agreement of the relative photometry between the different observers for the narrow bandpasses is poor when compared with that already achieved in 8-14 μm (N bandpass) photometry. Presumably closer agreement will result as statistically significant numbers of observations are acquired. In most instances, extinction errors are estimated to introduce less than five percent scatter. The systematic errors in the absolute calibrations are really not known. Nominally the calibration used here differs from that of Johnson (1965) by $\sim$ 16 percent. However, if the different values used for the absolute calibration of the V bandpass are reconciled then this calibration and that of Johnson are found to have a real difference of less than ten percent.

The original contributions of this part of the thesis are: (1) a new calibration which is the first to be totally independent of the work of both Saiedy (1960) and Johnson (1965), (2) a system of standard stars, and (3) a discussion of the errors likely in the relative photometry and absolute calibration.

REFERENCES

Allen, C. W., (1963), Astrophysical Quantities, Second Edition, Athlone Press, London.

Allen, David, A., (1970), Infrared Diameter of Vesta, Nature 227, 158-159.

Allen, David. A., (1971), private communication.

Code, A. D., (1960), Stellar Energy Distribution Chapter 2 in Stellar Atmospheres, Greenstein Editor, University of Chicago Press, 50-87.

Gehrz, R. D., (1971), private communication.

Gehrz, R. D. and N. N. Woolf, (1971), Mass Loss From M Stars, Ap.J. 165, 285-294.

Gillett, F. C., F. J. Low, and W. A. Stein, (1968), Stellar Spectra From 2.8 to 14 Microns, Ap.J. 154, 667-687.

Gillett, F. C., K. M. Merrill, and W. A. Stein, (1971), Observations Of Infrared Radiation From Cool Stars, Ap. J. 164, 83-90.

Hayes, D. S., (1970), An Absolute Spectrophotometric Calibration of the Energy Distribution of Twelve Standard Stars, Ap.J. 159, 165-176.

Hayes, D. S., J. B. Oke, and R. E. Schild, (1970), A Comparison of the Heidelberg and NBS-Palomar Spectrophotometric Calibrations, Ap.J. 162, 361-362.

Johnson, H. L., (1965), The Absolute Calibration of the Arizona Photometry, Communications Lunar and Planetary Laboratory of the University of Arizona, 3, 73-77.

Low, F. J., (1970), Sky Survey, Semi-Annual Technical Report, Air Force Cambridge Research Laboratory, AFCRL-70-0179.

Neugebauer, G., and E. E. Becklin, (1971), private communication.

Oke, J. B., and R. E. Schild, (1970), The Absolute Spectral Energy Distribution of Alpha Lyrae, Ap.J. 161.

REFERENCES
cont.

Plass, G. N., and H. Yates, Atmospheric Phenomena, Handbook of Military Infrared Technology, Chapter 6, William L. Wolfe, Ed., Office of Naval Research, Department of the Navy (1965).

Saiedy, F., (1960), Solar Intensity and Limb Darkening Between 8.6 and 13 μ, M. N. R. A. S., 121, 483-495.

Schild, R., D. M. Peterson, and J. B. Oke, (1971), Effective Temperatures of B- and A-Type Stars, Ap.J. 166, 95-108.

Stebbins, J., and G. E. Kron, (1964), Six-Color Photometry of Stars, XI, Black-Body Color Temperatures of 25 Stars, Ap.J. 139, 424-434.

Willstrop, R. V., (1960), Absolute Measures of Stellar Radiation, M. N. R. A. S. 121, 17-40.

PART 2. INFRARED OBSERVATIONS OF ASTEROIDS AT WAVELENGTHS OF 8.5, 10.5 and 11.6 μm

PART 2. INFRARED OBSERVATIONS OF ASTEROIDS AT WAVELENGTHS OF 8.5, 10.5 and 11.6 μm

I. INTRODUCTION

The purpose of Part 2 of this thesis is to report new observations of the thermal radiation emitted from asteroids. The reason for doing infrared photometry is that these observations and their subsequent interpretation provide new and unique information. The combination of the new infrared data and the previously existing visible-wavelength photometry places important constraints upon models that are used to represent asteroidal surfaces. Thus, the sizes, the albedos and, in some cases, the emissivities can be estimated for real asteroids. The key to obtaining this information is conservation of energy; the requirement to balance the reradiation of absorbed (visible) energy and the reflected visible light against the total solar insolation. The infrared photometry provides a way of estimating the amount of energy re-emitted by an asteroid.

The important result of this effort is to find that by and large the asteroids observed in this thesis have lower (visible) albedos than previously believed and to "measure" albedos that span a range of an order of magnitude.

Optical disk measurements have been published for Ceres, Pallas, Juno and Vesta. These measurements are very difficult to perform because of the small angles subtended by the asteroidal disks and because of the turbulence ("seeing")

of the Earth's atmosphere. The diameters so determined have been criticized extensively in the literature. Now, the infrared photometry gives new ground upon which to question the accuracy of these disk measurements.

Low (1965) was the first author to publish an infrared measurement of an asteroid. He reported 233 ± 10°K as the 8-14 μm brightness temperature of (1) Ceres. Later he observed (4) Vesta and found its N-magnitude (8-14 μm) to be -2 (Low 1970). D. A. Allen (1970, 1971) was the first author to discuss the significance of the infrared data and he proceeded to solve for the "infrared diameters" of several objects. Finally, Veverka (1970a, b, 1971) attacked the problem of size and albedo through use of visible-wavelength polarimetry. He estimated sizes and albedos for (4) Vesta and (8) Flora.

Allen's (4) Vesta data are particularly important because they were obtained during the same opposition as the observations that are presented here and through roughly similar bandpasses.

The next section of this paper presents observations of twenty-six asteroids. Some asteroids have been observed only once while others have been observed extensively in order to collect phase and lightcurve data. By use of color plots for direct comparison of the visible and infrared wavelength observations, differences between individual asteroids can be identified. These differences are not dependent upon the assumptions of any model.

The third section introduces the thermal model which is used for the detailed analysis of the (4) Vesta, (7) Iris and (324) Bamberga observations.

Modelling of the observable parameters is discussed. In section four it is found that the model gives about the expected answers for (J3) Ganymede but does not explain the observations for (J4) Callisto. The (4) Vesta data are found to be satisfied if the bolometric Bond albedo for that body is about ten percent. When the data for the other asteroids are examined it is found that (324) Bamberga is extremely dark.

The problems raised by these observations are discussed in section 5.

The need for, and specific nature of, future work comprises the sixth section. An important long range goal is to determine the distribution of asteroidal properties. Such information would then enable comparative studies of asteroids, meteorites, comets and the crater populations on planetary surfaces.

II OBSERVATIONS

The infrared observations are presented in this section. Wherever possible the observations are compared with analogous visible-wavelength photometry. This comparison allows some conclusions to be drawn immediately. The discussion of the observational technique for asteroids is followed by the infrared lightcurve and phase effect data. Next, special diagrams plot the infrared versus the visible-wavelength photometry. The color diagrams are the important part of this section because these diagrams show clearly that there are differences between the surfaces of some of the asteroids. Finally the data for (J3) Ganymede and (J4) Callisto are presented and compared with existing infrared photometry by other observers.

Method and Coverage

All of the observations havebeen made through the bandpasses centered at wavelengths of 8.5, 10.5 and 11.6 μm. The photometry is described in Part I of this thesis and the photometer in Appendix II. The data are from August 1969 through July 1970. All have been collected using the Mt. Wilson 60-inch telescope of the Hale Observatories.

The irradiance above the Earth's atmosphere is obtained from each observation. Here the units used for irradiance are W $cm^{-2} \mu m^{-1}$ with the symbol "E" as recommended by Nicodemus (1970). The symbol "E" will be used exclusively to refer to the irradiance above the Earth's atmosphere. The

irradiance data for asteroids and satellites are reduced to a standard reference distance of 1 AU from the object by forming the product $E \cdot \Delta^2$. Δ and other symbols that are traditionally used in the asteroid literature are explained in Figs 1 and 2. By comparison, visible-wavelength photometry is usually reduced to unit distances from both the Sun and the Earth ($r=1$, $\Delta=1$). Unfortunately there is no simple way to do this for photometry of thermal emission.

Fig. 1. Nomenclature used in the asteroid literature. r is the distance between the sun and the asteroid. R and Δ are the sun-earth and earth-asteroid distances respectively. Φ is the phase angle as measured in the plane defined by the sun, earth and asteroid. All distances are given in astronomical units (AU).

Fig. 1.

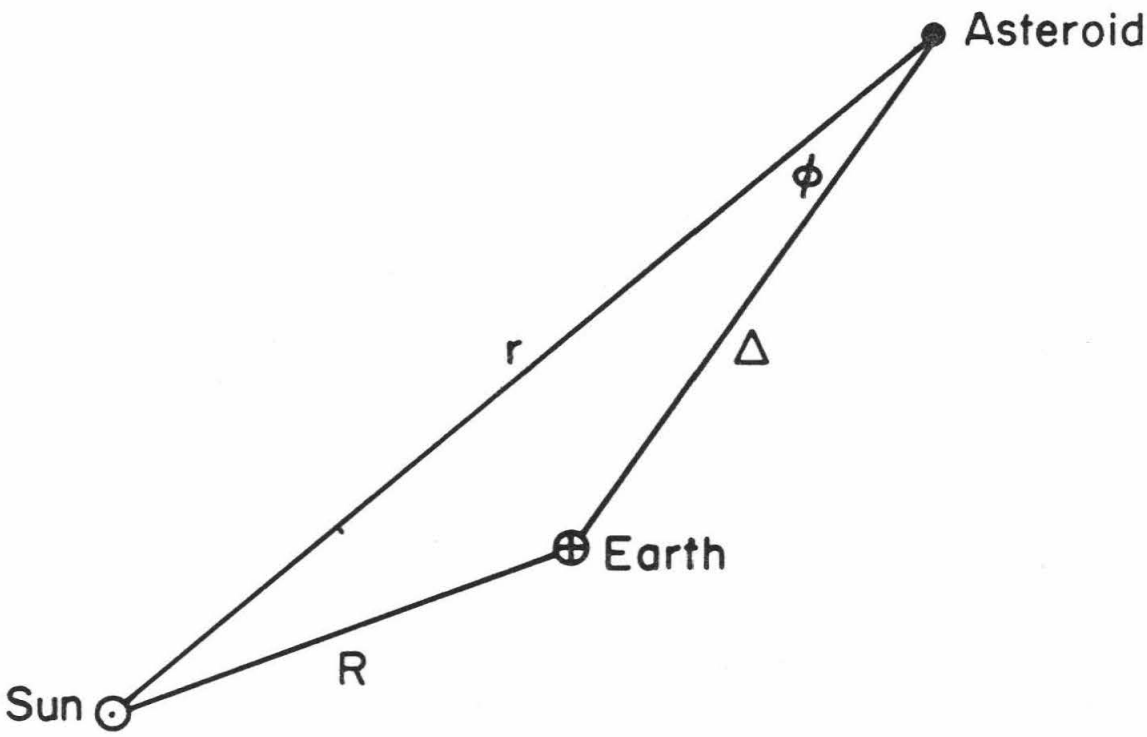

Fig. 2. Reference angles for an asteroid. φ is the phase angle and ψ is the aspect.

Fig. 2.

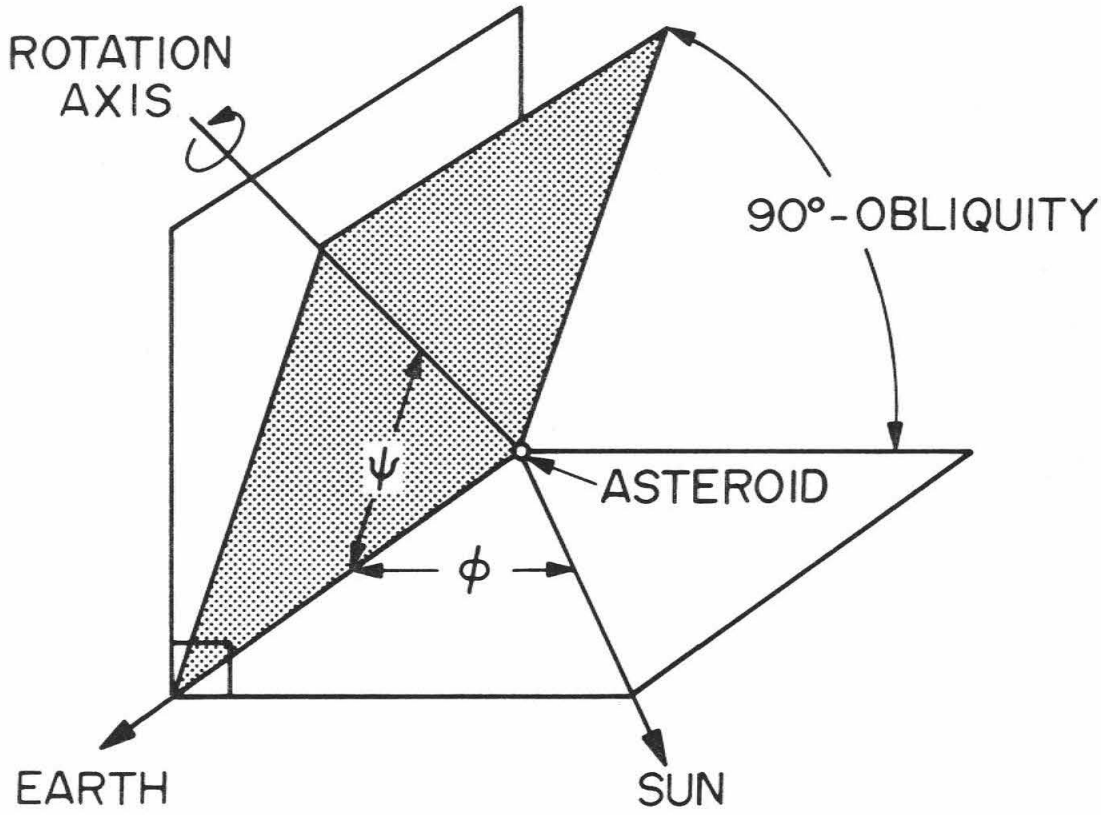

The accuracy of the observations has been discussed in Part 1. In addition to the procedures described there, each asteroid observation is tested here for the presence of a limiting mean. This is done by plotting the cumulative mean versus the number of deflections. Observations that show poorly on this plot are assigned half weight. The best criterion for reliability is, of course, to repeat the observations on several different nights. For objects yielding poor instrumental signal-to-noise ratios there is always the possibility that part of the signal could be from uncompensated background radiation. Great care must be exercised in interpreting such data.

Most of the asteroids were acquired by setting the telescopes at the appropriate ephemerides coordinates. The positions for every tenth day came from the Institute for Theoretical Astronomy in Leningrad (U.S.S.R. 1969, 1970; Herget 1970, private communication) and from the Cincinnati Observatory (Herget 1970, private communication). The hourly positions for each object were obtained using Bessel's second order interpolation formula and the telescope was set to the nearest hourly position. In practice this was accomplished using the setting circles to make precise differential offsets from bright finding stars. Usually the asteroid was required to be no farther than a minute of arc from the nominal position. The exact tolerance allowed, of course, depended upon the magnitude of the asteroid with respect to the magnitudes of the field stars. For each object the visual magnitudes were estimated both through the main 60-inch telescope and through a 4-inch finder. These estimates were compared with expected values computed in advance. The color had to be similar to solar-type stars and

the position of the object was checked against the field stars. Prints from the National Geographic Society-Palomar Observatory Sky Survey were used to verify that there were no bright stars at the object's observed position. Differential motion with respect to field stars is a sufficient condition for identification but only if there is no other asteroid close about. A strong infrared signal is also diagnostic. For example, some 9th magnitude asteroids give substantial infrared signals, whereas a G2 star of that magnitude could not be detected.

Many asteroids were not found because they were not close enough to their nominal positions to be acquired quickly. (16) Psyche, (192) Nausikaa and (324) Bamberga, were some of the more difficult asteroids which were eventually acquired. Brian Marsden (1971, private communication) notes that for these objects the Crimean Astrophysical Observatory has found the right ascension residuals for the 1968-69 ephemerides to be $0^{m}.3$, $0^{m}.4$, and $0^{m}.8$ respectively.

The emphasis of this thesis was placed on studying a variety of objects and effects. This type of reconnaissance approach was chosen so that the success of the investigation would not depend entirely upon the fruitfulness of any single activity. On the other hand, this approach did not permit a complete and in depth study of any of the topics.

There were three chief priorities for the asteroid observations. The first was to search for differences between asteroids; the second was to look for any infrared lightcurve variation; the third was to measure the infrared phase effect. Other priorities which shared the telescope time were standard star

photometry, and observations of (J3) Ganymede and (J4) Callisto. The first goal required sampling a large number of objects and the second and third goals were met by repeated observations of four asteroids. J3 and J4 were included for use as test cases for the data analysis because their diameters are fairly well known.

The 11.6 μm bandpass was used most frequently because it was expected to be closest to the peak of the thermal emission spectrum for most of the asteroids. Minor planets that proved to be bright at 11.6 μm were also measured at 8.5 and 10.5 μm.

The observational coverage of asteroids is summarized in Table 1. The last two columns of this table show where limited phase and lightcurve data were acquired. Here the lightcurves are really "composite lightcurves", and they are formed by combining data gathered on different nights. Some of the asteroids observed at 11.6 μm were not reobserved because they did not initially yield a good instrumental signal to noise ratio.

There are several important types of bias in the data and the properties of all asteroids cannot be extrapolated from these observations. First, only bright and easy-to-find objects were selected. In a second step, these asteroids were further screened by picking only those likely to have measurable infrared signals. The net effect of this selection is to discriminate against the small dark objects, and objects beyond 2.5 or 3.0 AU and to favor large asteroids with high albedo.

TABLE 1. SUMMARY OF ASTEROIDS OBSERVED

		Bandpasses			Phase	Composite
		8.5μm	10.5μm	11.6μm	Coverage	Lightcurve
1	CERES	1	-	2		
2	PALLAS	2	4	7		
3	JUNO	-	-	5		
4	VESTA	12	8	20	8.5, 10.5, 11.6	8.5, 10.5, 11.6
5	ASTRAEA	-	-	1		
6	HEBE	4	-	11		11.6 (fractional)
7	IRIS	4	10	16	8.5, 10.5, 11.6	8.5, 11.5, 11.6
8	FLORA	-	-	1		
9	METIS	-	1	-		
15	EUNOMIA	-	-	1		
16	PSYCHE	-	-	1		
18	MELPOMENE	-	-	1		
19	FORTUNA	1	-	1		
20	MASSALIA	-	-	1		
25	PHOCAEA	-	-	1		
27	EUTERPE	-	-	1		

(continued on next page)

- continued -

TABLE 1. SUMMARY OF ASTEROIDS OBSERVED

		Bandpasses			Phase	Composite
		8.5μm	10.5μm	11.6μm	Coverage	Lightcurve
39	LAETITIA	6	3	3		
44	NYSA	-	-	1		
68	LETO	-	-	1		
80	SAPPHO	-	2	2		
145	ADEONA	1	-	4		
163	ERIGONE	1	-	-		
192	NAUSIKAA	-	-	3		
313	CHALDAEA	-	-	3		
324	BAMBERGA	3	5	7	10.5, 11.6	
674	RACHELE	-	-	1		
TOTALS	26	35	33	95	8	7

Infrared Lightcurves

The visible light received from an asteroid usually shows a periodic variation on a time scale of a few hours. Undoubtedly this variation is caused by the axial rotation of the asteroid, but the exact details of how the fluctuations are produced are not known. There are several possibilities. Lightcurves may be due to differences in the projected area, to patches of different albedo, to variations of the local photometric phase function, or to combinations of all three. Asteroids are expected to exhibit lightcurve variations in the infrared and there should be definite relationships between the visible and infrared lightcurves. For example, if the albedo varies over the surface, then when a darker region comes into view, the infrared signal would increase as the signal in the visible diminishes.

Enough observations were obtained for (4) Vesta, (6) Hebe, and (7) Iris that their lightcurve variations can be studied. Unfortunately these observations did not yield any major new conclusions in that the effects appear to be less than the scatter of the data. However, this is the first time that this effect has been studied and the lightcurves serve the important purpose of showing that this variable has been properly sampled. Later, in the case of (4) Vesta, this coverage allows the standard deviation of the mean to be used to estimate the error of the observations.

A composite lightcurve is formed by bringing together the available data for an asteroid and plotting the irradiance versus the rotational phase angle.

If the period of rotation is known, each observation can be registered to the correct rotational phase angle. However, the precise functional relationship between the lightcurve amplitude and the coordinate frame fixed in the asteroid is not known. This problem leads to a smearing of the features of the lightcurve when the data to be combined are obtained at different solar phase angles, φ. The limits for this smearing can be computed by considering the extreme cases. The maximum possible range of variation is given by the angle in planetocentric equatorial right ascension that is subtended by the Earth (as seen from the asteroid), between the epochs of the first and the last observation. If the position of the rotation pole is not known, then the entire angle is assumed to lie in planetocentric right ascension. These limits for smearing are plotted with each lightcurve. The irradiance values in the composite lightcurve also include the solar phase angle variation. In a later section, when a model is derived, this effect will be removed from the (4) Vesta lightcurve.

The data for (4) Vesta are tabulated in Tables 1 and 5 in Appendix I, and Fig. 3 shows the composite lightcurve. The data for each bandpass are compatible with the dashed curve, but upon considering the error bars, perhaps a constant value (horizontal line) would be as satisfactory. The dashed line in Fig. 3 is actually the visible-wavelength (V filter) lightcurve from Gehrels (1967a). The visible curve has been advanced to the epoch of the infrared observations by using the period for (4) Vesta of $5^{h}.342\ 129$ (Gehrels 1970). The vertical (irradiance) level has been adjusted to match the curve to the infrared data for

Fig. 3. Thermal Emission lightcurve for (4) Vesta. The dashed line is the visible lightcurve and it has been fit to the data by translation in the vertical direction only. The maximum phase distortion shows the limits for horizontal scrambling of the lightcurve by the compositing process.

Fig. 3.

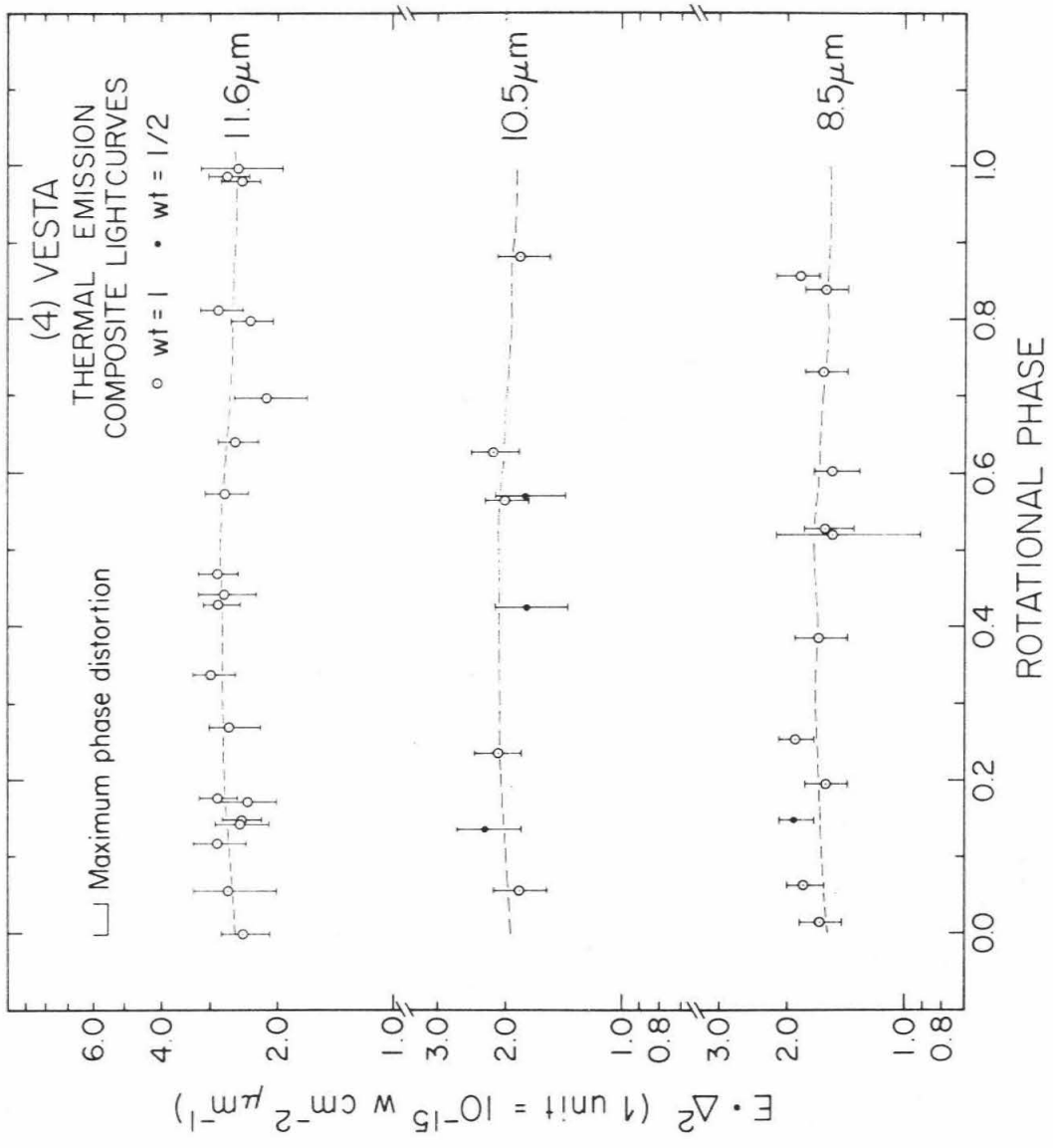
(4) VESTA
THERMAL EMISSION
COMPOSITE LIGHTCURVES
○ wt = 1 • wt = 1/2
Maximum phase distortion
11.6μm
10.5μm
8.5μm
E • Δ² (1 unit = 10⁻¹⁵ w cm⁻² μm⁻¹)
ROTATIONAL PHASE
0.0
0.2
0.4
0.6
0.8
1.0
6.0
4.0
3.0
2.0
1.0
0.8

each bandpass. The comparison here is valid because the difference in ecliptic longitude between the infrared and visible data is not too large. The visible data were obtained when (4) Vesta was near 125° ecliptic longitude and 4° latitude. For the most part the infrared data are near one hundred thirty degrees longitude and north twenty-four degrees latitude.

Though (4) Vesta's infrared lightcurve is fairly flat and apparently devoid of any grossly complicated structure, it does clear up a minor detail. From the small maximum 0.13 magnitude amplitude of the visible lightcurve, (4) Vesta has been thought to be nearly of spherical shape with a surface of fairly uniform albedo. The infrared lightcurve finally rules out the possibility that the shape of (4) Vesta is grossly elongated with the ends of small geometric cross-section suitably lightened in albedo so as to keep the reflected light nearly constant. In a situation where the contrast of the visible lightcurve is suppressed, the infrared lightcurve will actually be amplified and vice versa.

The observations of (6) Hebe show a large variation. The data are tabulated in Appendix I and plotted in Fig. 4; at 11.6 μm the value of $E \cdot \Delta^2$ varies from 2.9 to 8.8 x 10^{-16} W cm^{-2} μm^{-1}, a factor of three. This type of variation is considerably larger than the variation of 0.16 magnitude which is the largest amplitude so far observed for (6) Hebe in the visible.

Fig. 4 Infrared lightcurve for (6) Hebe. The dashed line is the closest available visible lightcurve. Its vertical exaggeration is about a factor of 22 and it has been translated both vertically and horizontally to fit the infrared data. The translation along the abscissa is necessary because the rotational phase angle for the visible data at the epoch of the infrared observations is unknown.

Fig. 4.

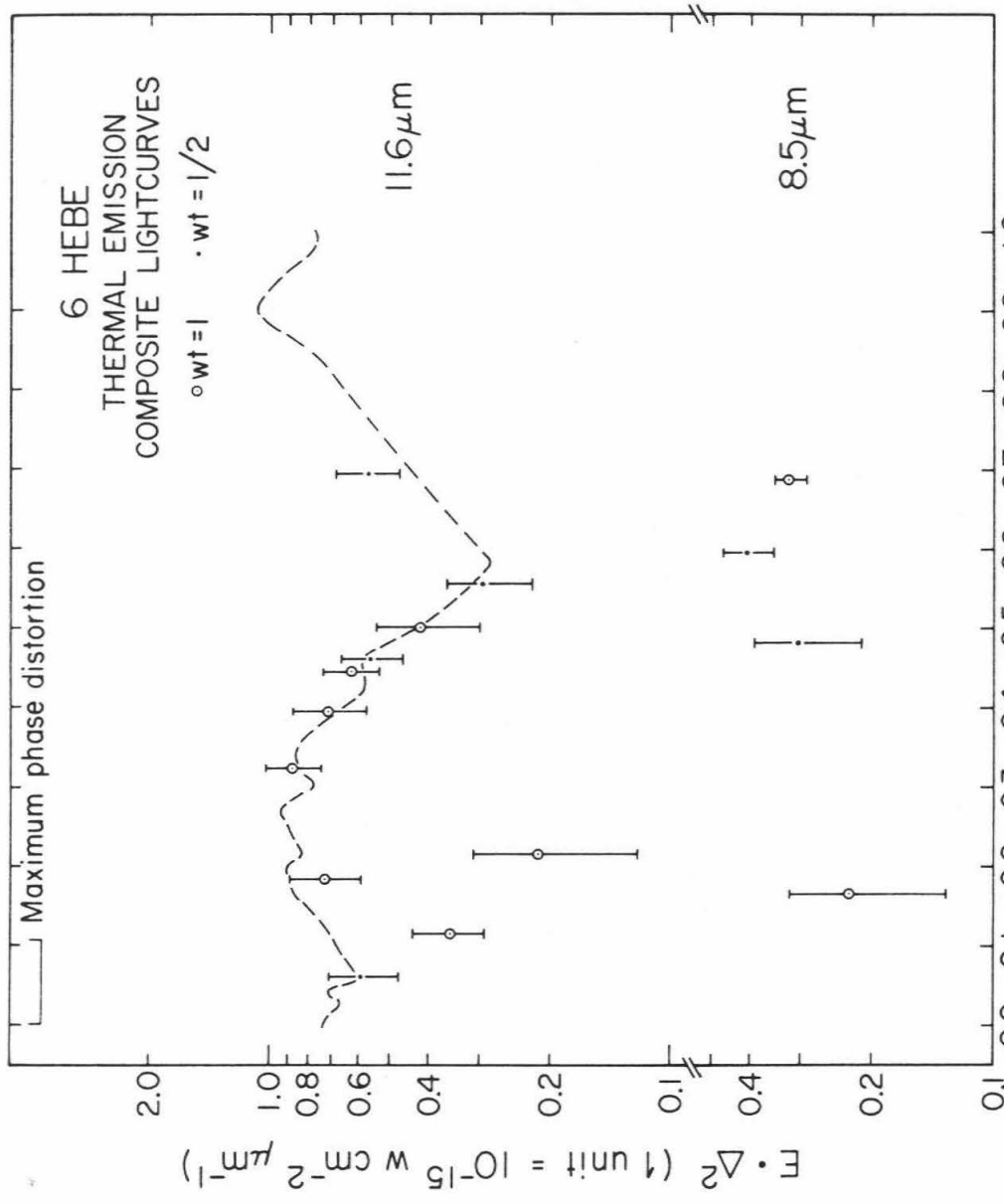
6 HEBE
THERMAL EMISSION
COMPOSITE LIGHTCURVES
○ wt = 1 · wt = 1/2
Maximum phase distortion
11.6μm
8.5μm
FΔ² (1 unit = 10⁻¹⁵ w cm⁻² μm⁻¹)
ROTATIONAL PHASE
2.0
1.0
0.8
0.6
0.4
0.2
0.1
0.0
0.1
0.2
0.3
0.4
0.5
0.6
0.7
0.8
0.9
1.0

However, near 0.2 in rotational phase the 11.6 μm data show a large amount of scatter because other points for the same nights as the two low values follow the trend of the rest of the data. The apparent peak in the 8.5 μm data is attributed to random scatter.

The low instrumental signal-to-noise ratio for this object argues that the two discordant 11.6 μm points should be taken as a conservative measure of the true scatter in the data. However, the nine other 11.6 μm data which were obtained on four different nights seem to follow a trend that bears discussing.

Comparison with visible data for Hebe cannot be done exactly, because the cumulative error in the rotation period has already exceeded half a revolution. The visible lightcurve for (6) Hebe is from Ahmad (1954), for which the ecliptic longitude is about 353° while the longitude for the infrared data is in the vicinity of one hundred and fourteen degrees. When the longitude difference is this large, comparison of the visible and infrared curves can not be regarded as a completely legitimate procedure, but no alternative exists. In the illustration, Ahmad's lightcurve is vertically exaggerated by a factor of 21.7 and is fit to the 11.6 μm data by translation both vertically and horizontally. This modification of his curve is the dashed line in Fig. 4. The position of (6) Hebe's pole has yet to be properly determined (Vesely 1971) and this is one of the reasons for the larger limit set for horizontal scrambling.

If the difference between the amplitudes of the visible and the infrared lightcurves is real, then either (6) Hebe has patches of different albedo on its

surface or 1970 was an extremely favorable opposition. If the correct registration between the infrared and visible lightcurves is as drawn in Fig. 4, and if the amplitudes are really in the ratio 20:1, then the data would suggest a variation of albedo across Hebe's surface. This is because a change in the projected cross-section would give lightcurves of equal amplitude in both spectral regions. However, in the event of an extremely favorable opposition, at the epoch of the infrared observations the visible lightcurve would have had an amplitude equal to that suspected in the infrared and both would simply be due to a changing cross-sectional area. If this were true, then (6) Hebe would be elongated by about $\sqrt{3}$:1. By way of comparison, (624) Hector is elongated in the ratio of about 5.3 : 1 (Dunlap and Gehrels 1969).

In order to check on possible albedo variations, Ahmad's curve was inverted, but this way a good fit to the infrared data could not be found for any translation or vertical exaggeration factor.

The author is unaware of any visible photometry coincident with his infrared observations. Some recent visible photometry (Gehrels 1971, private communication) and colorimetry (Chapman 1971, private communication) have been obtained for (6) Hebe and the data are currently in the process of being reduced. Because of the uncertainty in the pole position, it is not obvious that these new observations will help to resolve the present dilemma. The diagnostic information will be simultaneous visible and infrared lightcurves of Hebe.

The composite lightcurves for (7) Iris are in Fig. 5 and the data are

Fig. 5.

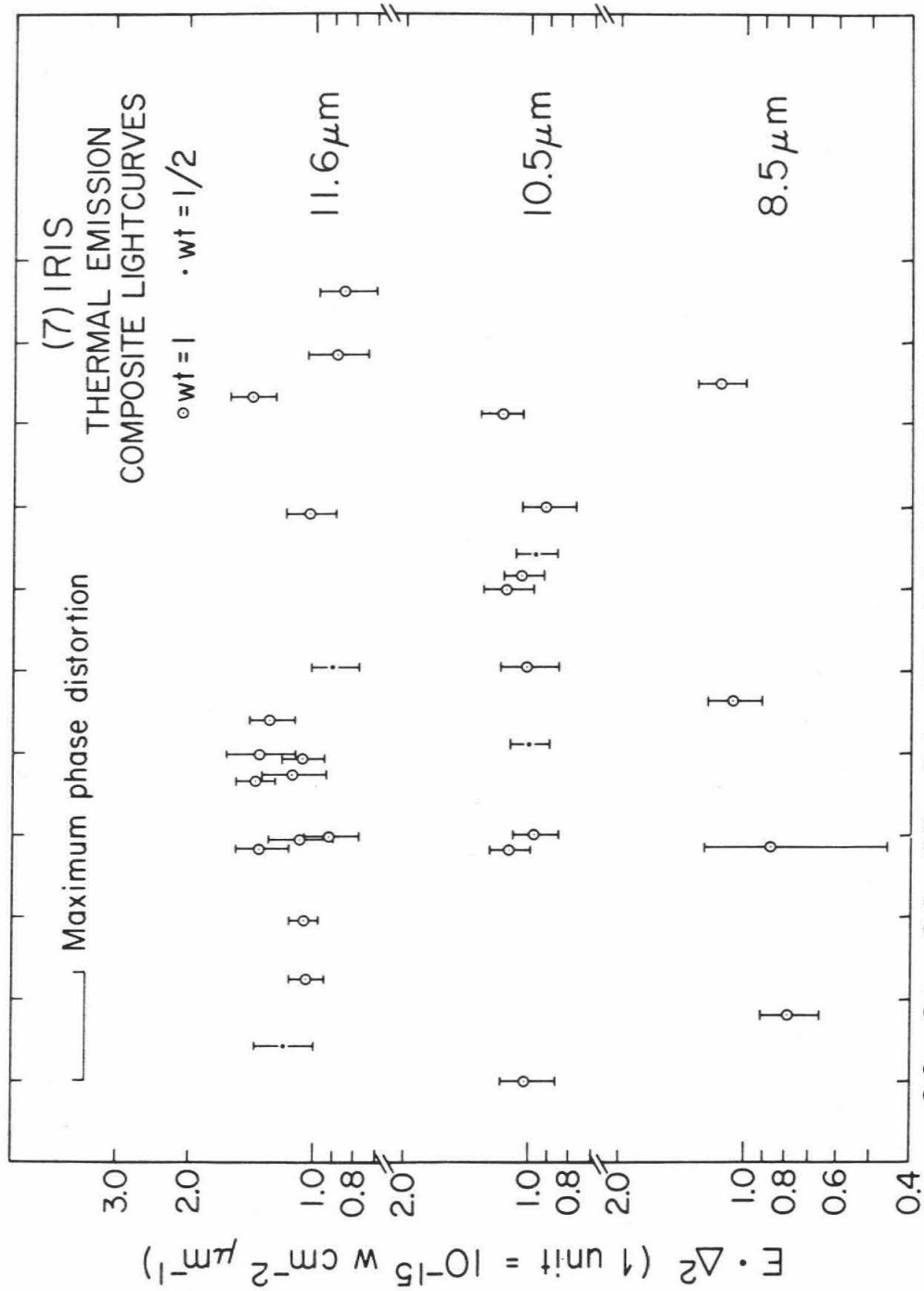

Fig. 5. Infrared lightcurve data for (7) Iris

tabulated in Appendix 1. The data 11.6 μm appear to have an excessive amount of scatter when compared to those obtained at 10.5 μm. The rotational phase angle for the visible photometry of Iris is currently lost due to the cumulative error in the rotation period. The author knows of no visible lightcurves that correspond either to the epoch or the ecliptic longitude of these infrared data. The existing visible lightcurves for Iris show a maximum amplitude of 0.29 magnitude. This amplitude is about that exhibited by the 10.5 μm lightcurve data. Thus the available infrared data are consistent with the hypothesis of a slightly irregular shape.

Infrared Phase Effect

Measurement of the angular distribution of the light from asteroids is an important way to test theoretical models. The best technique for phase effect work is to take complete lightcurves throughout an entire opposition and to plot the phase effect for either the maximum or the minimum or for some other distinctive feature on the observed lightcurves. This procedure would largely remove the lightcurve variation but it would require a tremendous amount of telescope time.

However, it is possible to have a first look at the infrared phase effect with the available data. The observations on each night are averaged and plotted as a function of solar phase angle. On the plots for (4) Vesta and (7) Iris that follow, the numbers beside each point show how many observations were averaged.

Data for (4) Vesta are plotted in Fig. 6. The observations obtained by D. A. Allen (1970), for this same opposition are also plotted but with a different set of symbols. Allen's 11.8μm data are roughly comparable with the 11.6 μm observations of this work and thus they are all plotted together. The $E \cdot \Delta^2$ has been computed for his data and it has then been increased by 17.5% to remove the systematic difference in absolute calibration discussed in Part 1 of this thesis. On the other hand, the 8.5 μm data have not been adjusted and there may be both real and systematic differences between observers. There also seems to be a difference in the slope of the data between the two observers, but it must be remembered that the effect of the lightcurve has not been removed.

From Allen's 11.8 μm and the present 11.6 and 8.5 μm data a reasonable lower bound can be set for the infrared phase effect. This empirical boundary is compared in Fig. 7 with the visible phase effect. Both are normalized to unity at $\varphi = 0°$. The infrared phase variation is much less pronounced than the effect at visible wavelengths.

The (7) Iris phase data are plotted in Fig. 8. The scatter is rather large but the effect appears to resemble that for (4) Vesta.

Color Diagrams

Color diagrams are used to compare the thermal emission data with previsously existing visible photometry. These plots are important because they display the observational data before model-dependent corrections are introduced.

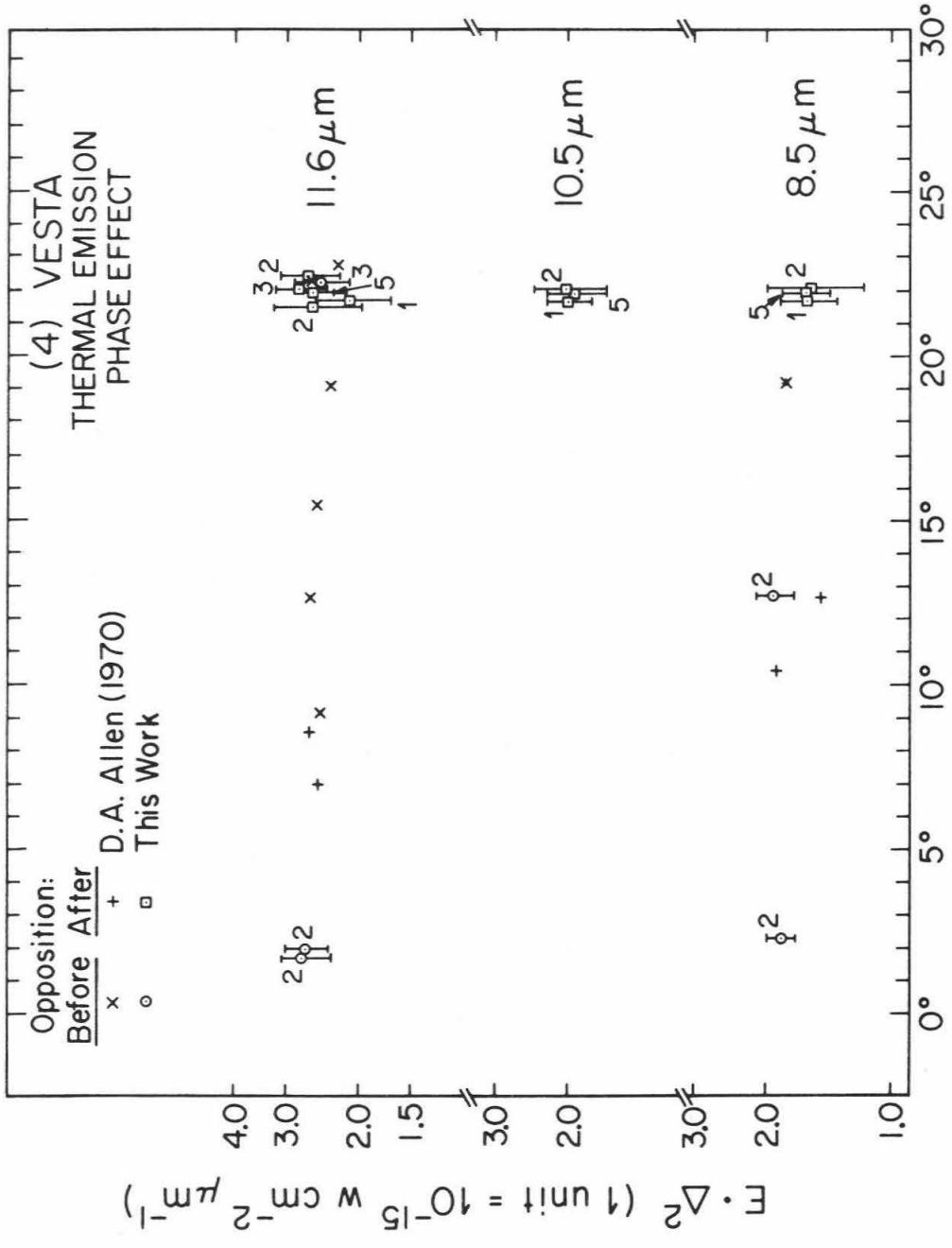

Fig. 6. Thermal emission phase effect for (4) Vesta.

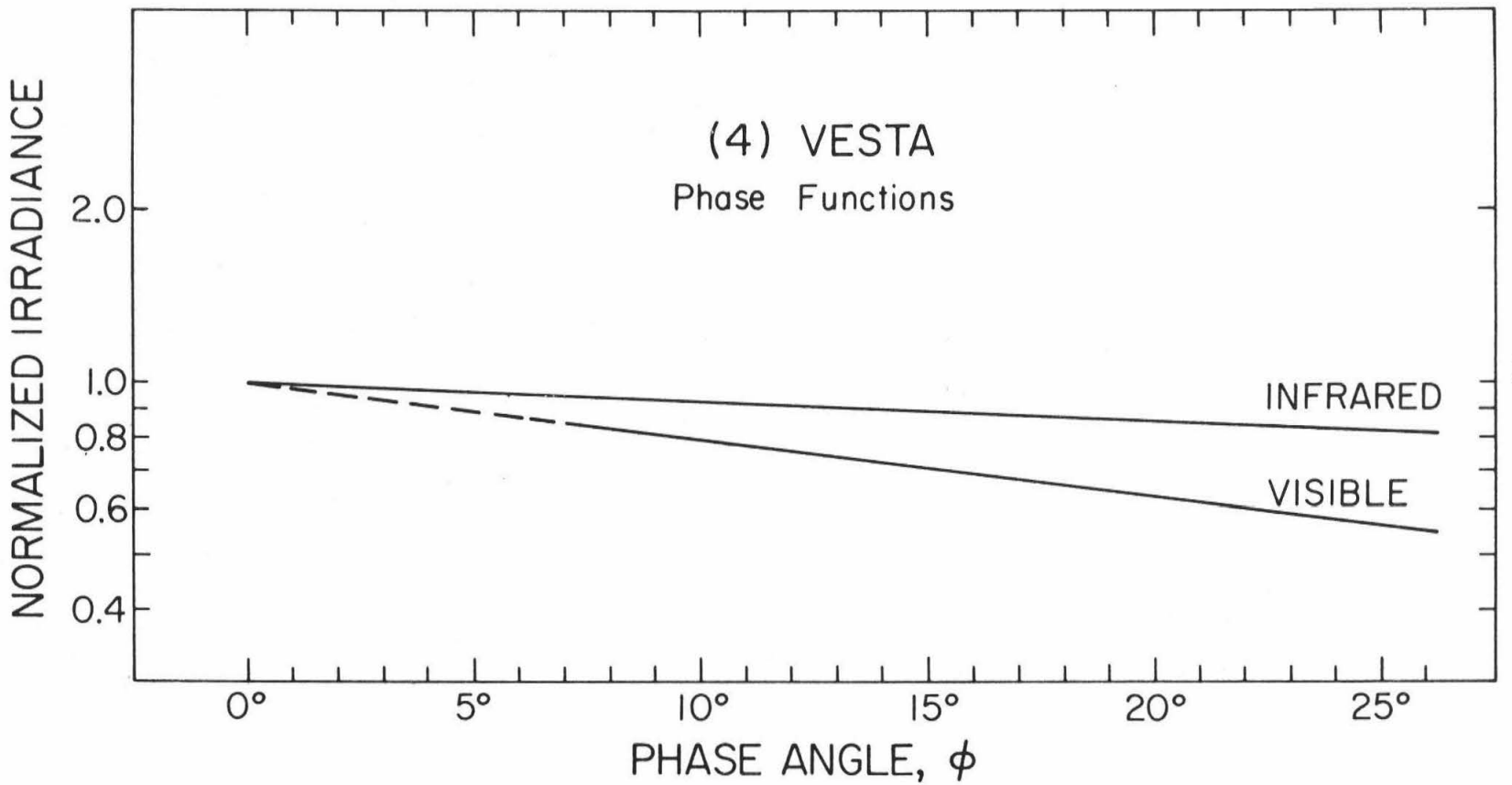

Fig. 7. Comparison of observed phase effects.

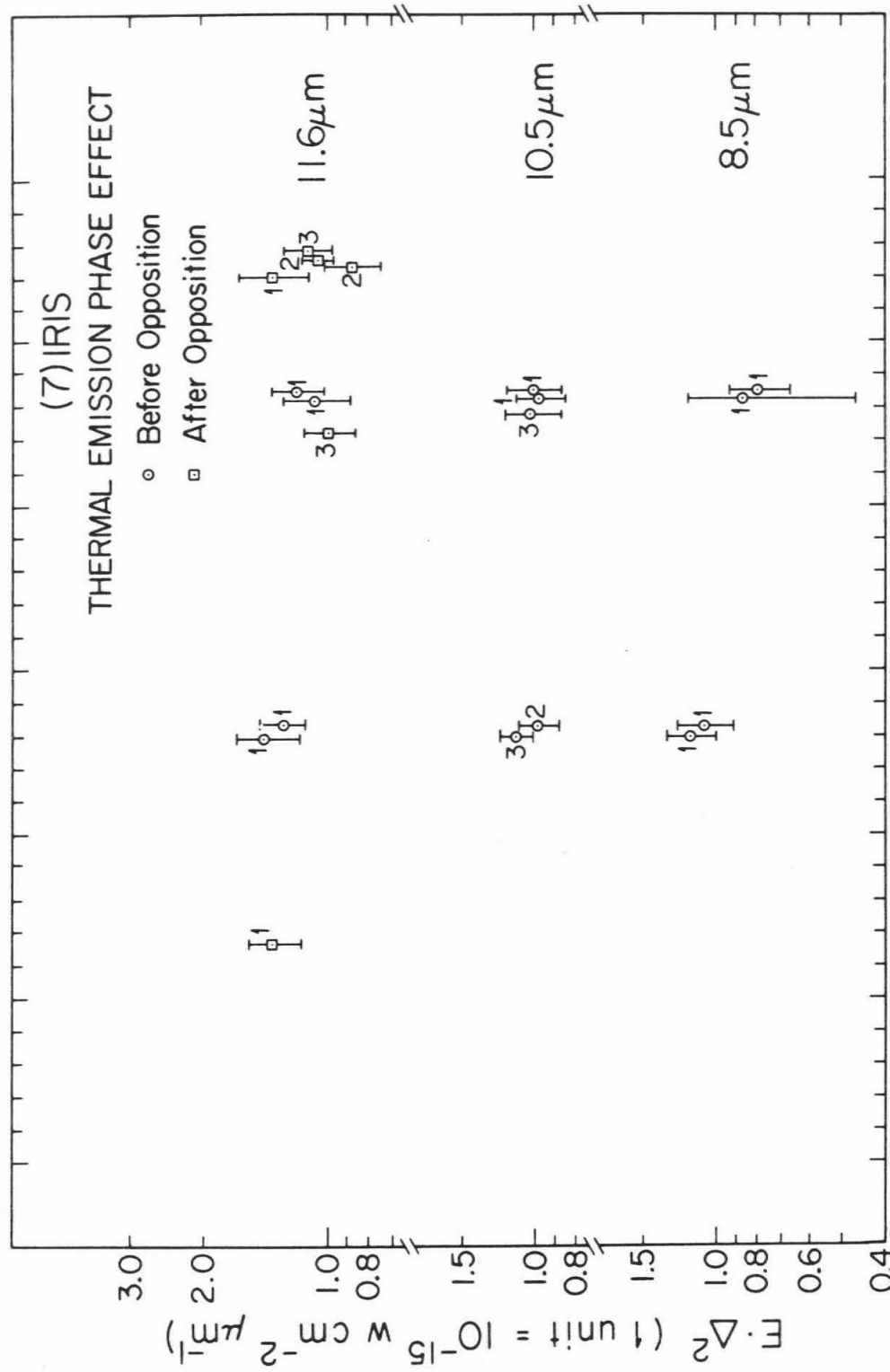

Fig. 8. (7) Iris. Phase effect data.

There are three plots, one for each bandpass. The ordinates are $E \cdot \Delta^2$ and the error bars are for the infrared photometry only. Because $E \cdot \Delta^2$ is a function of the distance from the sun, different symbols are used to show the distance intervals. The symbols and the distribution of the asteroids with radius vector, r, at the time of observation are shown in Fig. 9. The numerical data are tabulated in Appendix 1.

The abscissa are the absolute B magnitudes of the asteroids, B(1,0). The quantity B(1,0) is defined and illustrated in Fig. 10. Recent values have been tabulated by Gehrels (1970). Though B(1,0) is strictly an operationally defined parameter, its definition is so direct that it is useful to think of B(1,0) as a property of the asteroid.

To obtain error bars for the B(1,0) data one must consider both the error in the tabulated B(1,0) magnitudes and the possible error due to the lightcurve at the time of the infrared observation. The errors in average magnitude are due chiefly to phase, rotation and aspect variations. The weights assigned by Gehrels (1970) to the value of B(1,0) for each asteroid are used to estimate the standard deviation by the formula:

$$\text{s.d.} = \frac{0.194 \text{ magnitude}}{(0.67) \times (\text{weight})} \qquad (1)$$

The probable error of 0.194 magnitude corresponds to unit weight. The light-curve error is taken as one-half of the range of the maximum variation tabulated by Gehrels (1970). These variations are reasonably well known for only those

Fig. 9. The distribution of the distances from the sun to the asteroid at the time of observation.

Fig. 9.

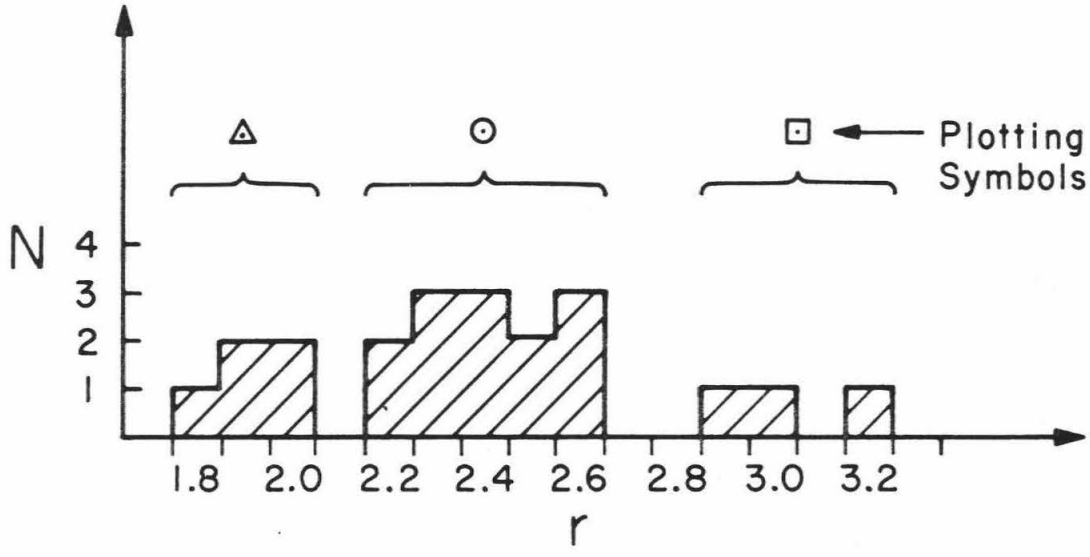

Fig. 10. Idealized B magnitude versus phase plot showing how the opposition magnitude is obtained by extrapolation. The absolute magnitude, B(1,0), is obtained when the opposition magnitude is corrected to unit distances ($r = 1$, $\Delta = 1$). The "0" in B(1,0) refers to zero degrees phase angle, $\varphi = 0°$. The opposition effect is the brightening which occurs at small phase angle (see Gehrels 1956, 1970 p. 363 and Gehrels et al 1964. See Oetking 1966 for laboratory data.).

Fig. 10.

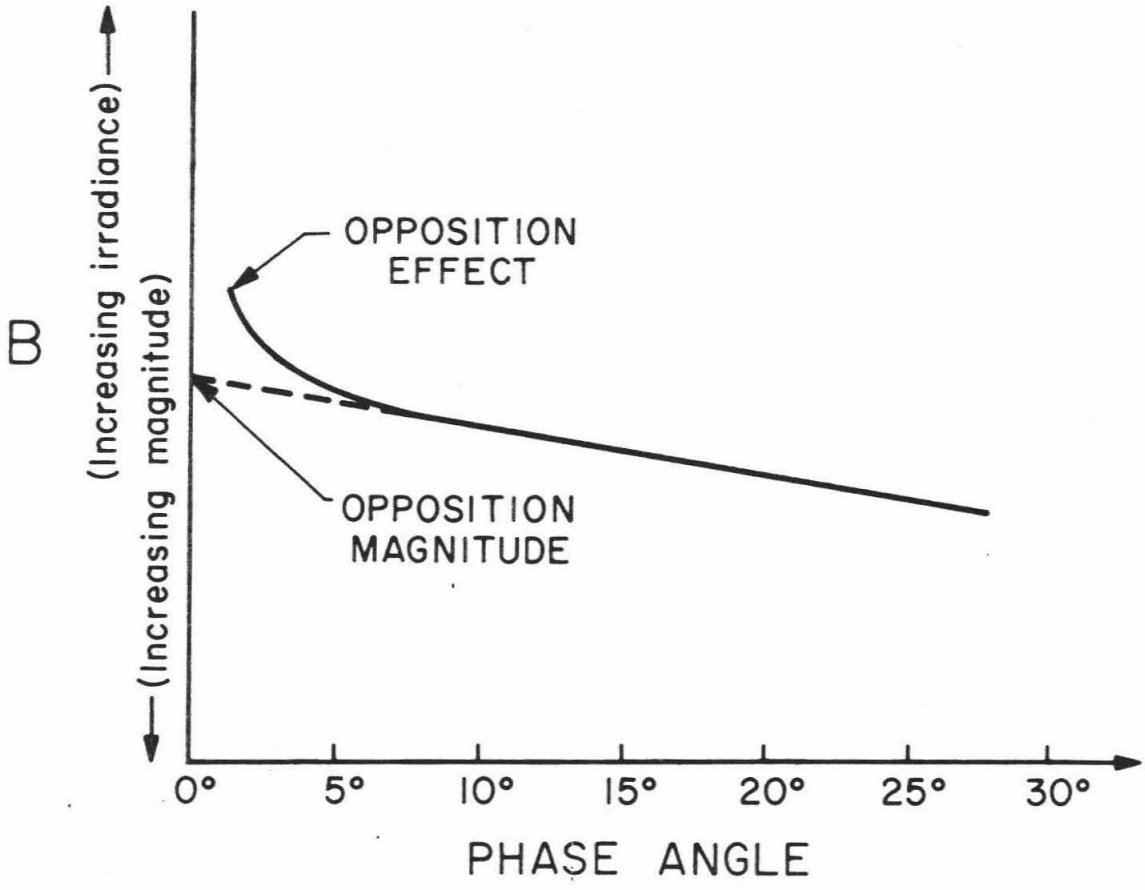
B
(Increasing irradiance)
(Increasing magnitude)
OPPOSITION
EFFECT
OPPOSITION
MAGNITUDE
0°
5°
10°
15°
20°
25°
30°
PHASE ANGLE

few asteroids which have had their lightcurves measured at several different ecliptic longitudes. With the general paucity of lightcurve data currently available, meaningful error bars cannot even be assigned for most of the large asteroids of radius greater than 50 km. Whenever lightcurve data are not available, an error of ± 0.15 magnitude is arbitrarily assumed. For the observed asteroids with error bars assigned by the above procedure, the lightcurve errors dominate except for asteroids 1, 6, 20, 192 and 674, where the errors in the mean absolute magnitudes are larger.

Now consider the point plotted on one of the $E \cdot \Delta^2$ versus B(1,0) graphs for the hypothetical asteroid (0) Asterid*. Figure 11 shows how the point moves on the diagram when the various properties of the asteroid are changed. The scales are chosen in such a way that changes in the size of the minor planet move the point along a line of unit slope. If Asterid becomes darker or lighter in albedo then the change is indicated. The result of a variation in effective emissivity depends upon the specific situation. Figure 11 illustrates one of two cases where the $E \cdot \Delta^2$ bandpass is on the blue slope of the thermal radiation spectrum. With the visible-wavelength albedo fixed the absorbed solar energy is constant. If the emissivity is now decreased then the temperature of the surface increases and the spectrum shifts blueward. For the case of Fig. 11, as for the asteroids under study, the blueward shift of the spectrum more than compensates for the

---

*The name "Astrid" was introduced by Arnold (1965). The present author prefers to use "(0) Asterid" to denote the hypothetical asteroid.

Fig. 11. Example of how the position of a point on the $E \cdot \Delta^2$ versus B(1,0) plots changes as various parameters are perturbed. This figure illustrates the special situation discussed in the text. The ordinate and the abcissa are in magnitude units, making this a log-log plot.

Fig. 11.

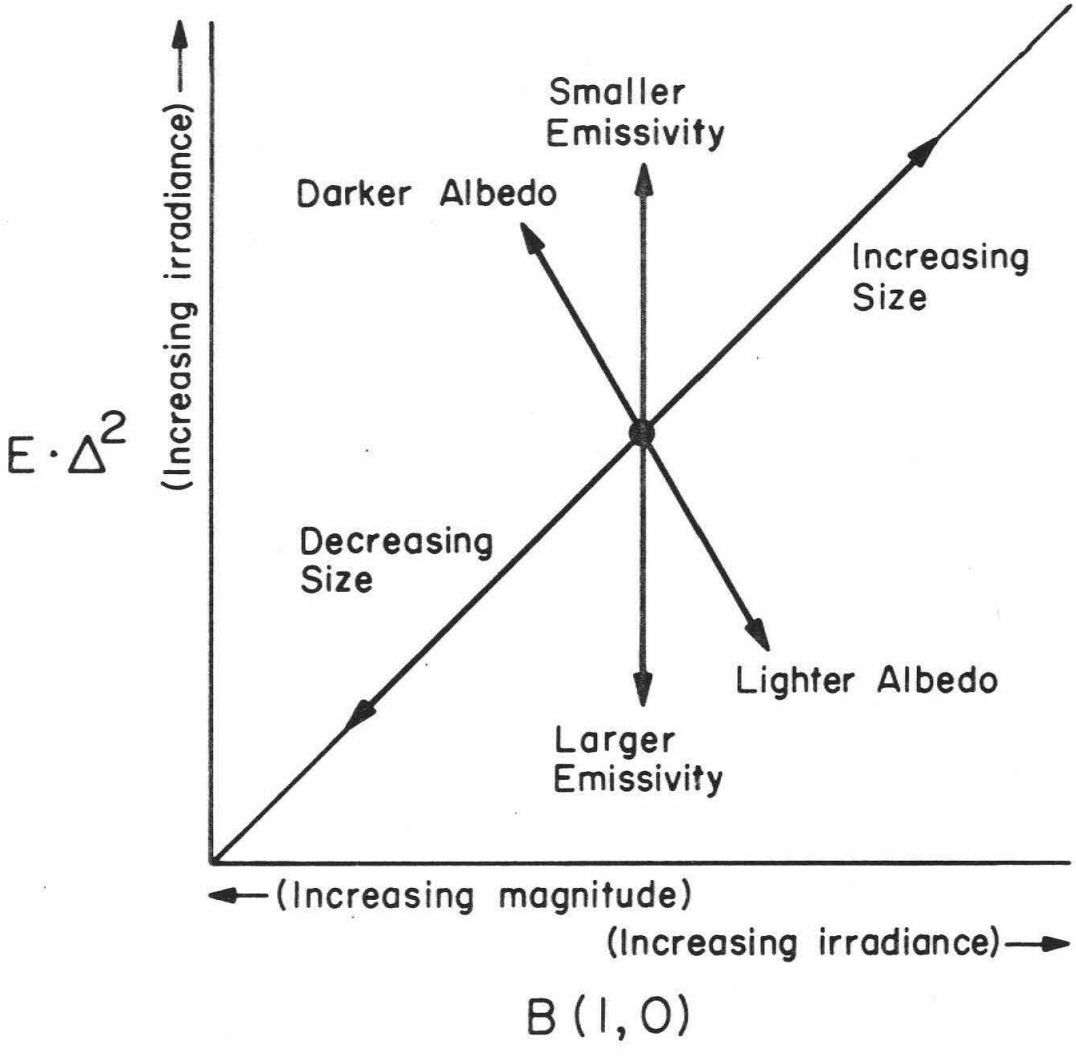
Smaller
Emissivity
Darker Albedo
Increasing
Size
E · Δ²
(Increasing irradiance)
Decreasing
Size
Lighter Albedo
Larger
Emissivity
(Increasing magnitude)
(Increasing irradiance)
B (1, 0)

effect of lower emissivity and the predicted $E \cdot \Delta^2$ increases. On the other hand, for the red slope of a spectrum, the situation would be reversed.

It follows that if two asteroids are at the same distance from the Sun and their points plotted on these diagrams cannot be connected by a line of unit slope then they must have some surface properties that differ. If they can be connected by such a unit-slope line, then nothing is demonstrated uniquely, although it is consistent for them to differ only in size.

Again, the reader is cautioned that there may be some rather large errors on these color plots. For some objects, (674) Rachele for example, it is possible the lightcurve error may amount to 50%. For the faint objects (poor instrumental signal-to-noise ratio) there could be systematic errors in the infrared photometry that might amount to 20-30 percent. These possibilities are taken into consideration when drawing conclusions.

In Fig. 12 the visible and 11.6 μm data show that there are differences between (324) Bamberga on the one hand, and (7) Iris, (80) Sappho, (192) Nausikaa and perhaps (313) Chaldaea. These latter four objects all lie near a line of unit slope and they may have similar surfaces. (6) Hebe and (20) Massalia contrast (19) Fortuna and (145) Adeona. All four objects are about the same distance from the Sun but the latter two are brighter in the infrared than their B(1,0) values alone would suggest. (19) and (145) are also distinct from (7) Iris which is actually closer to the Sun.

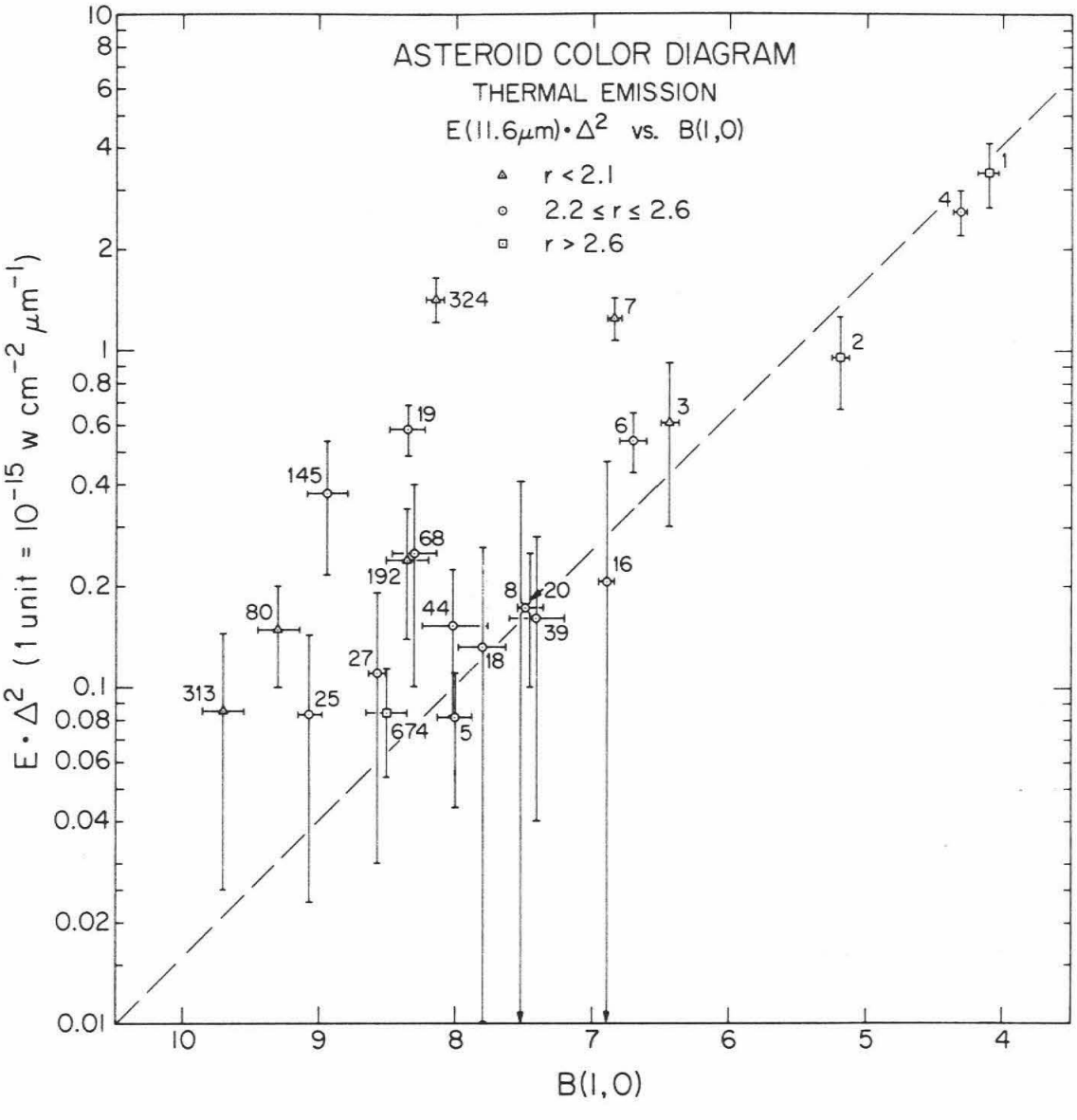

Fig. 12. 11.6 μm color diagram

At 10.5 μm (Fig. 13), (7) Iris and (80) Sappho both clearly have surface properties that differ from (324) Bamberga.

In the 8.5 μm versus B(1,0) plot, Fig. 14, the difference between (1) Ceres and (4) Vesta is noted. (19) Fortuna and (145) Adeona still differ from (6) Hebe as they did in the 11.6 μm data. Also, (324) Bamberga and (7) Iris still differ.

The relative position of (324) Bamberga on all three color plots is consistent with the asteroid having a very low albedo. This is the conclusion that will be drawn later when a model is used to analyze the thermal emission data.

Table 2 tabulates what is currently known about periods of rotation and the lightcurves for these asteroids. Within the limits of present knowledge, all of the above conclusions involve asteroids of roughly comparable periods of rotation.

Observations of (J3) Ganymede and (J4) Callisto

Infrared observations of the Galilean satellites have been reported previously by Murray et al (1964), Low (1965) and Gillett et al (1970). Two of these satellites, J3 and J4, were observed for the present work as a check on the model and on the photometry.

The orbital phase angle, θ, is defined in Fig. 15. In Fig. 16, the $E \cdot \Delta^2$ data for (J3) Ganymede is plotted versus the orbital phase angle. The curve which is drawn with the 11.6 μm data represents the visible photometry ($\lambda = 0.56$ μm) of Johnson (1970, 1971) The curve is only for reference and his data scatter by more than the curve suggests. The reference curve was fit

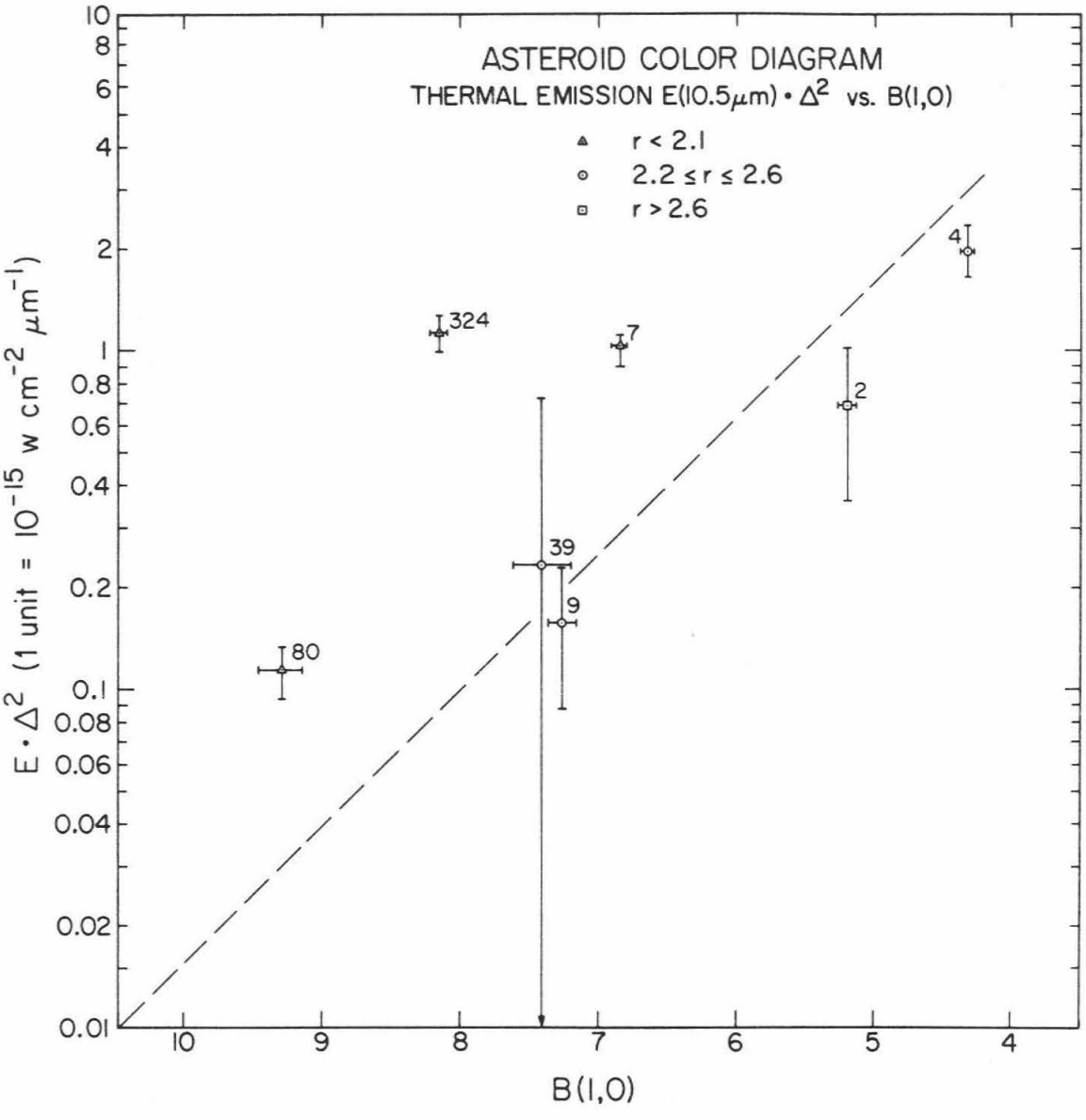

Fig. 13. 10.5 μm color diagram

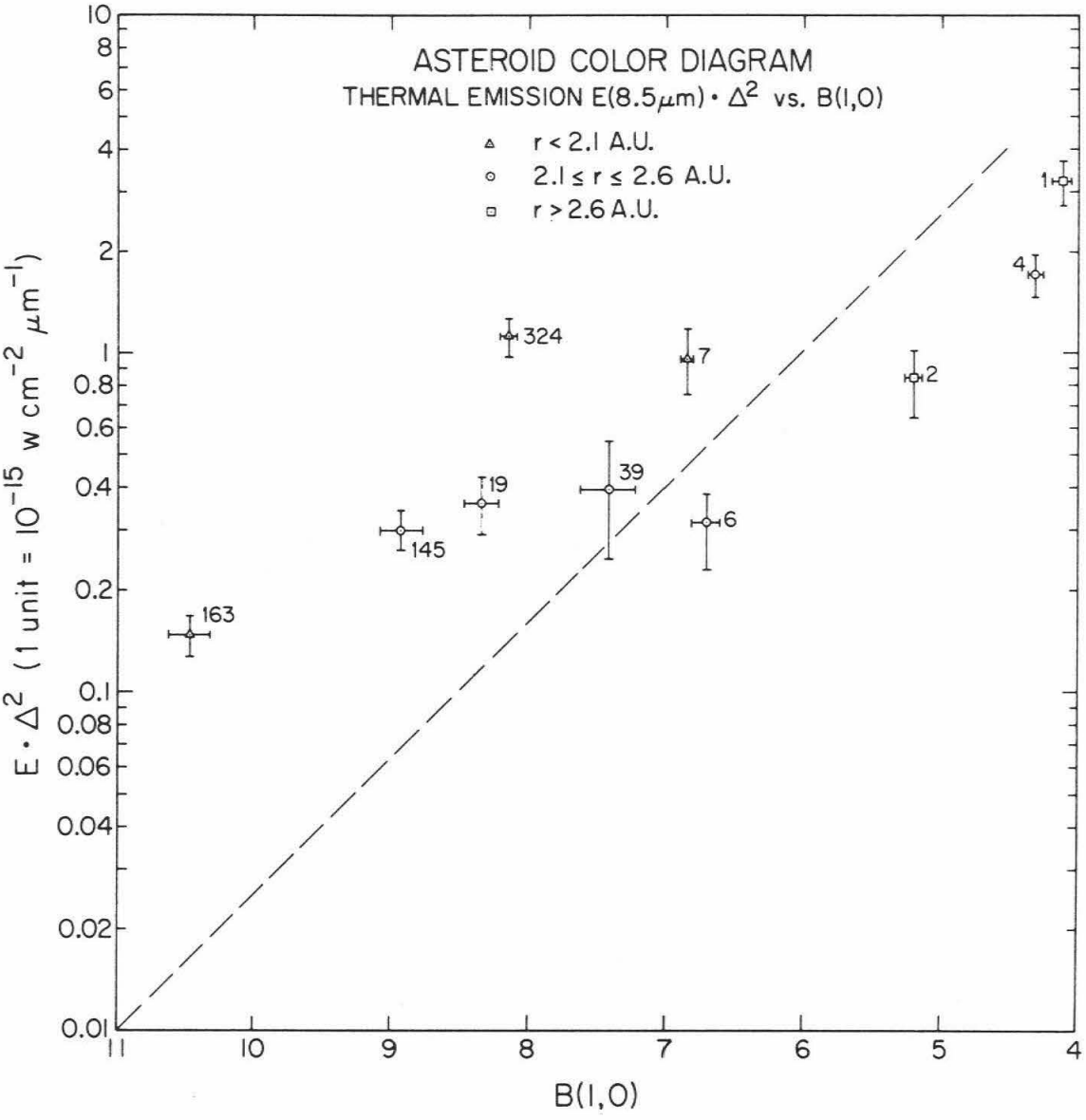

Fig. 14. 8.5 μm color diagram

TABLE 2. ASTEROID DATA (From Gehrels, 1970)

	Name	Rotation Period	Range of observed lightcurve amplitude (mag)
1	Ceres	9.078 hours	0.04
2	Pallas	9 - 12 ?	0.12 - 0.15
3	Juno	7.213	0.15
4	Vesta	5.342 129	0.10 - 0.13
5	Astraea	16.806	0.21 - 0.27
6	Hebe	7.275	0.06 - 0.16
7	Iris	7.135	0.04 - 0.29
8	Flora	13.6	0.01 - 0.04
9	Metis	5.064	0.06 - 0.26
15	Eunomia	6.083	0.42 - 0.53
16	Psyche	4.303	0.11
18	Melpomene	14	0.35
19	Fortuna	7.45	0.25
20	Massalia	8.0980	0.17 - 0.24
25	Phocaea	9.945	0.18
27	Euterpe	8.500	0.15
39	Laetitia	5.138	0.18 - 0.53
44	Nysa	6.418	0.22 - 0.48
68	Leto	—	—
80	Sappho	—	—
145	Adeona	—	—

(continued on next page)

- continued -

TABLE 2. ASTEROID DATA (From Gehrels, 1970)

	Name	Rotation Period	Range of observed lightcurve amplitude (mag)
163	Erigone	—	—
192	Nausikaa	—	—
313	Chaldaea	—	—
324	Bamberga	8 ?	0.07
674	Rachele	—	—

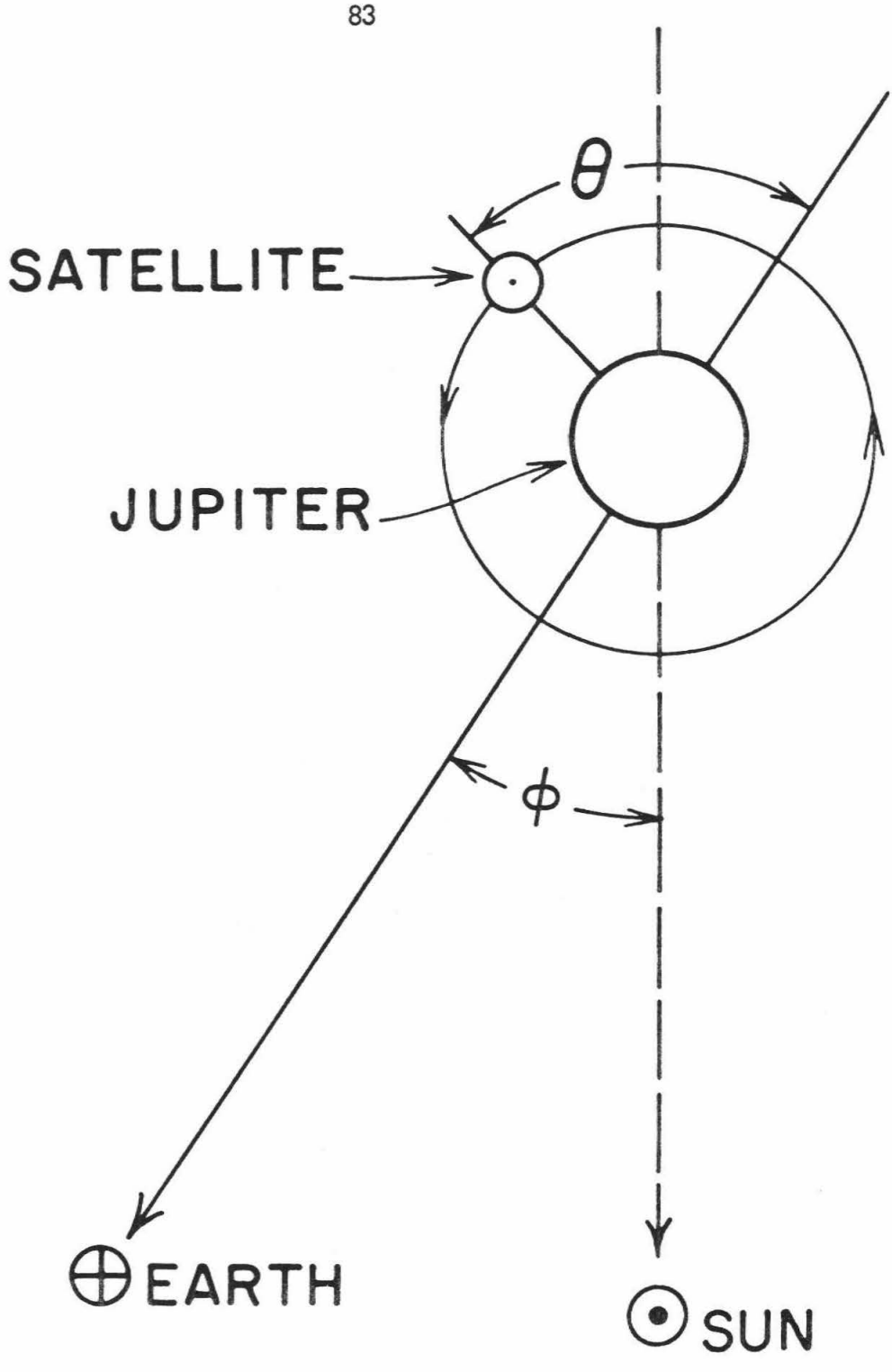

Fig. 15. The orbital phase angle, θ, is the angle between the planetocentric position vector of the satellite and the anti-earth point.

Fig. 16. Observations of (J3) Ganymede plotted as a function of the orbital phase angle θ. The curve shown for reference has been sketched from Johnson's (1970,71) 0.54 μm data. The vertical dimension of this curve has been exaggerated by a factor of 6 and has been fit to the infrared data by translating it vertically.

Fig. 16

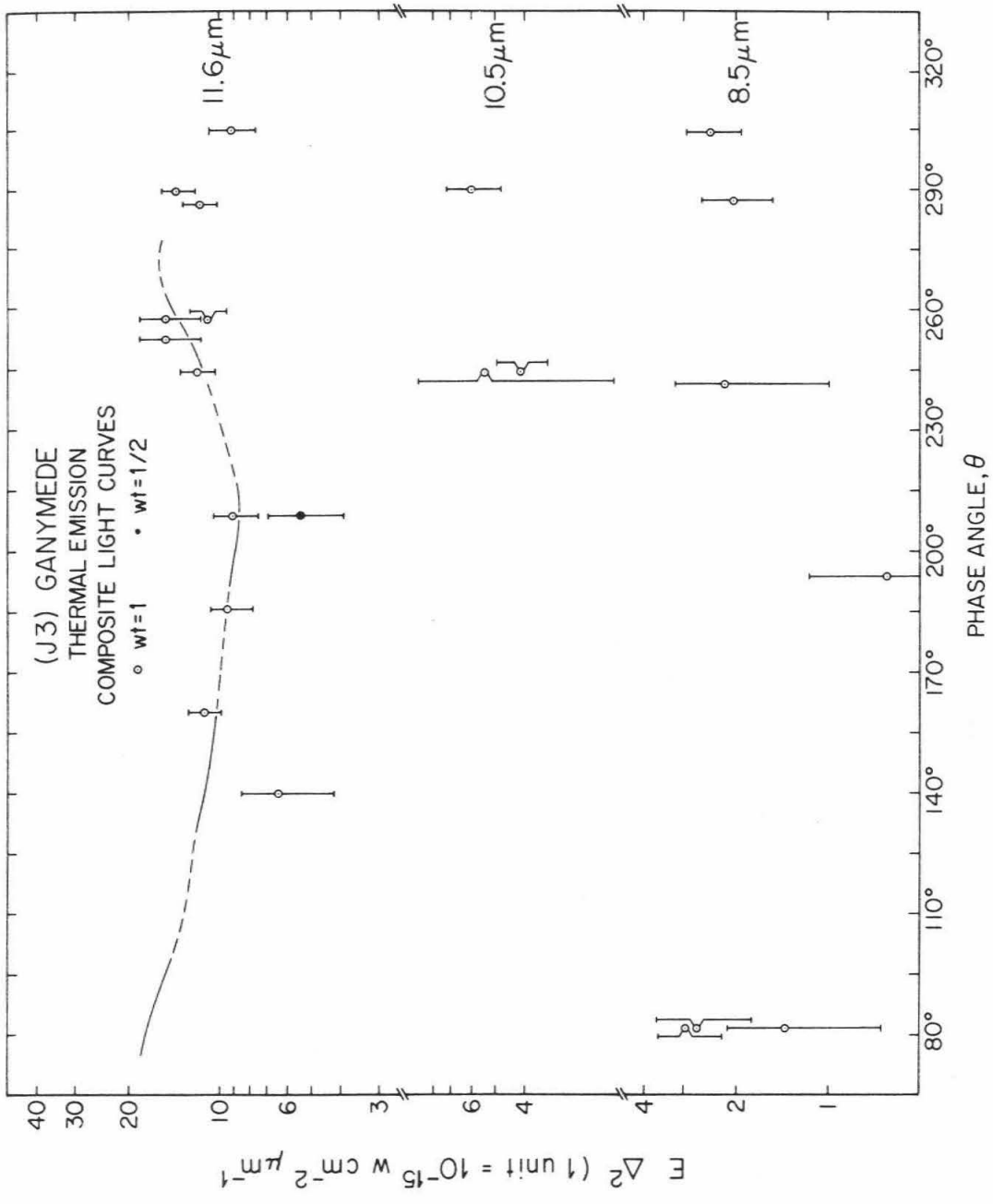
(J3) GANYMEDE
THERMAL EMISSION
COMPOSITE LIGHT CURVES
○ wt=1 • wt=1/2
11.6μm
10.5μm
8.5μm
E Δ² (1 unit = 10⁻¹⁵ w cm⁻² μm⁻¹
PHASE ANGLE, θ
80°
110°
140°
170°
200°
230°
260°
290°
320°

vertically to the 11.6 μm data.

One does not expect a large cross-section variation for a 2,510 km radius object and the shape of the data is probably due to scatter. This interpretation takes the scatter as the range of variation at phase angles for which several data are available.

The $E \cdot \Delta^2$ versus rotational phase angle information for (J4) Callisto is presented in Fig. 17. At 11.6 μm the infrared data appear to have two rather distinct values with the transition between these levels occurring close to where Stebbins (1927), Stebbins and Jacobsen (1928) and Johnson (1970, 1971) have observed a gross change in the visible lightcurve.

At 8.5 μm the J4 data show an interesting shape. The 8.5 μm data undergo a large change in $E \cdot \Delta^2$ while at the same phase angles the 11.6 μm data are unchanged. If this feature is real it would imply a spatial and a wavelength dependence of emissivity. The reason for suspecting these 8.5 μm data is that they do not have a very good instrumental signal-to-noise ratio. The largest value of $E \cdot \Delta^2$ at 8.5 μm barely produces a discernible stripchart deflection. Thus, it can be argued that large scatter, systematic errors or both may be present. The shape of the curve really depends upon the single point at $\theta \sim 235°$. Considering the errors possible in this type of photometry, a single observation is not diagnostic and for the present the 8.5 μm feature is regarded as fortuitous.

Fig. 17. Observations of (J4) Callisto plotted as a function of orbital phase angle, θ. The infrared data appear to pass through a transition near $\theta = 180$ to 200°. Visible-wavelength photometry obtained by Stebbins (1927), Stebbins and Jacobsen (1928) and Johnson (1970, 1971) has a 15-20 percent change in amplitude which is centered at $\theta \sim 180°$.

Fig. 17

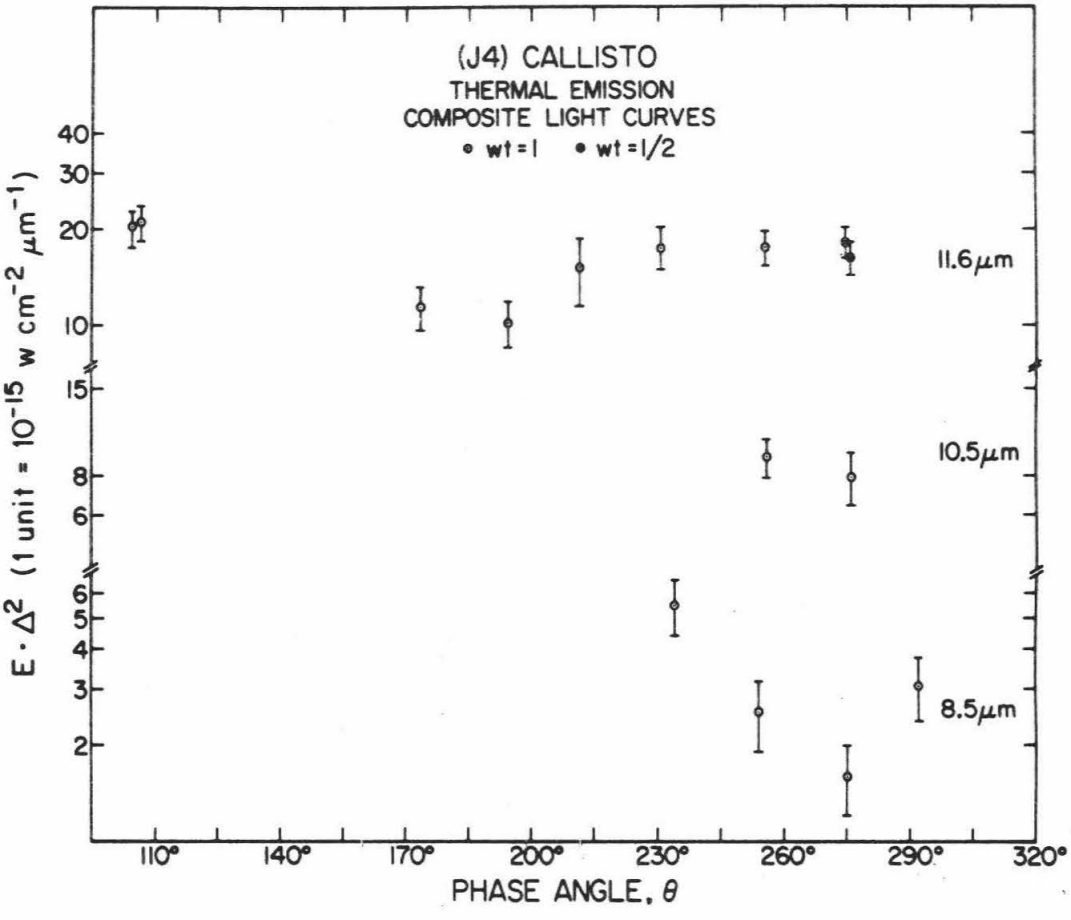
(J4) CALLISTO
THERMAL EMISSION
COMPOSITE LIGHT CURVES
• wt = 1 • wt = 1/2
11.6μm
10.5μm
8.5μm
E · Δ² (1 unit = 10⁻¹⁵ w cm⁻² μm⁻¹)
PHASE ANGLE, θ
110°
140°
170°
200°
230°
260°
290°
320°

In Table 3, the J3 and J4 photometry by other observers is summarized and reduced to $E \cdot \Delta^2$. The work of Gillett et al (1970) is that most comparable to this study. Their observations show about the same irradiances as this work but Gillett et al do not give either the rotational phase angle, θ, nor the date upon which their observations were obtained. So, it is not clear what is being compared. With the possibility of a variation with θ, it cannot yet be concluded that any of the $E \cdot \Delta^2$ values in Table 3 are out of line.

Infrared photometry of the Galilean satellites is currently being carried out as a Ph.D. thesis by Olav Hansen. His detector and photometer combination has a better signal-to-noise ratio than the one used in this study and some of these questions about the lightcurve variations of the satellites may be resolved.

Table 3 Observations of (J3) Ganymede and (J4) Callisto

Authors	λ^{-1} (μm^{-1})	(J3) Ganymede Brightness Temperature	$E \cdot \Delta^2$ (1 Unit = 10^{-15} W $cm^{-2} \mu m^{-1}$)	(J4) Callisto Brightness Temperature	$E \cdot \Delta^2$ (1 Unit = 10^{-15} W $cm^{-2} \mu m^{-1}$)
Murray, et al (1964)	8-14	154.5° K	10.7*	168.5° K	17.5*
Low, (1965)	8-14	144±5	5.5±1.9*	159±5	10.5±2.8*
Gillett, et al (1970)	8-8.8	145±3	1.87±0.46**	160±3	4.5±0.9**
	10-12	143±3	7.0± 1.4**	160±3	14.5±2.3**
Present Work	8.5		2.17±0.61		3.2±2.9
	10.5		5.0±1.2		8.50±0.84
	11.6		10.1±2.9		16.4±3.6

* Radii used: J3 = 2550 km, J4 = 2360 km, λ = 10.2 μm

**Radii used: J3 = 2510 km, J4 = 2230 km, λ = 8.4, 11.0 μm

III. THE THERMAL MODEL

This section develops a thermal model for use in interpretation of the asteroid and satellite observations. There is good reason to believe that the surfaces of the larger asteroids have much in common with that of the Moon. In the visible-wavelength region both polarimetry and the integral phase effect observations support this idea. Veverka (1970a,b) has studied the polarization of light from (4) Vesta and (8) Flora. He interprets his data as implying a porous or particulate surface layer. The brightness versus phase data for (4) Vesta is strikingly similar to that for the Moon and this fact has been noted by Gehrels (1967) and Veverka (1970b). In Fig. 18 the visible-wavelength phase curves are plotted for several bodies. The (4) Vesta curve is from Gehrels (1967); the Moon from Gehrels et al (1964); the Galilean satellites from the work of Johnson (1970, 1971) and Stebbins (1927); and Mars from O'Leary and Rea (1968). J3, which differs more from the Moon on this plot than does (4) Vesta, is thought to have a porous or particulate surface layer. This belief is substantiated by the low values of thermal inertia which are implied by the eclipse cooling observed by Murray et al (1965) and Morrison et al (1971).

Another line of argument is by analogy with the Moon and Mars. The large asteroids probably have surface regoliths simply because they retain some of the debris formed by impacts. Consider the limiting case of hyper-velocity impact. From the mass of (4) Vesta ($\sim 2.4 \times 10^{23}$ g; Hertz 1968), the escape

Fig. 18. Visible-wavelength phase data. The relative magnitudes for the Galilean satellites were computed from a mixture of data from Johnson (1970, 1971) and Stebbins (1927):

$$m_1 = 0.0360\,\varphi - 0.00100\,\varphi^2$$
$$m_2 = 0.0262\,\varphi - 0.00125\,\varphi^2$$
$$m_3 = 0.0273\,\varphi - 0.00066\,\varphi^2$$
$$m_4 = 0.0830\,\varphi - 0.00270\,\varphi^2$$

Other data are from references cited in the text.

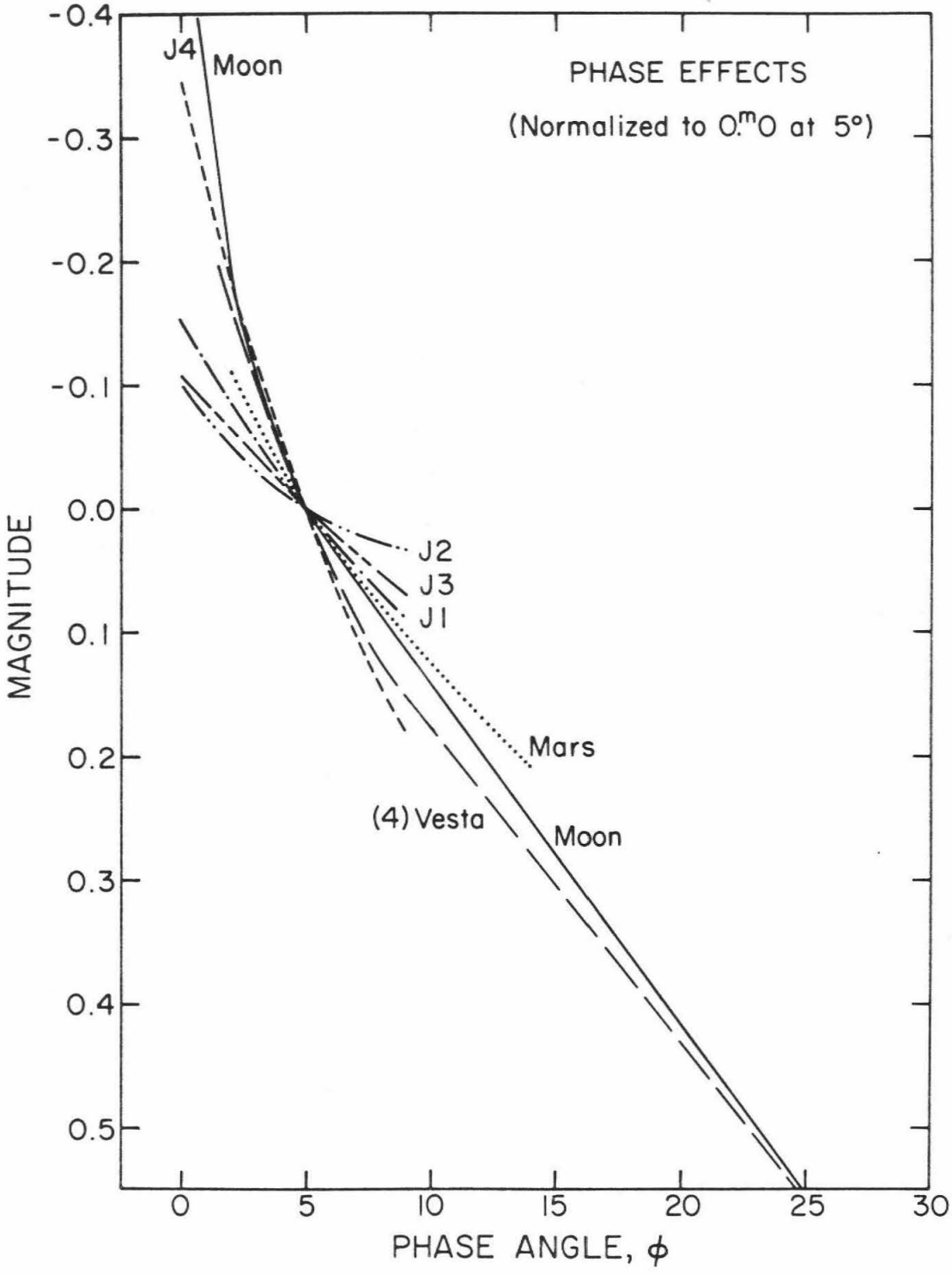
PHASE EFFECTS
(Normalized to 0.^m0 at 5°)
J4
Moon
J2
J3
J1
Mars
(4) Vesta
Moon
MAGNITUDE
PHASE ANGLE, φ
-0.4
-0.3
-0.2
-0.1
0.0
0.1
0.2
0.3
0.4
0.5
0
5
10
15
20
25
30

Fig. 18

velocity is estimated to be ~400m/sec. By using the observed laboratory relationship between the ejection velocity for a debris particle and the cumulative mass of debris that is ejected at even high velocity (Gault et al 1962, Fig. 10), one can estimate the percentage of ejecta that returns to the asteroid. For (4) Vesta this estimate amounts to more than ninety-five percent when a two-hundred kilometer radius is used for the asteroid. For these reasons the Moon is taken as the basis for a model. Asteroids and satellites will be modeled by perturbing the size, albedo, emissivity and period of rotation. All of the other parameters in the model will be set equal to those values derived from telescopic observations of the Moon.

Previous Work

The first studies using detailed thermal models to explain the Moon's infrared emission were made by Wesselink (1948), Jaeger and Harper (1950), and Jaeger (1953a,b). Their general approach is followed because it is adequate enough for the asteroid observations that are to be studied. Readers interested in more recent developments in this field should consult Watson (1964), Linsky (1966), Buhl et al (1968a,b), Winter and Saari (1969) and Winter and Krupp (1970).

Modifications of Wesselink's method have been used by Hugh Kieffer (1971, personal communication) in calculation model surface temperatures. In this study Kieffer's computer program is used to produce a map of the planetary surface temperature. Given this map the various radiation parameters can then be computed.

Description of the Model

The model partitions the surface of a rotating sphere into 432 area elements. The temperature of each element is found by solving the linear heat flow equation with a radiation and insolation boundary condition for an infinite half-space in which k, ρ, c, and $\eta = k/\rho c$ are the thermal conductivity, density, specific heat and diffusivity. These parameters are assumed to have constant values. The linear heat flow equation is

$$\frac{\partial^2 T}{\partial X^2} - \frac{1}{\eta} \frac{\partial T}{\partial t} = 0 \qquad (2)$$

where

T = temperature, °K
t = time, seconds
X = depth below the surface, cm.

The boundary condition equation at x= 0 is

$$\frac{\partial T}{\partial X} = \epsilon \sigma T^4 - q_A (i,r), \quad -\frac{\pi}{2} < i < \frac{\pi}{2} \qquad (3)$$

$$= \epsilon \sigma T^4, \quad \text{i other} \qquad (4)$$

where:

ε = the effective emissivity
σ = the Stefan-Boltzmann constant
$q_A(i,r)$ = absorbed heat from the sun as a function of angle of isolation, i, and distance from the sun, r.

The function

$$q_A(i,r) = \cos(i)\, E_\odot(r)\ (1-A), \quad -\frac{\pi}{2} < i < \frac{\pi}{2} \tag{5}$$

$E_\odot(r)$ is the solar radiation received at the distance of the model from the sun. A is the bolometric Bond albedo and

$$A = \frac{\int_0^\infty a(\lambda)\, E_\odot(\lambda, r)\, d\lambda}{\int_0^\infty E_\odot(\lambda, r)\, d\lambda} \tag{6}$$

in which $a(\lambda)$ is the monochromatic Bond albedo and $E_\odot(\lambda,r)$ the spectral irradiance of the sun at distance r.

An explicit solution cannot be obtained because the unknown temperature in the boundary condition occurs raised to the fourth power; numerical methods must be used. A number of methods have been employed and discussions are given by Wesselink (1948), Jaeger and Harper (1950), Jaeger (1953 a, b) and Ingrao et al (1966). Of the published discussions the method to be used here most closely resembles that of Wesselink (1948).

The actual numerical calculations for the model temperatures are done using a computer program developed by Hugh Kieffer (1971; personal communication) for computing planetary surface temperatures.

Kieffer's program uses the method of finite differences with layer thicknesses that increase exponentially with depth. The depth parameter is scaled in units of $(kP/\pi\rho c)^{1/2}$ and this is the thermal skin depth or the depth at which the periodic thermal waves propagating into the surface have been reduced in amplitude by 1/e. For the calculations involved in this thesis 12 layers were used with the bottom layer placed at a depth of 5 scale units--or where the periodic temperature change is less than one percent. The bottom of the lowest layer is assumed to be insulating and the temperature gradient in the uppermost layer is assumed to be uniform. A perturbation solution of the quartic boundary condition equation is made in each iteration in order to calculate the surface temperature. The calculations start at the evening terminator with the initial temperature distribution (with depth) of a perfect conductor. At the end of the second day a second-degree perturbation is applied to the temperature profile. This sets the mean lower layer temperature to equal the mean surface temperature. The time increment used is 1/480 of a day (revolution) and the linear increment is a function of depth due to the exponential layering. A solution is considered to have been found when the rms change in temperature between different days is less than 0.1°K. The resultant temperatures are printed out for each 15° of planetary longitude. This process is carried out separately for each latitude with the latitude spacing being 10 degrees. The output is a temperature map which is used as the input data for an irradiance calculation routine. This routine

computes the radiation geometry and the projected area for each surface element of area ΔS. The radiant intensity ΔI contributed by each surface element is evaluated using the spectral radiant power for a blackbody ($B(\lambda,T)$), the effective emissivity (ϵ), and the projection factor for the unit vectors for the direction of the Earth and the local surface normal ($\hat{n}_\oplus \cdot \hat{n}$). Thus,

$$\Delta I(\lambda,T) = \frac{\epsilon}{\pi} (\hat{n}_\oplus \cdot \hat{n})\, B(\lambda,T)\, \Delta S, \quad (\hat{n}_\oplus \cdot \hat{n}) > 0 \qquad (7a)$$

$$= 0, \quad (\hat{n}_\oplus \cdot \hat{n}) \leq 0 \qquad (7b)$$

The units of ΔI are W sr^{-1} μm^{-1}. The ΔI's are summed over the sphere and the irradiance falling on a square centimeter at 1 AU from the model is calculated. This computed irradiance corresponds to the observational quantity $E \cdot \Delta^2$.

As a check on the accuracy of the computer program, the total amount of energy radiated at the end is computed and compared with the amount that was absorbed. To slide rule accuracy, the radiated energy is found to equal that initially absorbed.

The fixed parameters adopted for the model are: density $\rho = 1.5$ g cm^{-3}, specific heat capacity $C = 0.2$ cal g^{-1} $°K^{-1}$, and $(k\rho c)^{1/2} = 0.001$ cal cm^{-2} $°K^{-1}$ $sec^{-1/2}$. These values are typical of the parameters that have been derived for the Moon from Earth-based telescopic observations of lunation and eclipse cooling.

Lateral heat transport is not important in this model because $\Delta X \ll \sqrt{\Delta S}$.

Several computer runs were made for the Moon using an albedo of 0.07 and unit effective emissivity. The results for the lunar equator were in agreement with Wesselink's (1948) calculations. Calculations for (J3) Ganymede, however, did not agree with Richardson and Shum's (1968) temperatures when their assumed data for J3 were used. Their calculation is incorrect because the subsolar point temperature they give for unit emissivity is higher than the solar equilibrium temperature.

Phase Functions and Spectra

The important observational parameters that are implicit in the model are the emitted radiation beam pattern (phase function) and the thermal emission spectrum. These are the only properties of the model that can be tested by integral photometry. Unfortunately, for observations with Earth-based telescopes, only the first ten to thirty degrees of the phase function are accessible and the spectrum can only be observed at wavelengths where our atmosphere is transparent. Fig. 19 shows some model beam patterns for (0) Asterid . The thermal emission spectrum is shown with several other spectra in Fig. 20. These parameters vary from one situation to the other and they provide the relationship between the irradiance, $E \cdot \Delta^2$, and the total radiated energy.

Fig. 19. Cross sections of model emission beam patterns.

(a) The pattern the Moon would have if it were placed at a distance of 3 AU from the sun. The Moon is the origin for the plot and the cross section lies in the ecliptic plane. The rotation pole points directly up, out of the paper. The radiation intensity at each wavelength is normalized to the value in the direction of the Sun.

(b) Now the Moon is spun-up to equal the period of Vesta, 5.34 hours. The radiation lobe shifts to a position of about 13 or 14 degrees. Also the shape of the pattern becomes a more pronounced function of wavelength.

(c) This is a polar cross section through (b). The axis of rotation lies in the plane of the paper and is perpendicular to the direction to the Sun.

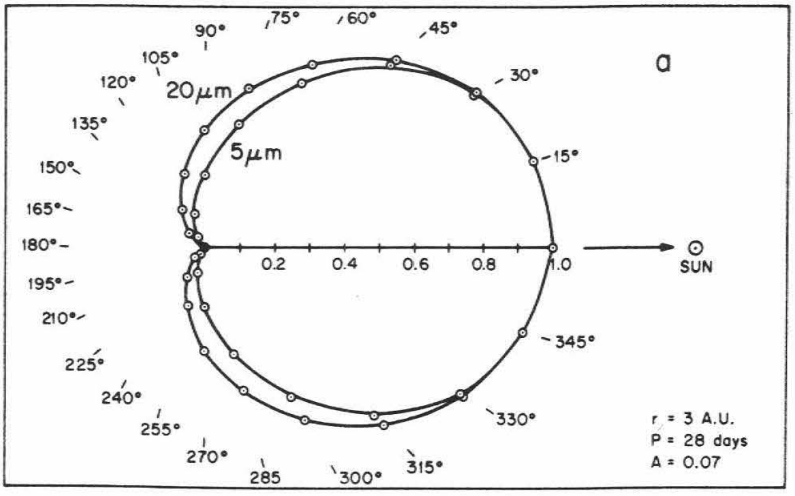
a
20μm
5μm
90°
75°
60°
45°
30°
15°
105°
120°
135°
150°
165°
180°
195°
210°
225°
240°
255°
270°
285
300°
315°
330°
345°
0.2
0.4
0.6
0.8
1.0
SUN
r = 3 A.U.
P = 28 days
A = 0.07

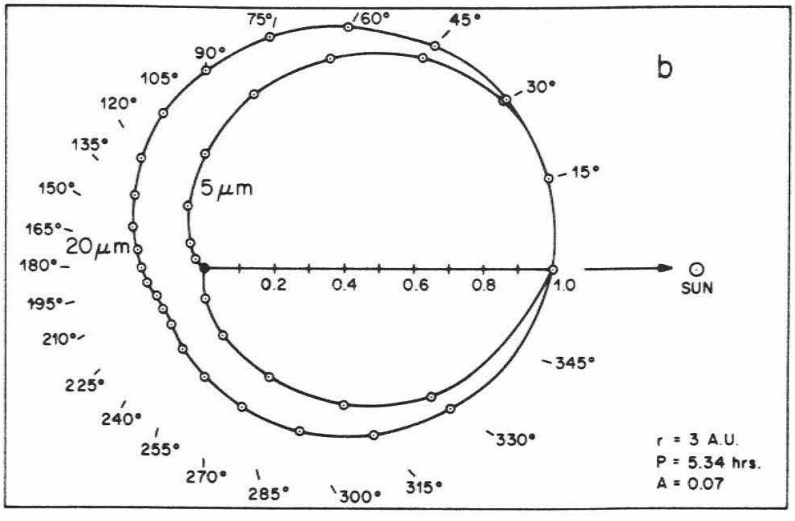
b
5μm
20μm
90°
75°
60°
45°
30°
15°
105°
120°
135°
150°
165°
180°
195°
210°
225°
240°
255°
270°
285°
300°
315°
330°
345°
0.2
0.4
0.6
0.8
1.0
SUN
r = 3 A.U.
P = 5.34 hrs.
A = 0.07

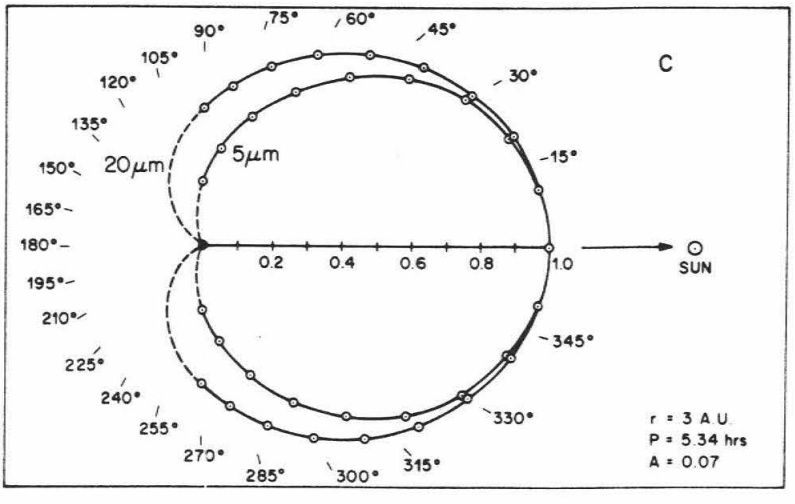
c
20μm
5μm
90°
75°
60°
45°
30°
15°
105°
120°
135°
150°
165°
180°
195°
210°
225°
240°
255°
270°
285°
300°
315°
330°
345°
0.2
0.4
0.6
0.8
1.0
SUN
r = 3 A.U.
P = 5.34 hrs
A = 0.07

Fig. 19

Fig. 20. Model and reference spectra corresponding to the model beam pattern in Figs. 19b and 19c.

(a) The total spectral radiant power (W μm^{-1}) from the model if it radiated all the absorbed insolation as a uniform-temperature blackbody.

(b) Integrated spectral radiant power from the model.

(c) The spectral radiance (W $cm^{-2} \mu m^{-1} sr^{-1}$) in the direction of the Sun. This is the observable spectrum when the asteroid is at opposition.

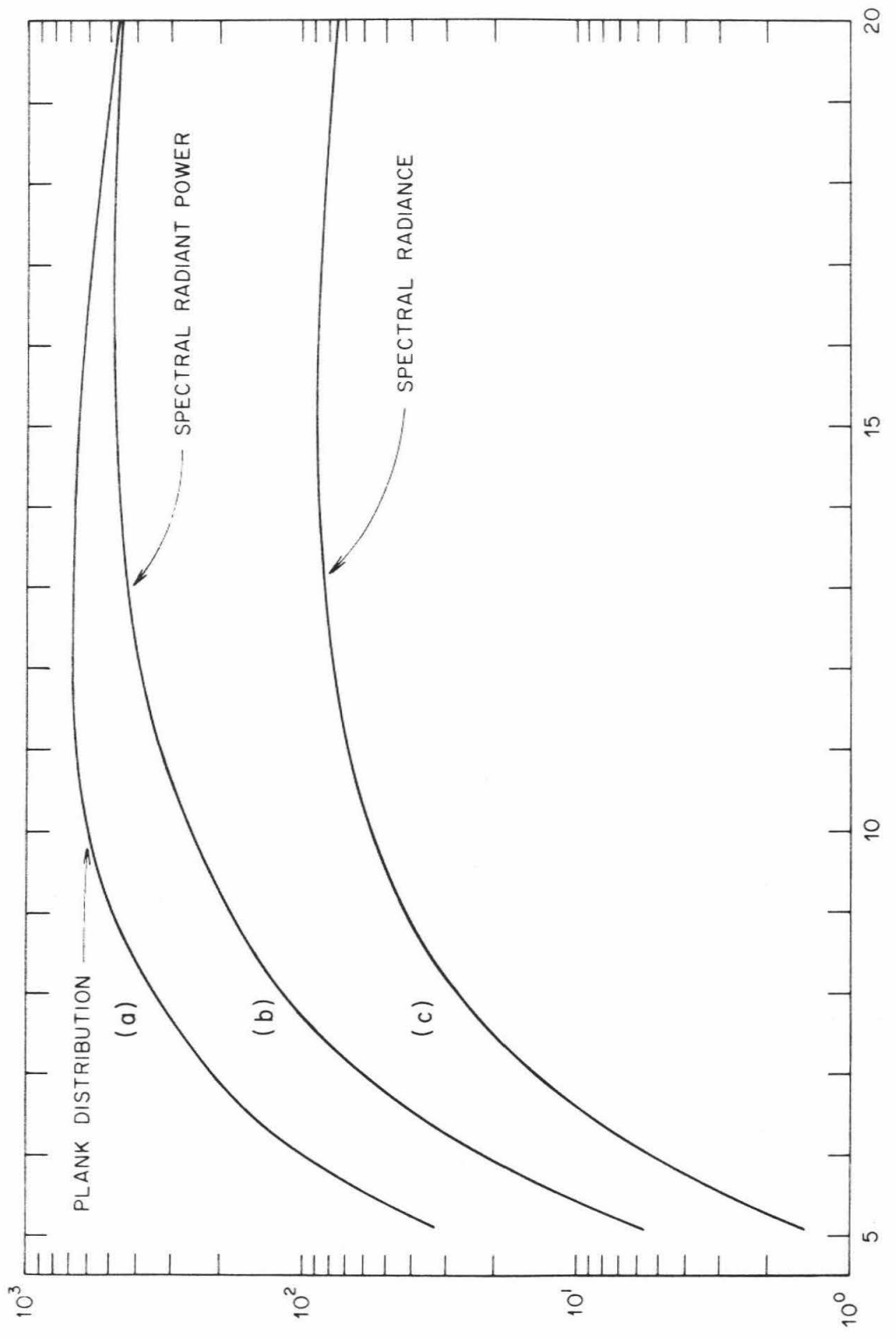
PLANK DISTRIBUTION
(a)
(b)
(c)
SPECTRAL RADIANT POWER
SPECTRAL RADIANCE
10^3
10^2
10^1
10^0
RELATIVE UNITS
5
10
15
20
WAVELENGTH, λ (in μm)

Fig. 20

IV. ANALYSIS OF THE OBSERVATIONS

(J3) Ganymede and (J4) Callisto

The comparison of the model with observations of J3 and J4 is important because these satellites were observed with the same instrument and techniques as were the asteroids. This provides a check for any gross systematic errors in either photometry or the model analysis because there are reasonable estimates for some of the photometric properties of these satellites.

The radius is one of the parameters required by the model. In order to understand the reliability of this value a short digression is necessary to study the angular diameter measurements. Dollfus (1970) has published a recent and convenient tabulation of this work which extends back through the last one and a half centuries. From the tabulation the average angular diameter measured by each instrumental method is plotted versus a reference method (in this case Dollfus' double image micrometer measurements) in Fig. 21. Different methods give different values, but the overall trend is that the differences between methods are not strongly correlated with the angular size. The greatest discrepancies are for J3. Dollfus (1970) has suggested that this may be due to albedo spots on that satellite's surface. The diameter to be used here for J3 will be the mean of the average values obtained by each method. Thus the diameter for J3 is $1''.36 \pm 0''.08$ or $(5.13 \pm 0.30) \times 10^3$ km and J4 is $1''.26 \pm 0.06$ or $(4.75 \pm 0.30) \times 10^3$ km. The 0.08 second of arc error for J3 will be used as an estimate of the systematic instrumental error for disk measurements.

Fig. 21. Disk diameters. The ordinate is the average angular diameter obtained by a given instrumental method. The abscissa is the double image micrometer diameter from Dollfus. The micrometer data for (4) Vesta was measured by Barnard and the interferometry is by Hamy. Data is that tabulated by Dollfus (1970). Satellite data is for a distance of 5.203 AU; for the asteroid it is 1.0 AU.

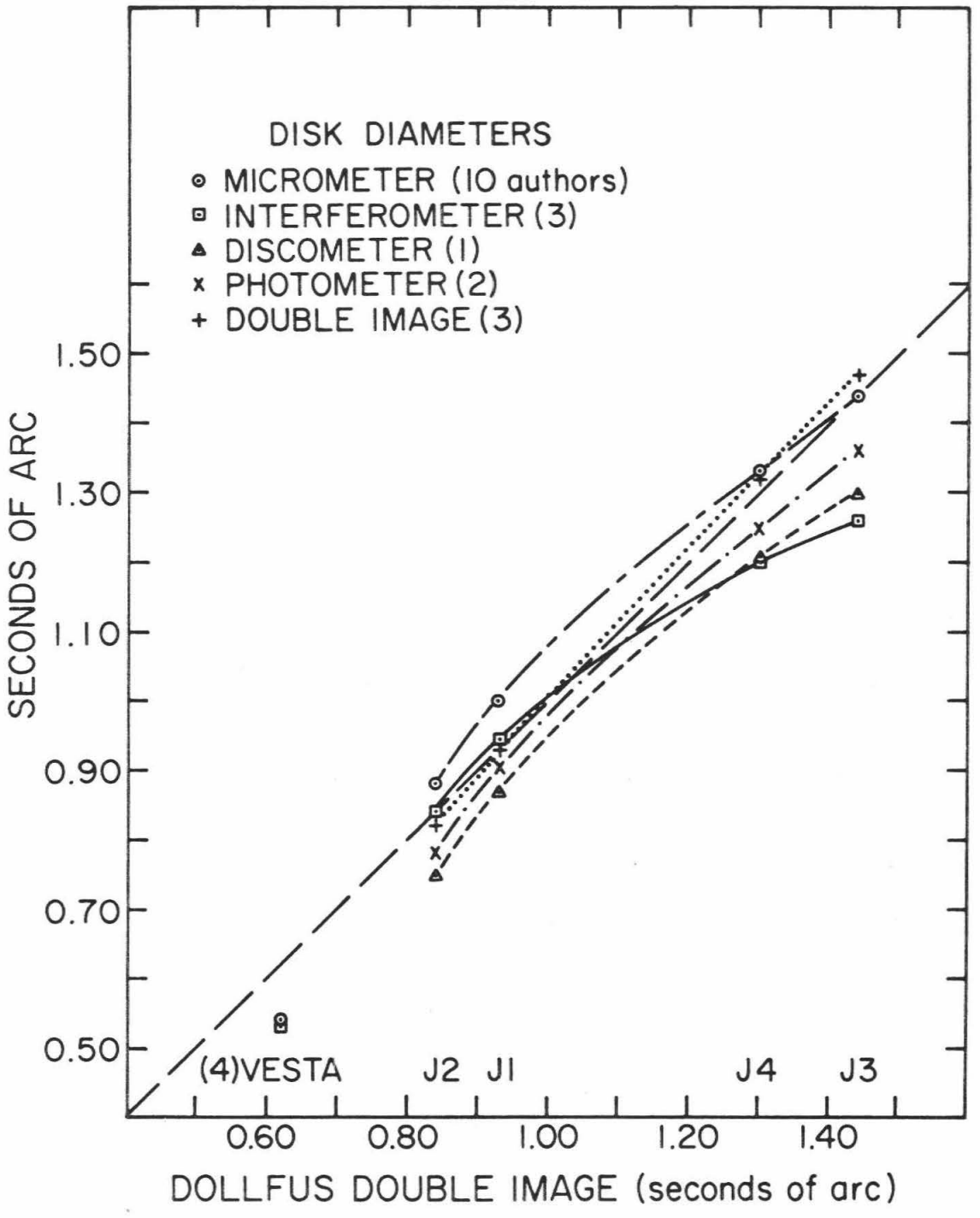
DISK DIAMETERS
MICROMETER (10 authors)
INTERFEROMETER (3)
DISCOMETER (1)
PHOTOMETER (2)
DOUBLE IMAGE (3)
SECONDS OF ARC
1.50
1.30
1.10
0.90
0.70
0.50
(4)VESTA
J2
J1
J4
J3
0.60
0.80
1.00
1.20
1.40
DOLLFUS DOUBLE IMAGE (seconds of arc)

Fig. 21

Recently (J1) Io occulted a star and the preliminary size that has been determined for it is consistent with the above analysis. The final results are not yet available but the preliminary results put J1 at about 0.94 seconds of arc (O'Leary 1971, private communication). This datum falls amongst the points plotted for J1 in Fig. 21.

With the above radii and the rotation periods for J3 and J4 from C.W. Allen (1963), the model was run for a variety of values for A and ε. The model fluxes and the observations of J3 are compared in Fig. 22. The ordinate for 22a and b is $E \cdot \Delta^2$. For 22c the ordinate is the 11.6 μm/8.5 μm ratio. The abscissa for all plots is the model albedo, A. The mean and standard deviation for the observations plot as horizontal lines. Points where the model was run are shown by filled circles. These points lie on nearly straight lines and the dashed lines are a graphical approximation. Since the radius is only accurate to $\sim$10%, the predicted model fluxes are expected to have a 20 percent uncertainty. Thus each dashed line represents the center of a band of values that are compatible with the model.

It can be seen by inspection of Fig. 22 that if $\varepsilon = 1.0$, the best solution for A is about 0.08 to 0.1. However, other values of ε yield other A's and, in fact, the ratio and each wavelength define a region in the albedo-emissivity (A-ε) plane. The solution that will be sought is the region in the A-ε plane where all of the data can be satisfied to within the stated observational errors.

Fig. 22. Model predictions compared with the observations: (a) 11.6 μm, (b) 8.5 μm and (c) 11.6 μm/8.5 μm ratio. The abscissa is the model albedo, A, which corresponds to the bolometric Bond albedo. The ordinate for (a) and (b) is $E \cdot \Delta^2$ and for (c) it is the 11.6 μm/8.5 μm ratio. The solid horizontal lines are the mean and the mean plus and minus a standard deviation. Model predictions are computed for several values of the effective emissivity, ε, and are shown as dashed curves.

Fig. 22

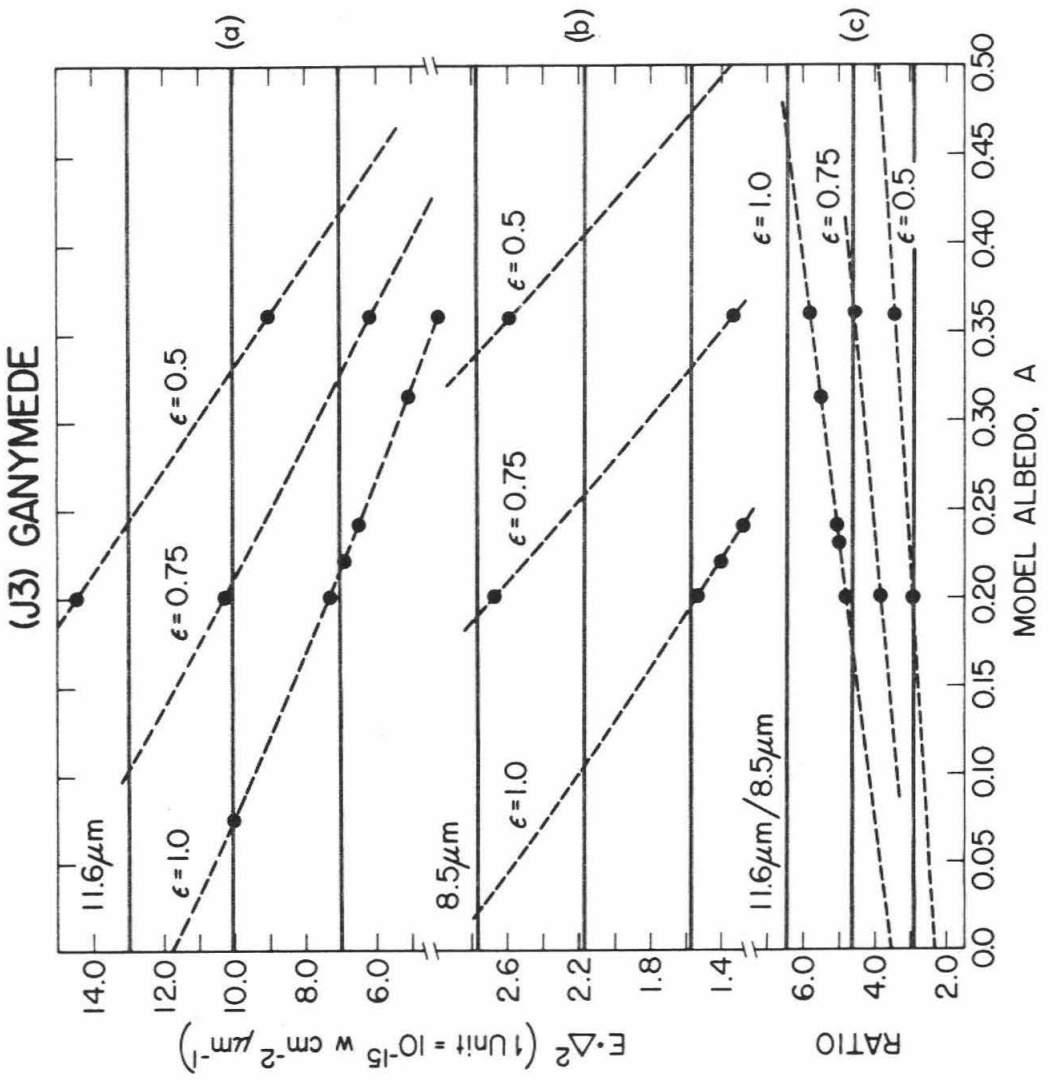
(J3) GANYMEDE
(a)
(b)
(c)
11.6μm
8.5μm
11.6μm/8.5μm
ε=1.0
ε=0.75
ε=0.5
E·Δ² (1 Unit = 10⁻¹⁵ w cm⁻² μm⁻¹)
RATIO
MODEL ALBEDO, A
14.0
12.0
10.0
8.0
6.0
2.6
2.2
1.8
1.4
6.0
4.0
2.0
0.0
0.05
0.10
0.15
0.20
0.25
0.30
0.35
0.40
0.45
0.50

The transfer is carried out graphically from Fig. 22 by replotting in the A-ϵ plane the intersections between dashed and solid lines. Regions are then defined by drawing curves through these transfer points. The area common to all of the data is outlined by a heavy line in Fig. 23. Any point in this region yields a combination of albedo and emissivity that satisfies all the observations.

For real objects an emissivity of greater than 0.75 is expected, especially if the surface is composed of silicates. This level is indicated by a dashed line. With the constraint of $\epsilon > 0.75$, the model albedo of J3 is between 0.02 and 0.3. If $\epsilon = 1.0$ then A is about 0.12 ± 0.10.

From his geometric albedo, Johnson (1970, 1971) has computed the Bond albedo of J3 at 0.56 μm to be 0.359 by assuming that the lunar phase integral applies ($q = 0.585$ from Harris 1961). Using his spectrophotometry of J3 and the irradiance of the Sun (Labs and Neckel 1968), the conversion factor between the bolometric and the $\lambda = 0.56$ μm Bond albedos can be found. Johnson's value, then, corresponds to $A \sim 0.31$ (also after conversion to a 5,130 km diameter). This albedo is a bit high compared to the present work. However, Johnson's lunar value cannot be ruled out because it comes within the error bars of the present work.

It is interesting to note that if Dollfus' double image micrometer diameter of 1."47 had been used, Johnson's A would be ~ 0.23 and the infrared A ($\epsilon = 1.0$) would be centered at $A \sim 0.15$.

It is concluded that the model explains the observations to within the limits of uncertainty.

Fig. 23. (J3) Ganymede in the A-ε plane. The regions which satisfy the 8.5 μm and the 11.6μ m data are specified by two sets of three lines. The three lines correspond to values of A and ε that satisfy the mean, and the mean plus and minus one standard deviation. The triangular region bounds all points that are within the standard-deviation error bars of all of the observational data. The 8.5μ m data set the left boundary and the 11.6μ m set the right. The error bars for the 11.6 μm/8.5 μm ratio are so large that they don't help. The error bar near the bottom shows how a 28 percent error would affect the ε = 0.75, 8.5μm point. This estimate was arrived at by assuming 20 percent errors for both the model and the photometry.

Fig. 23

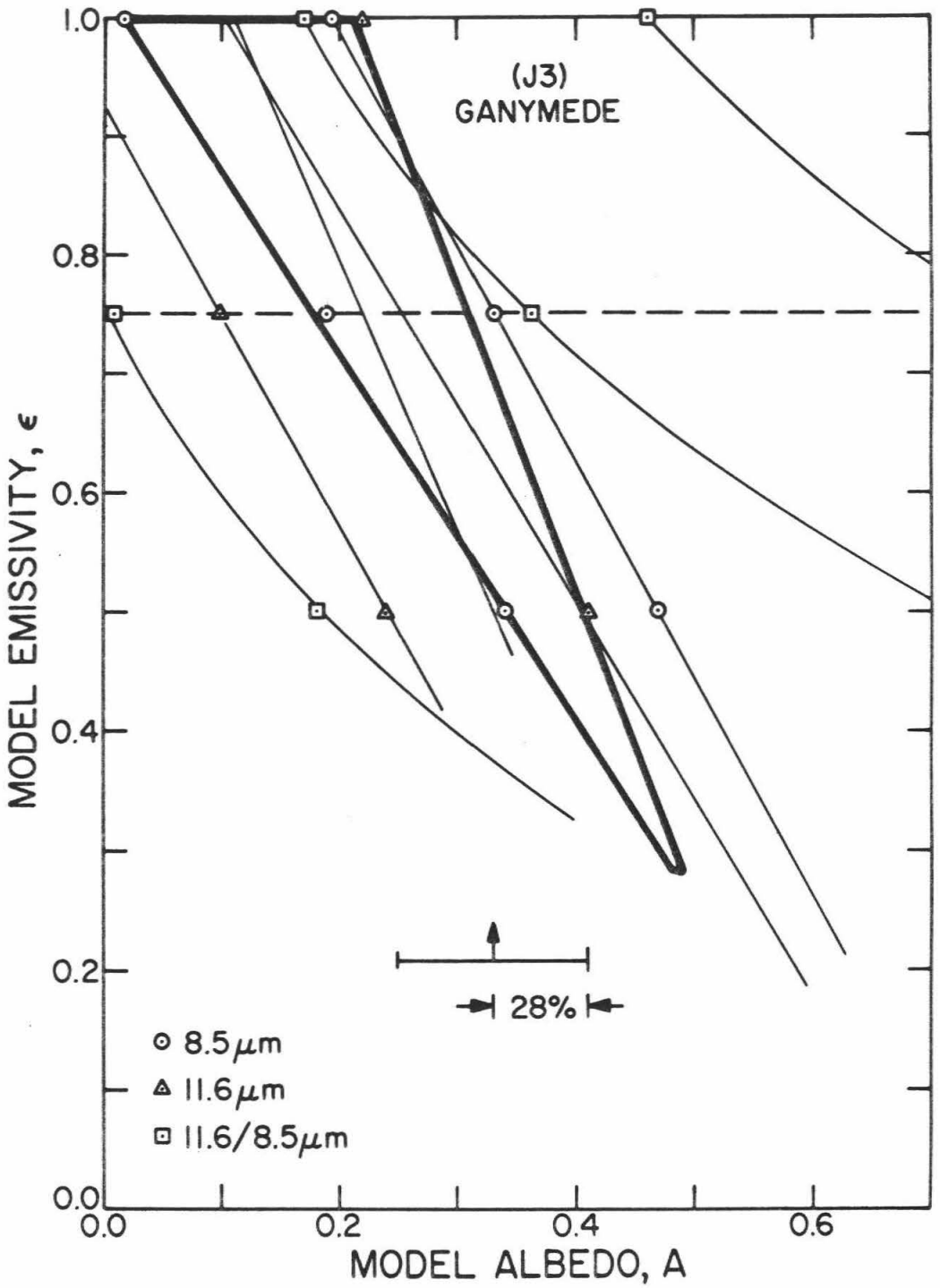
(J3)
GANYMEDE
MODEL EMISSIVITY, ε
MODEL ALBEDO, A
1.0
0.8
0.6
0.4
0.2
0.0
0.0
0.2
0.4
0.6
28%
8.5μm
11.6μm
11.6/8.5μm

The lunar model was also run for (J4) Callisto using a variety of A and ε values with a 2,380 km radius. The error in the photometric predictions due to the uncertainty in the radius is likely to be about 20 percent. The comparison between the model and the observations is made in Fig. 24. In Fig. 24a the 11.6 μm observations are a bit high compared to the model when $\varepsilon = 1.0$. The observations of Gillett et al (1970) give a slightly lower $E \cdot \Delta^2$ at 11.0 μm ($(14.5 \pm 2.3) \times 10^{-15}$ W cm^{-2} μm^{-1}) but it is within the present error bars. There is no problem at 10.5 μm and the error bars at 8.5 μm (not shown) are so large that the observations are not very diagnostic. This is also true for the observed ratio of 11.6 μm/8.5 μm.

If the present observations near $\theta = 260°$ are considered and the 11.6 μm $E \cdot \Delta^2$ values lie between 16 and 20×10^{-15} W cm^{-2} μm^{-1} then no reasonable model solution exists. Even when $\varepsilon \neq 1.0$ is allowed, there is no reasonable region (i.e., one with $\varepsilon \geq 0.5$) in the A-ε plane which satisfies both the present 11.6 μm and 10.5 μm data.

For J4 only a 10 percent increase in the predicted $E \cdot \Delta^2$ can be realized if the larger disk-diameter measurements ($\sim 1\overset{''}{.}32$ compared to $1\overset{''}{.}26$ adopted in this thesis) are used. This helps, but it is not enough to resolve the difficulty.

Letting ε be a function of wavelength enables one to construct a model that generates the observed 11.6 μm irradiance data. As merely a demonstration, suppose that the emissivity at 11.6 μm is unity and consider a solution for a variety of possible values for A and ε. This is done for $\varepsilon = 0.75$ and 0.5 and auxillary curves are generated and plotted as thin solid lines in Fig. 24a.

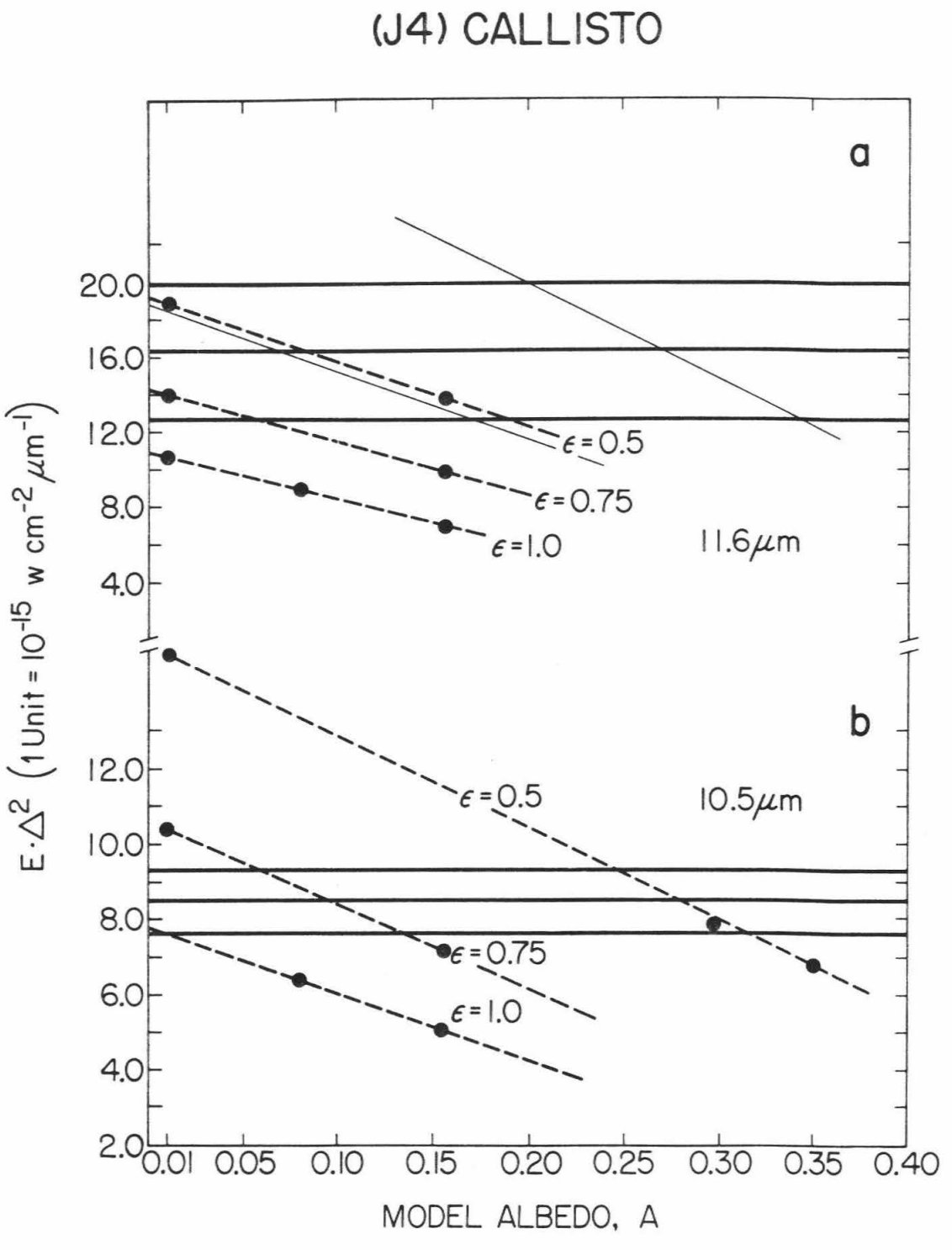

Fig. 24. Model predictions versus observations for (J4) Callisto

Taking the upper two horizontal lines as the observational limits for the 11.6 μm data (from $\theta \sim 260°$) and the auxillary curves, one can find a region in the A-ϵ plane that is compatible with the observations for all bandpasses: $A \sim 0.15$ and $\epsilon \sim 0.6 - 0.7$ with unspecified error bars. By way of comparison, Johnson (1970, 1971) using the lunar phase integral finds A(0.56 μm) = 0.156 which corresponds to a bolometric Bond albedo of A = 0.145.

In conclusion, the lunar model has failed for J4. However, the high irradiance values that have been measured are not physically impossible to attain. Considering the scatter in the present observations and in the data reported by other observers, it is not entirely obvious whether the difficulty is with the measurements or with (J4) Callisto itself.

(4) Vesta

In the following, the observed and the model phase effects are compared. The model is used to remove the phase effect from Vesta's lightcurve (Fig. 3). Using Barnard's diameter for Vesta as a starting point, the model is then used to predict values for $E \cdot \Delta^2$. The predictions are found to be much too low. The phase integral for the Moon, $q = 0.585$, is assumed to apply and the radius of Vesta can now be computed given the Bond albedo. Using this method the model correctly predicts the infrared observations if the bolometric Bond albedo of Vesta is about ten percent. The modelling here differs from that of Allen (1970, 1971), in that the emissivity is not assumed and several models are considered. One of these accounts for rotation and heat flow into the surface. Finally, several alternatives for modelling are discussed and are shown not to apply.

The model developed in Section III is now used to investigate the relative phase effect for (4) Vesta. The shape of the model beam patterns is fairly insensitive to choice of albedo and wavelength and is not dependent upon the asteroid's size. The lunar model was run for (4) Vesta using $A = 0.2$ and the 10 μm phase effect was computed. The results are shown as solid curves in Fig. 25. The observational data in this figure are identical to that of Fig. 6 and the model curves have been translated vertically by eye until they fit the observations.

The agreement between the model and the observations is excellent at 8.5 μm. Unfortunately, Allen's (1970) data appear to have an undue amount of scatter. At 11.6 μm the situation is reversed and the present data seem to have

Fig. 25

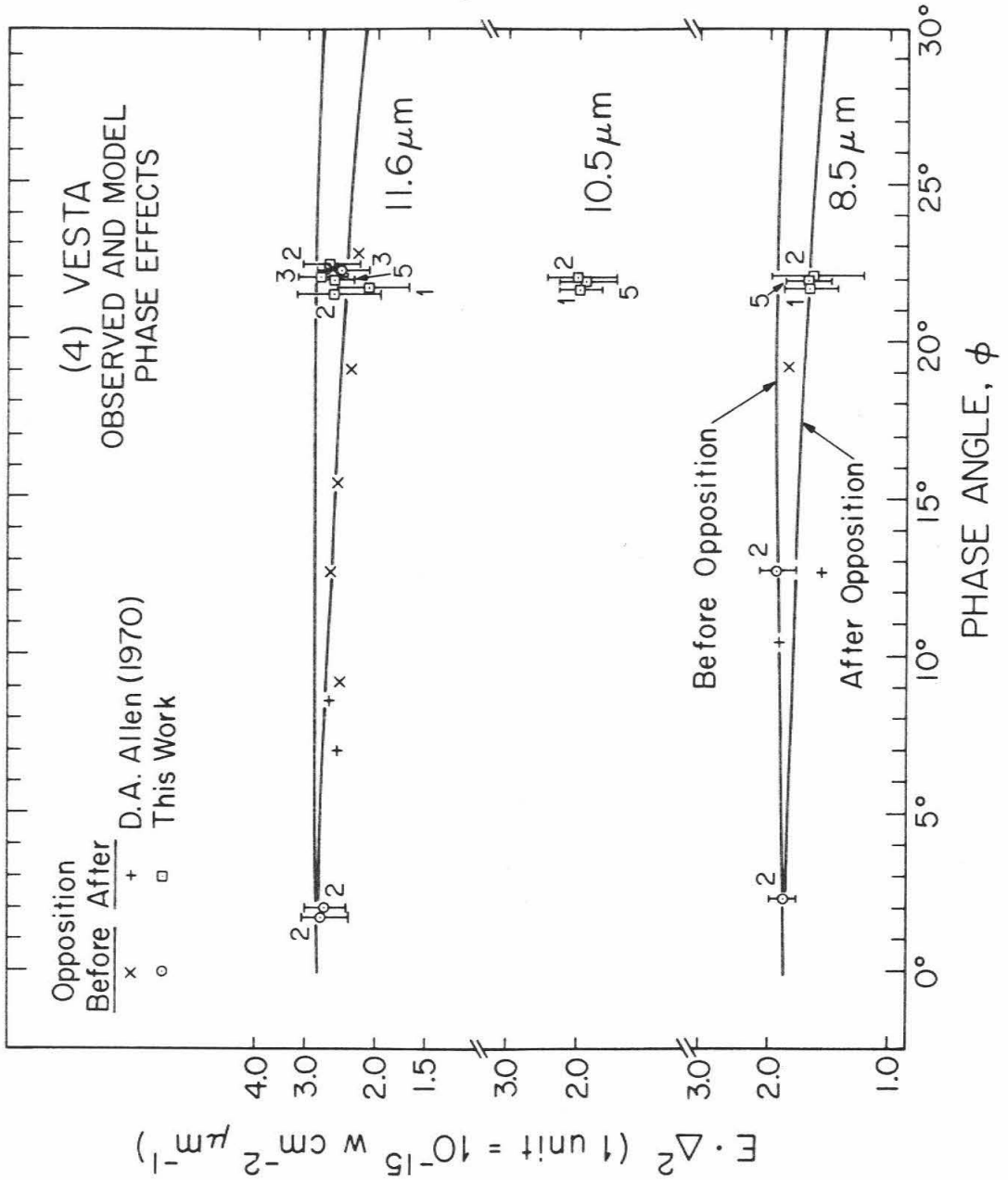
(4) VESTA
OBSERVED AND MODEL
PHASE EFFECTS
Opposition
Before After
D.A. Allen (1970)
This Work
11.6μm
10.5μm
8.5μm
Before Opposition
After Opposition
PHASE ANGLE, φ
0°
5°
10°
15°
20°
25°
30°
4.0
3.0
2.0
1.5
1.0

the larger scatter. It is interesting that the trend of the 11.6 μm data seems to be the reverse of what is expected. The data before opposition fit the after-opposition branch of the phase function better, and vice versa. There is little chance that the direction of rotation for (4) Vesta could have been mistaken. The above effects are attributed to scatter. This can be verified by inspection of the reproducibility of the observations at a given phase angle. It is noted that the correct branch of the model phase function is within the error bars for each night's data.

It is concluded that within the limits of observational error, the model has the correct angular distribution for the emitted infrared radiation.

The model was also run for two non-lunar cases to test the sensitivity of the phase effect. First, an iron ball ($\rho = 8$ g cm^{-3}, $C = 0.06$ cal g^{-1} °C^{-1}, $\gamma = 0.2$, $\epsilon = 0.5$) was tried and second, a sphere of solid rock ($\rho = 2.5$ g cm^{-3}, $C = 1.0$ cal g^{-1} °C^{-1}, $\gamma = 0.05$, $\epsilon = 1.0$). The iron case produced practically no effect and the case for rock predicted the after-opposition effect at phase $\varphi = 25°$ to be 97 percent of the value at opposition. The best data ($\lambda = 8.5$ μm) suggest that the observed phase effect is greater. The two above non-lunar models are rejected. Note that this conclusion is tentative because it rests on only the four 8.5 μm observations made before and the eight made after opposition.

With the model phase function now derived, the lightcurve data for (4) Vesta can be corrected to remove the nominal phase effect. The result is

Fig. 26. The dashed lines are the corresponding visible lightcurve, and as before, they have been fit to the infrared data by eye. At 8.5 μm the fit is excellent. The 11.6 μm data here show the scatter which was previously suspected. To within the limits of observational precision, the infrared lightcurve cannot be said to differ either in shape or phase from the visible lightcurve. This is consistent with (4) Vesta having a rather uniform albedo.

From the corrected lightcurves it appears that the error bars for 8.5 μm and perhaps 10.5 μm may have been chosen too conservatively. At 11.6 μm the choice appears to be better with the ratio for the bars that fully include the curve being 3:1.

The lunar model is now run for various combinations of albedo and effective emissivity. Barnard's radius of 190 km is used as the nominal starting value for the model. The observed and the predicted values of $E \cdot \Delta^2$ are plotted in Fig. 27. The heavy horizontal lines represent the data and they are, from the center out, the mean, the mean plus and minus the standard deviation of the mean and the mean plus and minus the standard deviation. The results of individual model runs are designated by filled circles and the curves are graphical interpolations.

The 11.6 μm/8.5 μm ratio is important because it is independent of the asteroid's size and of any multiplicative systematic errors in the absolute calibration of the photometry. But, the ratio is sensitive to systematic errors between the two bandpasses and this error is assumed to be 10 percent in Part 1 of this thesis. Inasmuch as the infrared lightcurve coverage for (4) Vesta is good, the

Fig. 26

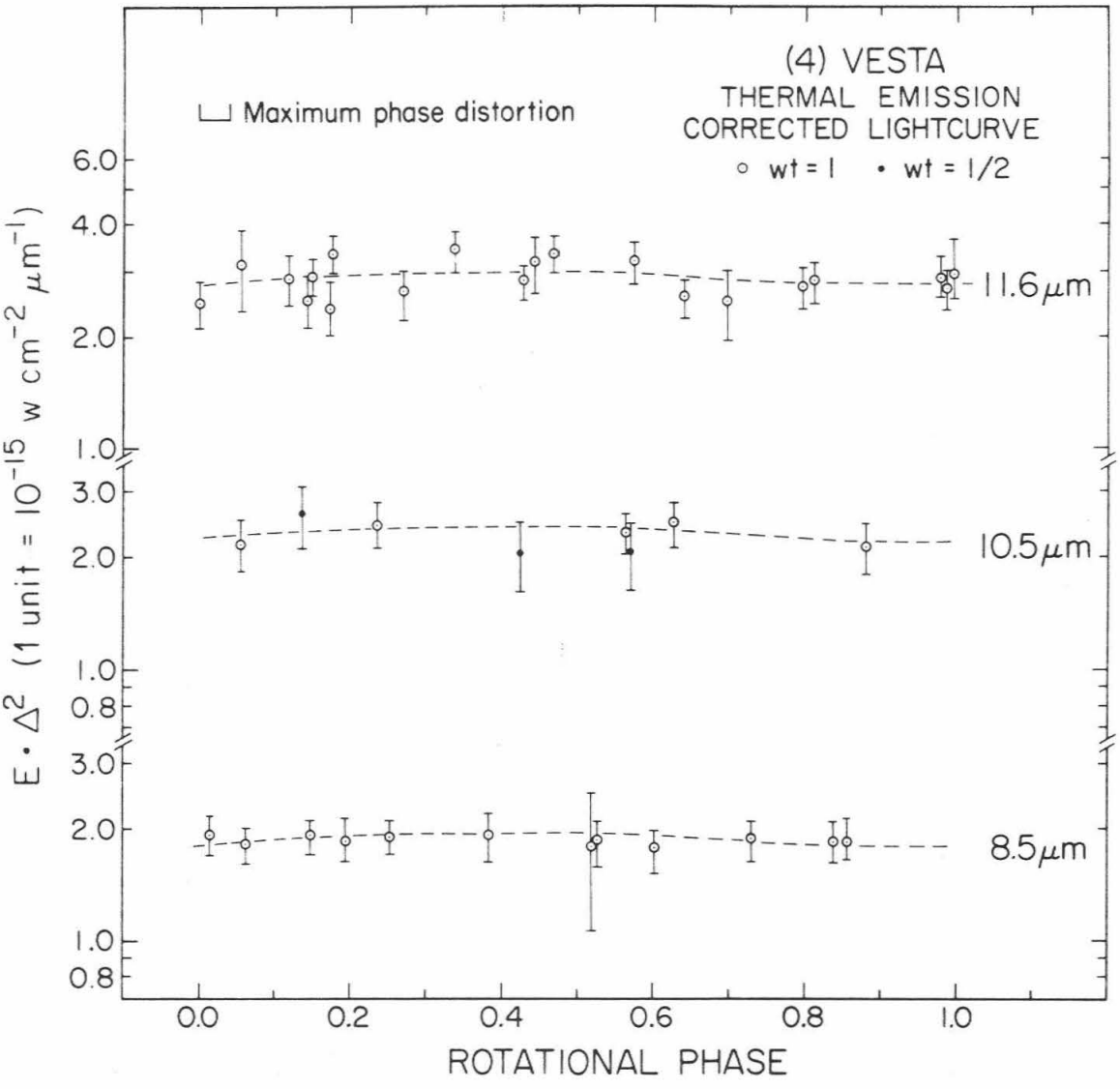
(4) VESTA
THERMAL EMISSION
CORRECTED LIGHTCURVE
○ wt = 1 • wt = 1/2
Maximum phase distortion
11.6μm
10.5μm
8.5μm
E • Δ² (1 unit = 10⁻¹⁵ w cm⁻² μm⁻¹)
6.0
4.0
2.0
1.0
3.0
2.0
1.0
0.8
3.0
2.0
1.0
0.8
0.0
0.2
0.4
0.6
0.8
1.0
ROTATIONAL PHASE

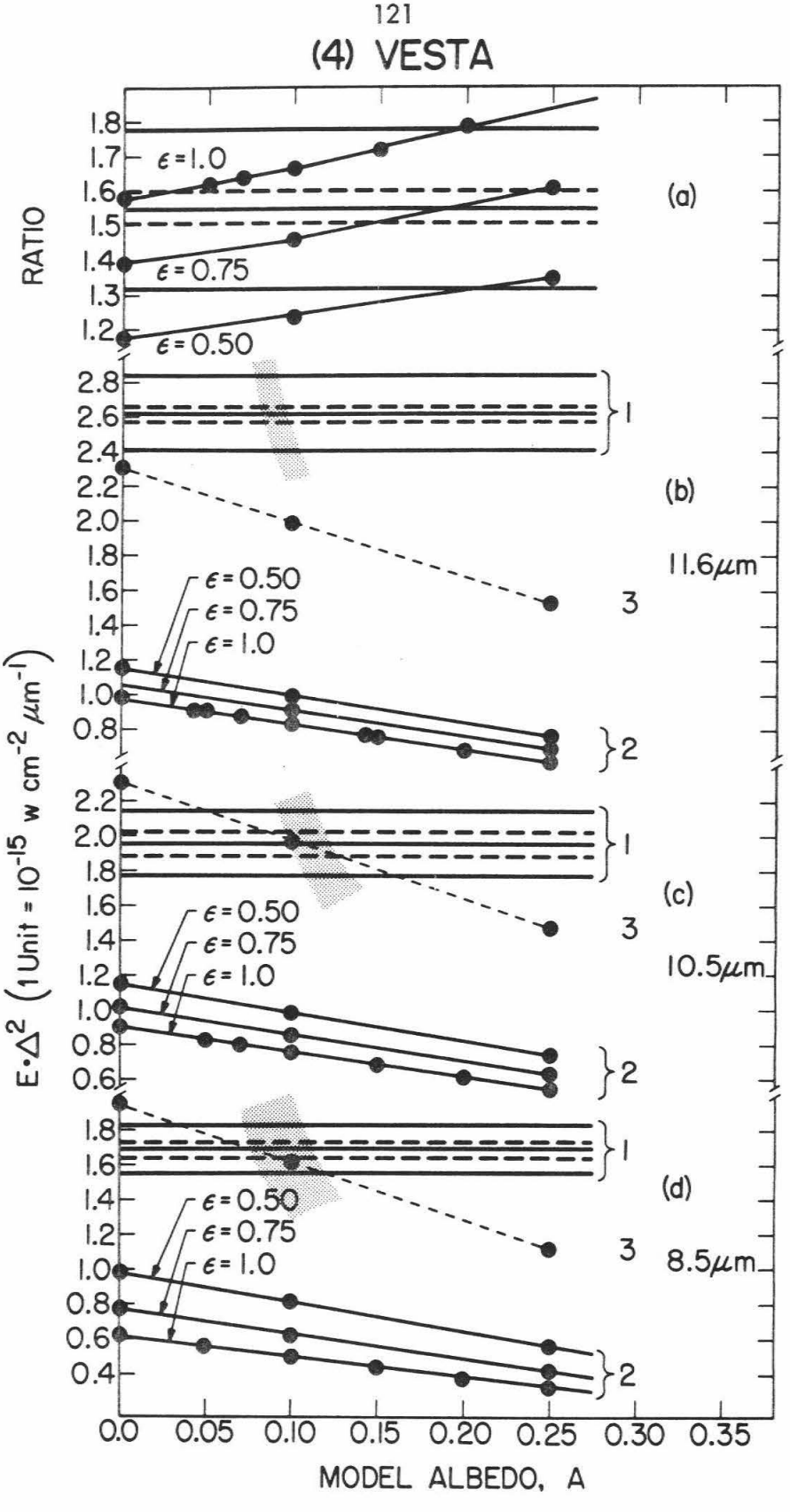

Fig. 27. (4) Vesta observed and predicted values of $E \cdot \Delta^2$

observational random errors are estimated by the standard deviation of the mean.

The observed 11.6 μm/8.5 μm ratio (Fig. 27a) admits the possibility of many different combinations of A and ε. These values are now transferred to the A-ε plane by the same method used for (J3) Ganymede. In Fig. 28 the curves are, from the center out, the ratio, the error in the ratio and the assumed 10 percent systematic error. If a +10% error is allowed for the ratio, then A must be less than 0.2 for $\varepsilon = 1.0$. For $\varepsilon = 0.75$ the model albedo is between 0.04 and 0.4, and so forth.

From the plots for $E \cdot \Delta^2$ (Fig. 27b, c, d), it is obvious that Barnard's radius is too small. The discrepancy at 11.6 μm between the observations and the predictions is greater than a factor of 2. Such an error is too large to attribute to the absolute calibration of the stellar photometry which was estimated at 20 percent in Part 1 of this thesis. Even if the emissivity varies as a free parameter in the model, the observed irradiances cannot be matched. In order to obtain a better radius, the absolute magnitude, B(1,0), must be used. The visible wavelength photometry specifies a relationship between the Bond albedo and the size if the value of the phase integral, q, is known. This essentially requires an assumption about the shape of the beam pattern (phase function) for the reflected light. The available phase data have been shown in Fig. 19 and show Vesta to be similar to the Moon. Therefore, Harris' (1961) lunar phase integral of $q = 0.585$ is assumed.

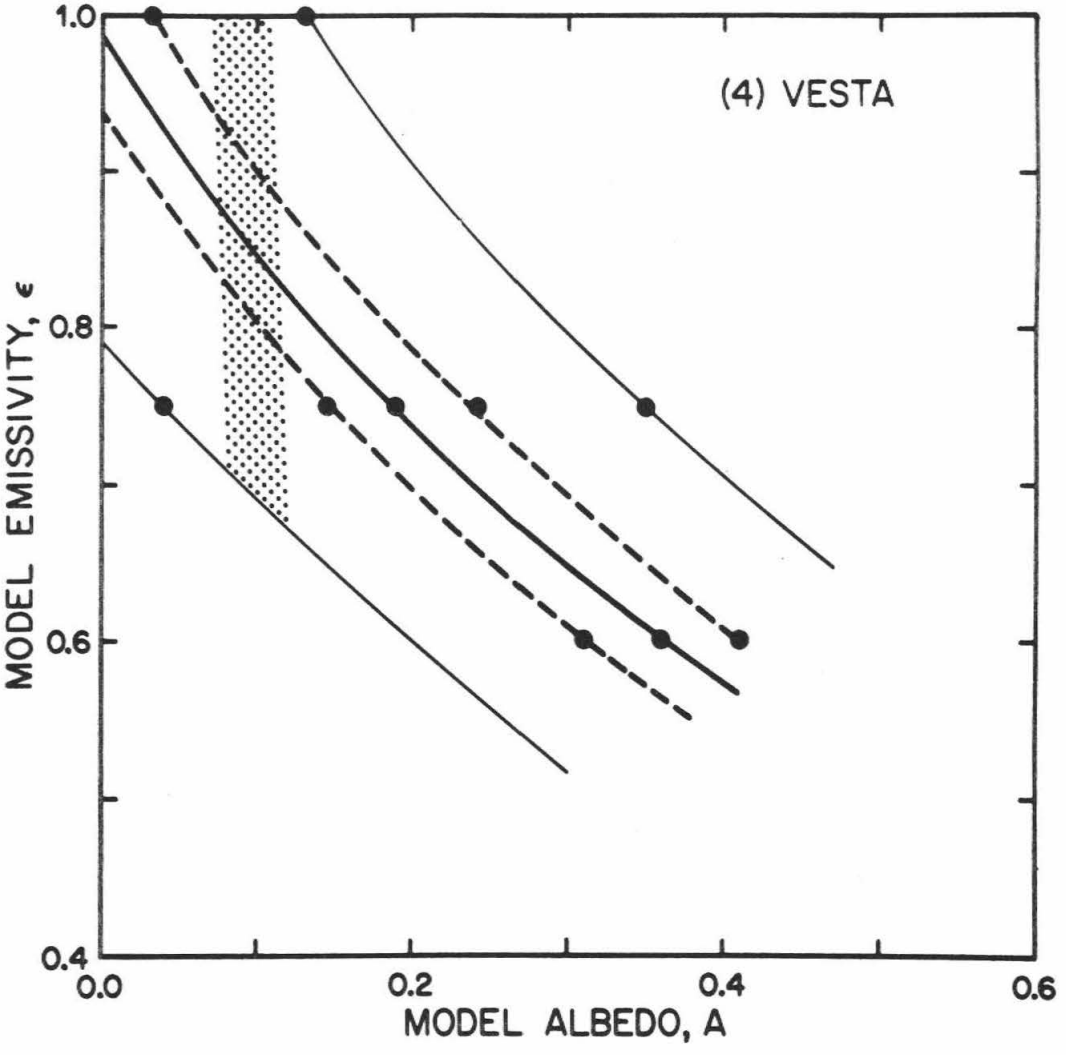

Fig. 28. (4) Vesta in the A-ε plane

Let p be the geometric albedo, and q the phase integral for the model:

$$p = \frac{A}{q} \quad . \tag{8}$$

For the B filter the geometric albedo is, by definition:

$$p = \frac{(E_B \cdot \Delta^2) \times (1.49 \times 10^{13} \text{ cm AU}^{-1})^2}{R^2 \; \frac{E_{B_\odot}}{r^2}} \tag{9}$$

Equation 9 can be expressed as:

$$p = \frac{10^{\frac{B(1,0)}{-2.5}} \; (1.49 \times 10^{13} \text{ cm AU}^{-1})^2}{R^2 \; E_{B_\odot}} \tag{10}$$

where E_B is the asteroid's B irradiance above the Earth's atmosphere, $E_{B_\odot}$ is the solar B irradiance at 1 AU from the Sun. B(1,0) is the asteroid's absolute magnitude, R the model radius (in cm) and Δ and r are the distances from the asteroid to the Earth and to the Sun in AU. Thus, from Eqns. (8) and (10):

$$R^2 = \frac{q}{0.94A} \quad \frac{10^{\frac{B(1,0)}{-2.5}}}{E_{B_\odot}} \; (1.49 \times 10^{13} \text{ cm AU}^{-1})^2 \tag{11}$$

The factor of 0.94 has been introduced to convert the bolometric to the B-bandpass Bond albedo. This conversion factor was derived using the color of (4) Vesta (McCord et al 1970) and the spectral irradiance of the Sun (Labs and Neckel 1968).

When Eqn. 11 is used to calculate the model radius for each trial albedo, the predictions of $E \cdot \Delta^2$ increase sharply as the albedo is diminished. The predicted $E \cdot \Delta^2$ values now intersect the horizontal lines that represent the observations. The new predictions are shown as stippled zones in Fig. 27b, c, and d.

In the A-ϵ plane there is no region that is common to all three infrared bandpasses. Such a possibility is created since the problem is over determined with only one bandpass being necessary for a solution. In Fig. 28 the envelope of the outer standard deviations for all three solutions is plotted as a stippled zone. This zone is truncated near $\epsilon = 0.7$ by the 11.6 μm/8.5 μm ratio (on the assumption of a -10% systematic error). If the ratio is correct as it stands then $0.9 \geqslant \epsilon \geqslant 0.8$.

From Fig. 28 it is concluded that the infrared observations are consistent with any value of effective emissivity that is greater than 0.7. Upon taking the extrema of the stippled zone ($A = 0.124$, $\epsilon = 0.7$, $\lambda = 10.5$ μm and $A = 0.073$, $\epsilon = 1.0$, $\lambda = 8.5$ μm) as the range of the error bars, the model albedo is 0.099 ± 0.026. From Eqn. 11 the corresponding model radius is then 300^{+50}_{-30} km.

The fact that the value of the model albedo is rather insensitive to variation of the emissivity and to errors in the infrared photometry is illustrated by Figs. 27 and 28. For example, a 20 percent error in the 10.5 μm $E \cdot \Delta^2$ observations would shift the model albedo by about ± 0.026 and thus the radius by about $\pm 10\%$. If q errs by $\pm 20\%$, then the radius would also change by $\pm 10\%$.

Surface roughness is an effect which will increase the amount of observed infrared radiation. In regions on Vesta's surface where the Sun appears at a low elevation angle, fragments of rock that rise above the mean surface level or otherwise receive sunlight at angles closer to normal incidence than the "average" surface element will be heated to higher temperatures. This causes the emission beam pattern (phase effect) to have a higher value in the direction of the Sun than would a smooth surface. A fairly good approximation which accounts for the roughness on the Moon is to take the local temperature to be the temperature of the subsolar point multiplied by the sixth root of the cosine of the angle between the local surface normal and the direction to the Sun.

In Table 4 the results from the "rough", non-rotating spherical model are tabulated. This model is an important limiting case because Vesta rotates rapidly ($\sim 5^h$) and does not return as much radiation in the direction of the Sun. It can be seen from Table 4 that, at best, the effect of roughness is not large enough.

These model results are in excellent agreement with the calculations of D.A. Allen (1970) who found a Bond albedo of 0.119 and an infrared radius of 287±3 km by using a smooth non-rotating spherical model. For the purpose of

TABLE 4. COMPARISON OF MODELS FOR (4) VESTA

	Description	Method of Handling Temperature, T, Distribution	Model Albedo	Model Radius
1.	Smooth, non-rotating sphere	$T = \left(\frac{(1-A)S}{\sigma}\right)^{1/4} \left(\cos \varphi\right)^{1/4}$	0.11	286 km
2.	"Rough", non-rotating sphere	$T = \left(\frac{(1-A)S}{\sigma}\right)^{1/4} \left(\cos \varphi\right)^{1/6}$	0.13	268 km
3.	Heat flow and lunar-type model (Section III)	Linear heat flow equation	0.10	300 km

S = solar constant at the asteroid; φ = angle between heliocentric radius vector and local surface normal; and σ = Stefan-Boltzmann constant.

comparison, this model is used to reduce the present data; the results are shown in Table 4.

The polarization work by Veverka (1970a, b) has yielded a preliminary normal reflectivity estimate of 0.25 ± 0.07 for Vesta. This implies a bolometric Bond albedo of about 0.146 ± 0.041 (for $q = 0.585$), which is in good agreement with the infrared data. However, the polarization method is both empirical and based upon data for materials other than those from the surface of Vesta. The estimate comes from an equation first given by KenKnight et al (1967) and noted independently and applied to asteroids by Widorn (1967):

$$h = c \cdot r_n^{-\beta} \qquad (12)$$

where h is the percent polarization per degree of phase angle and r_n is the normal reflectivity of the surface. c and β are empirical constants. Both the above authors and Veverka (1970b) feel that the value of $\beta = 0.8$ has been fairly well determined from laboratory measurements on lunar-like samples and from observations of the Moon. However, the constant, c, is not as certain and Veverka thinks that a likely range of values is 0.024 to 0.031. This range then determines the value for r_n. Veverka points out that the slope, h, can only be estimated because Vesta cannot be observed at phase angles greater than $\sim 26°$ and that the relationship, Eqn. 12, should be calibrated in the laboratory by measurements of crushed meteorites. In spite of these problems, the agreement between the polarization and the infrared methods is significant because the two methods have

no common assumptions, except for the value of the phase integral, q, which is used in order to compare the results.

The model diameters found here do not agree with disk measurements when the latter are taken at face value. A 600 km diameter at unit distance subtends an angle of about 0".8 or 0".3 larger than that measured by Barnard. The observed phase function for Vesta seems to rule out the possibility of limb darkening as the cause of the low measured diameters. This reasoning is based on analogy with the Moon which does not exhibit significant limb darkening. The systematic errors between the various disk-measurement methods have been estimated here to be 0".08. The random error for filar micrometers is estimated to be ±0".2 by Dollfus (1970, p.48). For the Vesta measurements made by Dollfus and his co-workers the random errors are presumably less, but their value of 0".62 is closer to the 0".8 implied by the infrared work. Considering the size of these errors it is probable that the infrared diameter is within 2 standard deviations of the disk measurements.

Could one construct a satisfactory model in which the disk diameter measurements are assumed to be correct? One attempt to do this lets the emissivity vary with wavelength in a way such that it is unity at 8-14 μm but elsewhere is such that the effective emissivity is low, say $\epsilon = 0.5$. This model, then, is essentially a test for absorption bands in the thermal emission spectrum which are situated at wavelengths other than 8-14 μm. The results of this model are labeled "3" in Fig. 27b, c, and d. While the approximate levels of irradiance can be

satisfied, the observed 11.6 μm/8.5 μm ratio is not. It would appear that this model requires A ~ 0.1. If this is the case, then the phase integral, q, must be ~ 0.2 (by Eqn. 11). From the available visible-wavelength phase coverage, Fig. 18, there is no reason to suspect that q differs in any significant way from the value for the Moon (q = 0.585).

Thus, a reasonable model has yet to be found which can satisfy both the disk measurements and the infrared photometry.

Using the slope of the 8.5 μm, $E \cdot \Delta^2$ predictions for a fixed radius, Fig. 27d (No. 2), one can return to the corrected lightcurve, Fig. 26, and set an upper limit upon the variation of the "integral" model albedo across Vesta's surface. Using the peak-to-peak variation of the 8.5 μm lightcurve, the range of the model albedo is A = 0.10 ± 0.06. This limit, of course, dos not apply to Vesta's north-polar region because the declination of the Earth as seen in Vesta-centric, equatorial coordinates, was about south thirty degrees during the 1969-1970 opposition.

In conclusion, both D.A. Allen (1970, 1971 private communication) and this author agree upon the measured irradiances for (4) Vesta and neither author has been able to reconcile them with the disk measurements.

The modelling situation is recapitulated with the aid of Table 5. Column A is the lunar-type model with about a 300 km radius. This model obviously conflicts with the disk measurements, but it explains all of the other observations. Columns B, C, and D show the results of attempts to construct

TABLE 5 . RECAPITULATION FOR (4) VESTA

	Observational Evidence	Data that do not fit (Models discussed in text): A	B	C	D
1.	Disk Measurements (~ 200 km radius)	X			
2.	Visible-wavelength Photometry				
3.	Visible-wavelength Colorimetry			X	X
4.	Visible-wavelength Phase Effect			?	?
5.	Visible-wavelength Polarization, Negative Branch				
6.	Visible-wavelength Polarization, Linear Slope		X	?	?
7.	Infrared, Thermal Emission, Photometry		X	X	
8.	Infrared, Thermal Emission, Colorimetry (11.6μm/8.5μm)		X	X	
9.	Infrared, Thermal Emission, Phase Effect				
10.	Physical Properties of Naturally-occurring Solid Materials			?	X

models based upon the assumption that the disk measurements are correct. In Column B, a 190-km lunar-type model is considered. It yields predictions that disagree with all of the infrared observations as well as with the albedo suggested by the slope of the linear portion of the polarization versus phase angle data. In an attempt to circumvent the difficulties encountered in Column B, the emissivity of the model is allowed to vary with wavelength in such a way that the effective emissivity is ~0.5, and $\varepsilon(\lambda) = 1.0$ for $8.5\ \mu m \leq \lambda \leq 14\ \mu m$. Although this variation allows the approximate observed levels of infrared irradiance to be reached, the match at 11.6 μm is not good enough to say that the model now agrees with the observations. Furthermore, a low value for the effective emissivity, (≤ 0.5) conflicts with the visible-wavelength colorimetry that is available for Vesta. According to McCord et al (1970), the colorimetry implies that the surface composition of Vesta closely resembles that of certain basaltic achondrites (e.g., Nuevo Laredo).

In Column D the emissivity is allowed to vary freely in the 8 - 14 μm region and all of the infrared data can be generated by the model if the effective emissivity is low (~ 0.2?). Low values of effective emissivity require a metallic surface and this model would severely violate the colorimetry by requiring that that technique be insensitive to the difference between a metallic composition and a basaltic achondrite. Furthermore, emissivities that are high at 8-14 μm and very low elsewhere are not compatible with any abundant, naturally-occurring, solid material.

For all of the models that have been considered, every attempt to reconcile the disk diameter measurements with other observations has failed. In order to obtain a self-consistent set of data, it appears that the disk diameter measurements for Vesta must be rejected. The observations that remain are then compatible with a lunar-type model.

(7) Iris and (324) Bamberga

A careful comparison of (7) Iris and (324) Bamberga is important because the color diagrams (Figs. 12-14) have already identified these two asteroids as having different surface properties. Both minor planets have been well observed (Table 1) and their infrared signals are nearly equal in amplitude. For both asteroids the positions of the axial rotation vectors are assumed to be unknown. Positions have been published for the axis of rotation for Iris (Cailliatte 1956, Gehrels and Owings 1962) but the two values disagree, and furthermore, the methods of analysis could be invalid (Vesely 1971).

For an asteroid at opposition the Earth-based observer sees two limiting cases: (1) an equatorial view and (2) a polar view. The first case is studied by running the lunar-type model (Section III) for a variety of A and ε values with model radii computed via Eqn. 11. The second case is studied by calculations for $\varepsilon = 1.0$ only; this situation corresponds to the non-rotating spherical model. For Iris the rotation period is 7.125 hours but for Bamberga it is unknown. A fragment of an existing lightcurve suggests a period compatible with about 8 hours which is the value tabulated by Gehrels (1970).

The $E \cdot \Delta^2$ observations for Iris and Bamberga are compared with the model predictions for the two limiting cases in Figs. 29 and 30. The variation due to the uncertainty in the axial rotation vector is the more important source of modelling error. The effect of the lower values of emissivity have their greatest significance at 8.5 μm. For Iris and Bamberga, at $\sim$ 1.9 AU from the

Figs. 29 and 30. Comparison of the observations with model predictions. The heavy horizontal lines show the mean value and the mean plus and minus one standard deviation. The solid curves are the predictions for the equatorial-view case and the dashed curve shows the polar-view case.

Fig. 29

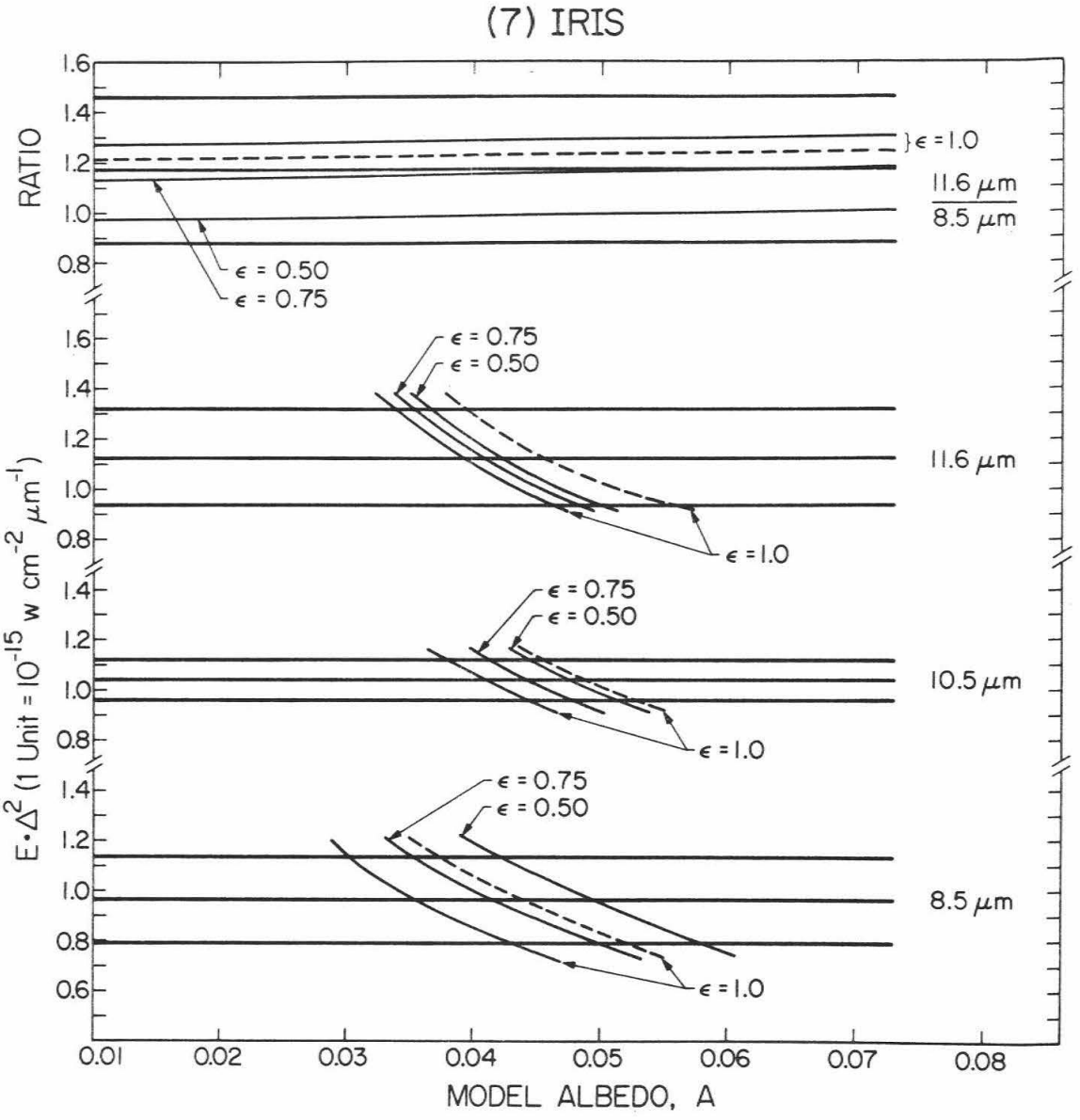
(7) IRIS
RATIO
E·Δ² (1 Unit = 10⁻¹⁵ w cm⁻² μm⁻¹)
MODEL ALBEDO, A
ε = 1.0
11.6 μm / 8.5 μm
ε = 0.50
ε = 0.75
11.6 μm
10.5 μm
8.5 μm

Fig. 30

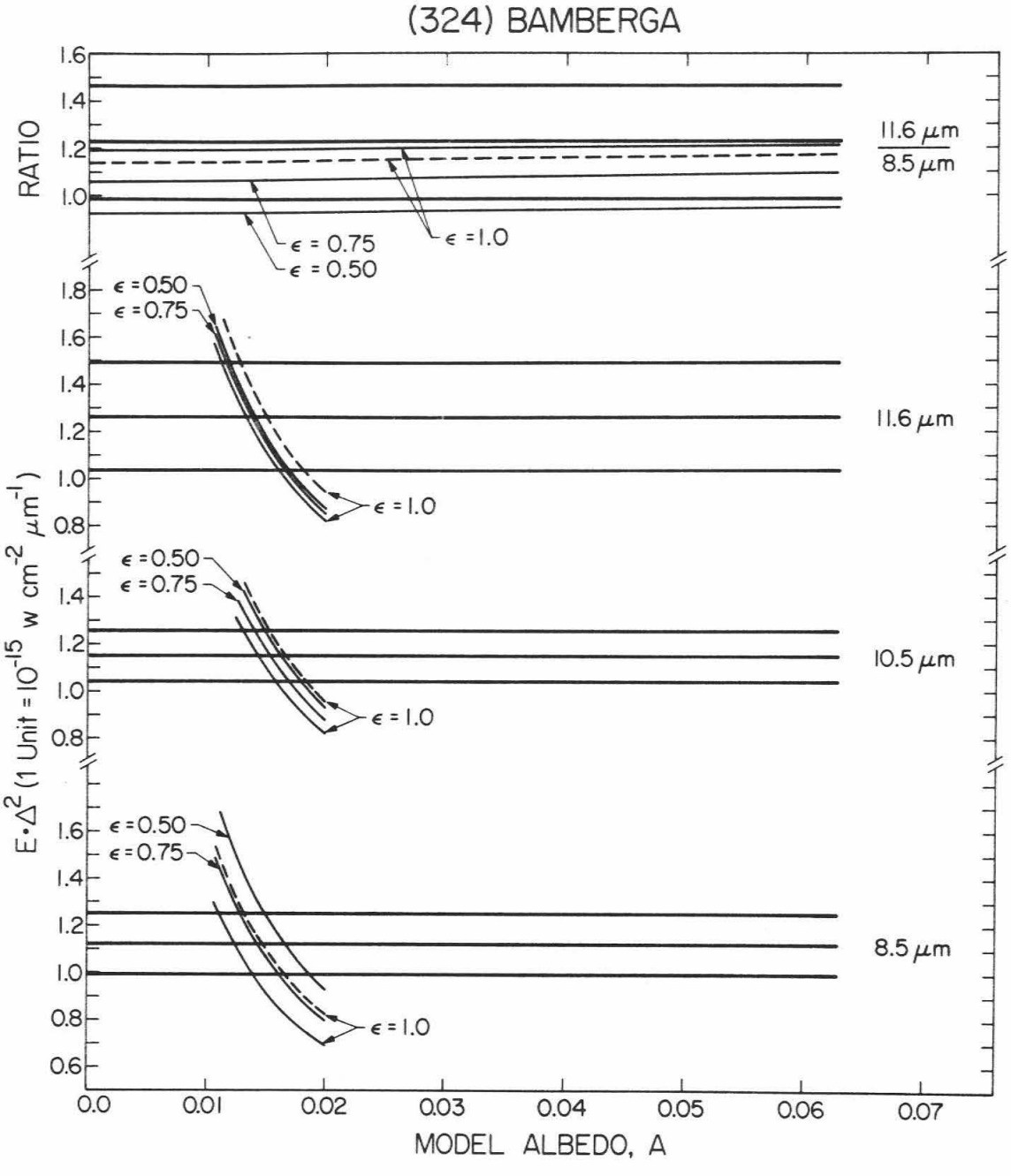
(324) BAMBERGA
RATIO
11.6 μm / 8.5 μm
ε = 0.75
ε = 0.50
ε = 1.0
ε = 0.50
ε = 0.75
11.6 μm
ε = 1.0
ε = 0.50
ε = 0.75
10.5 μm
ε = 1.0
ε = 0.50
ε = 0.75
8.5 μm
ε = 1.0
E·Δ² (1 Unit = 10⁻¹⁵ w cm⁻² μm⁻¹)
MODEL ALBEDO, A
0.0
0.01
0.02
0.03
0.04
0.05
0.06
0.07

Sun, the 11.6 μm/8.5 μm ratio is not strongly dependent upon the albedo. Theoretically, the hiatus between the two limiting cases is not large enough to destroy the utility of this ratio, and if the present observations had a higher precision, useful limits could be set for the emissivities. Table 6 tabulates the results obtained when the various models are applied to the present data for Iris and Bamberga.

The error study for Iris and Bamberga shows that the conclusion of low albedo is not critically dependent upon either the model or the uncertainties in the photometry. The two families of curves in Figs. 31 and 32 represent the values of the model parameters that yield the observed visible and infrared irradiances. At their intersection, the values of A and R satisfy all of the available photometry. The curves for the visible are the constraints set by the absolute magnitude, B(1,0), when the visible phase integral, q, is given. The value of q is not known for either Iris or Bamberga and the lunar value ($q = 0.585$) is assumed. There is no a priori reason to suspect that the true value will differ much (more than ~10%) from this value. The curve is also shown for the admittedly extreme values of $q = 0.3$ and 0.9 in order to test the sensitivity of the conclusion to this particular assumption.

The infrared curves are the constraints that correspond to the three models: (a) "rough" non-rotating sphere, (b) smooth, non-rotating sphere or polar view, and (c) the rotating, lunar-type model or equatorial view.

Table 6. Comparison of Models for (7) Iris and (324) Bamberga

	Description	(7) Iris Model Albedo	(7) Iris Model Radius	(324) Bamberga Model Albedo	(324) Bamberga Model Radius
1.	Equatorial view: Heat flow and lunar-type model (Section III)	0.039	152 km	0.013	143 km
2.	Polar view: Smooth, non-rotating sphere	0.046	139 km	0.016	132 km
3.	"Rough", non-rotating sphere	0.053	129 km	0.018	122 km

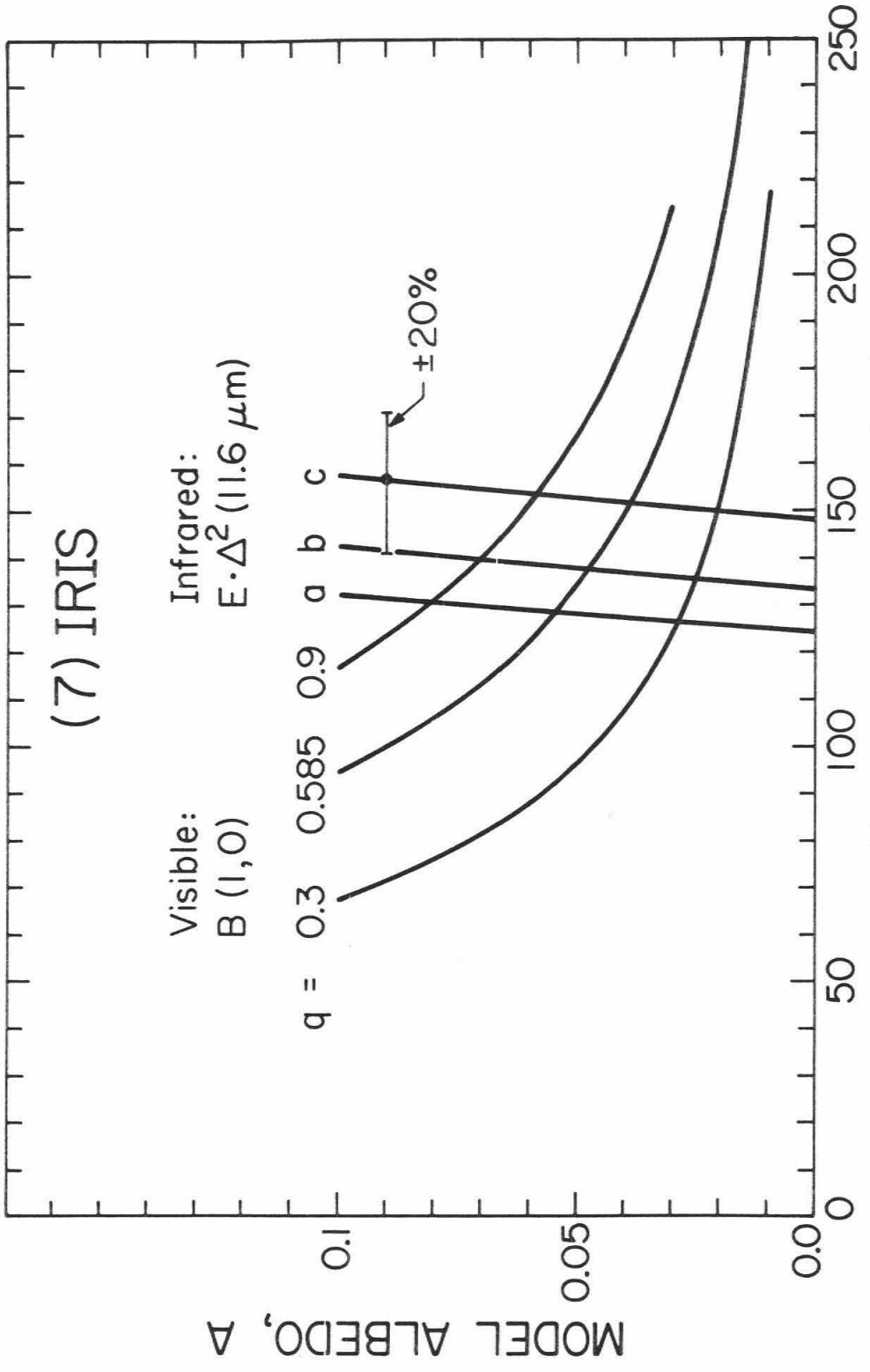

Fig. 31. (7) Iris: Model albedo vs model radius

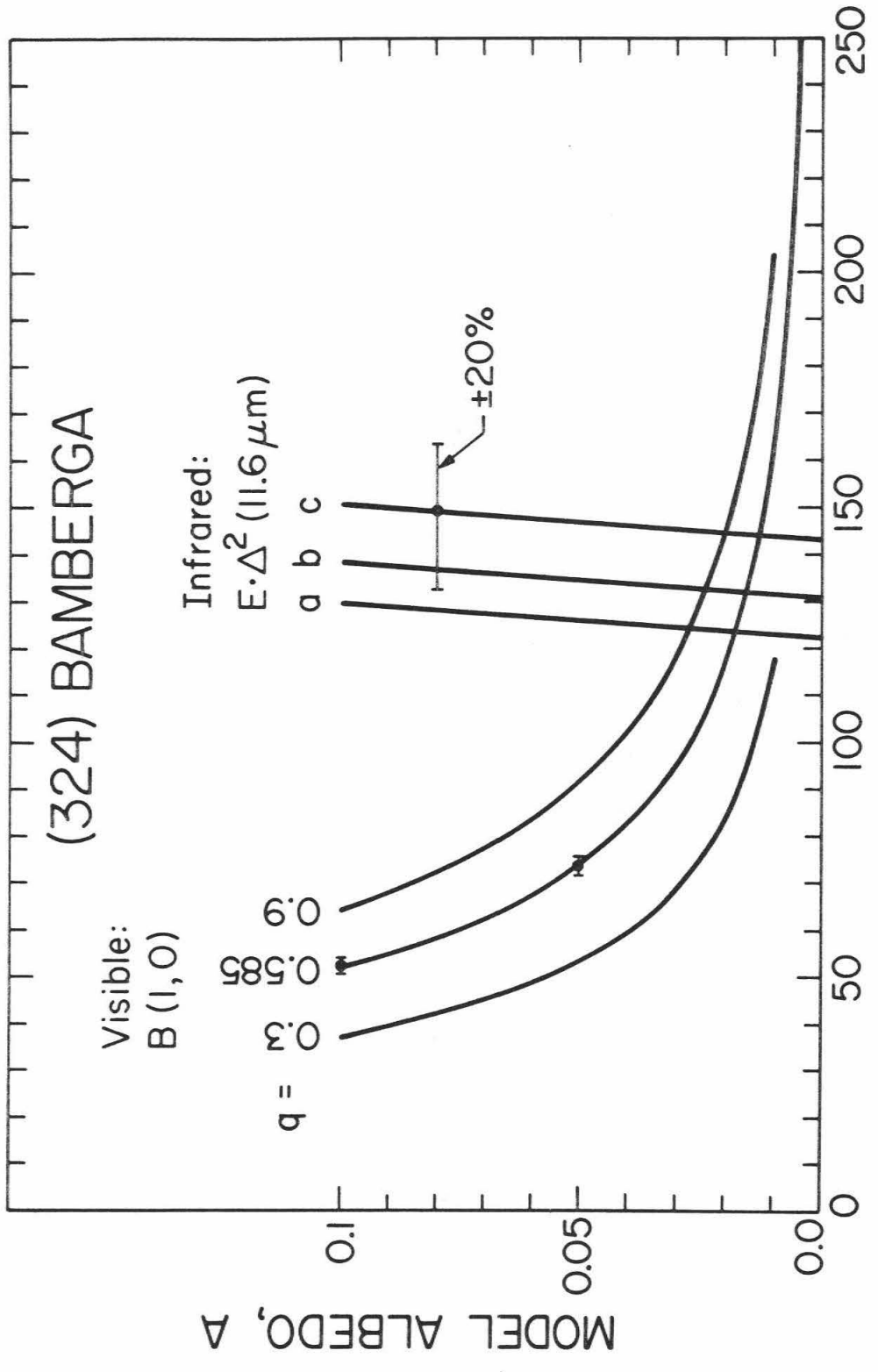

Fig. 32. (324) Bamberga: Model albedo vs model radius

The result shows that for dark objects ($A \sim 0.02$), the phase integral gives a model albedo uncertainty of less than ± 0.01. For Iris and Bamberga, the effect of the formal error in $B(1,0)$ is small and the error bars are plotted for two points on the $q = 0.585$ curve for Bamberga. A single set of error bars is plotted for the infrared curves corresponding to a $\pm$ 20 percent error in irradiance. The other infrared bandpasses define similar curves, all of which are within this error bar.

This analysis secures the conclusion that Bamberga must have an extremely low bolometric Bond albedo. Even a fortuitous combination of observational and likely modelling errors can not raise the model albedo to a value as high as $A = 0.03$. It also follows from Figs. 31 and 32 that the possibility that Bamberga and Iris could have equal albedos is not admissible, even with a doubly fortuitous combination of errors.

Other Asteroids

For the remaining asteroids that were observed, the positions of the rotation poles are not known and, for some of the objects, even the rotation rates have yet to be determined. By and large, the available lightcurve coverage is scant. Consequently some of these objects could have large errors ($\sim$ 20-40%) in B(1,0). The errors in the infrared photometry is also large as some of the error bars will show.

In the analysis for these asteroids the infrared phase effect is ignored, B(1,0) is used directly, and the emissivity of their surfaces is assumed to be unity. The visible-wavelength phase integral, q, is assumed to be 0.585. The color of Vesta is also assumed and thus the Bond albedo for the B bandpass is 0.94 of the bolometric Bond albedo. The emission beam pattern (phase effect) for each elemental area is assumed to be Lambertian.

The data are now processed using the rough spherical model. The model albedo and model radius are then normalized to the value for Vesta (A = 0.099, R = 300 km) in order to make a first order correction for the effects of rotation. It is reasonable to do this because all the rotation periods measured for asteroids fall in the range between 2.87 and 16.81 hours. From experience with (4) Vesta, (7) Iris and (324) Bamberga, one does not expect the modelling errors to be too large (Tables 4 and 6). Thus for A $\sim$ 0.1, one expects $\pm$0.03 to be a reasonable estimate on the model albedo errors. For A $\sim$ 0.02, the corresponding number is about $\pm$0.01.

The model parameters for asteroids are plotted in Figs. 33 and 34. The boxes in these figures represent the formal standard deviations of the infrared photometry and the errors assigned to B(1,0). The most significant feature on these plots is the position of (324) Bamberga and (19) Fortuna with respect to the other asteroids. Bamberga has been observed 15 times whereas Fortuna has been observed only twice, once at 8.5 μm and once at 11.6 μm (Table 1). Even though the results from the two bandpasses agree, it is felt that the observations are too few and that this asteroid should be reobserved before it can be confidentially classed with (324) Bamberga.

In Fig. 34, the parameters corresponding to each of the infrared bandpasses are plotted. The agreement from one wavelength to the next is excellent except for (1) Ceres. In the region where the model albedo is about 0.05, there are a number of objects: (6) Hebe, (7) Iris, (80) Sappho, and perhaps, (68) Leto. A number of other objects cluster in the 50 to 90 km and 0.03 to 0.1 albedo region. The errors for both the infrared and the visible photometry of these objects are large, as the error bars show. However, the data do suggest that there are smaller objects with albedos as high as that of (4) Vesta. (20) Massalia is the member of this cluster with the smallest error box, but this is based upon only one observation. The data for (2) Pallas, (5) Astraea, (15) Eunomia, (27) Euterpe, (39) Laetitia, (44) Nysa and (674) Rachele are poor and these asteroids must be observed again in order to reduce the size of the error boxes.

Figs. 33 and 34. Model albedo versus model radius. These model parameters are estimates of the bolometric Bond albedo and the radius or the "equivalent radius" in the case of an irregularly shaped asteroid. For comparison, the 11.6 μm data for (4) Vesta have been reduced by the methods of this section and plotted.

Fig. 33

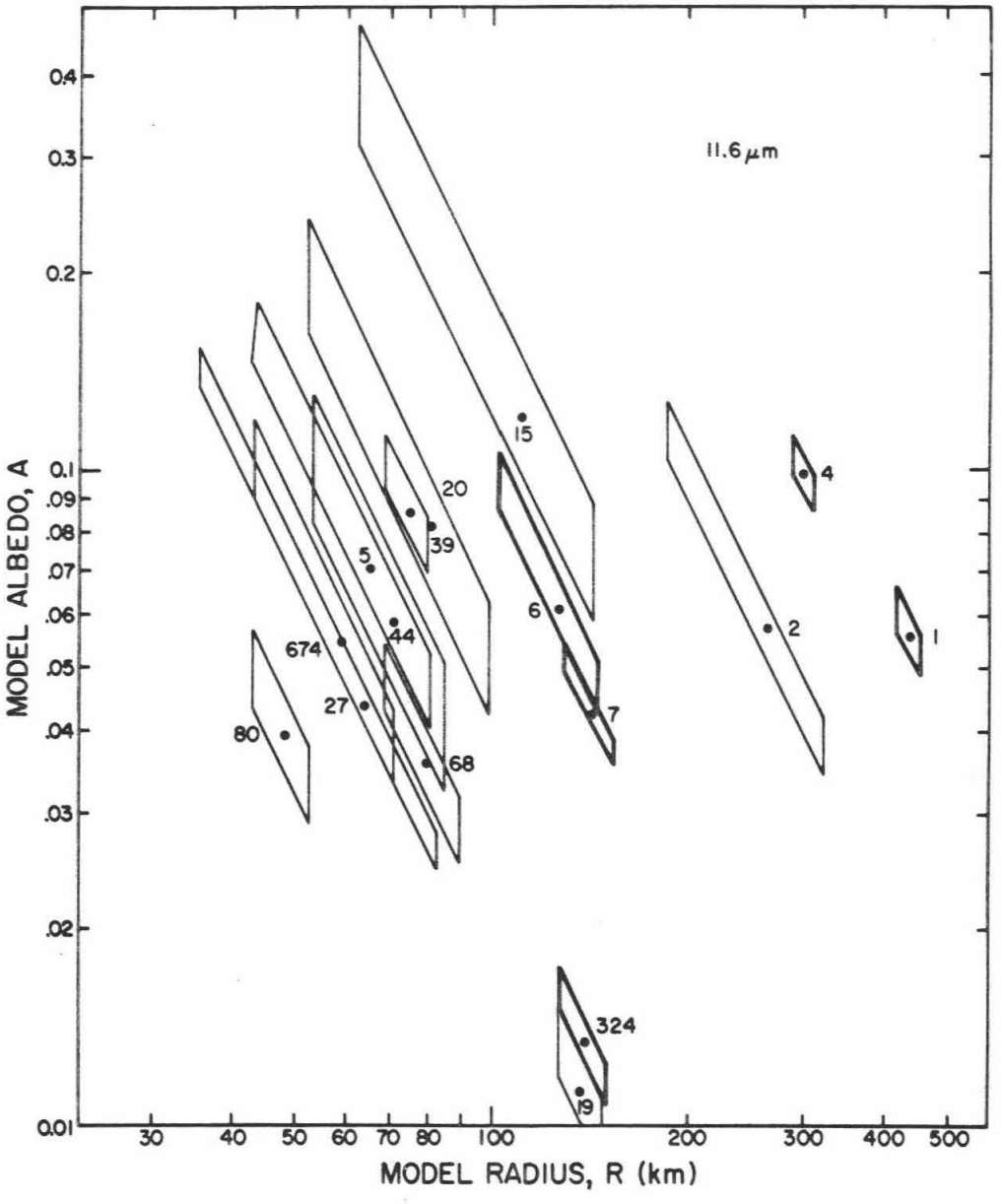
11.6 μm
MODEL ALBEDO, A
MODEL RADIUS, R (km)
0.4
0.3
0.2
0.1
.09
.08
.07
.06
.05
.04
.03
.02
0.01
30
40
50
60
70
80
100
200
300
400
500
15
20
39
5
44
674
27
80
68
6
7
4
2
1
324
19

Fig. 34

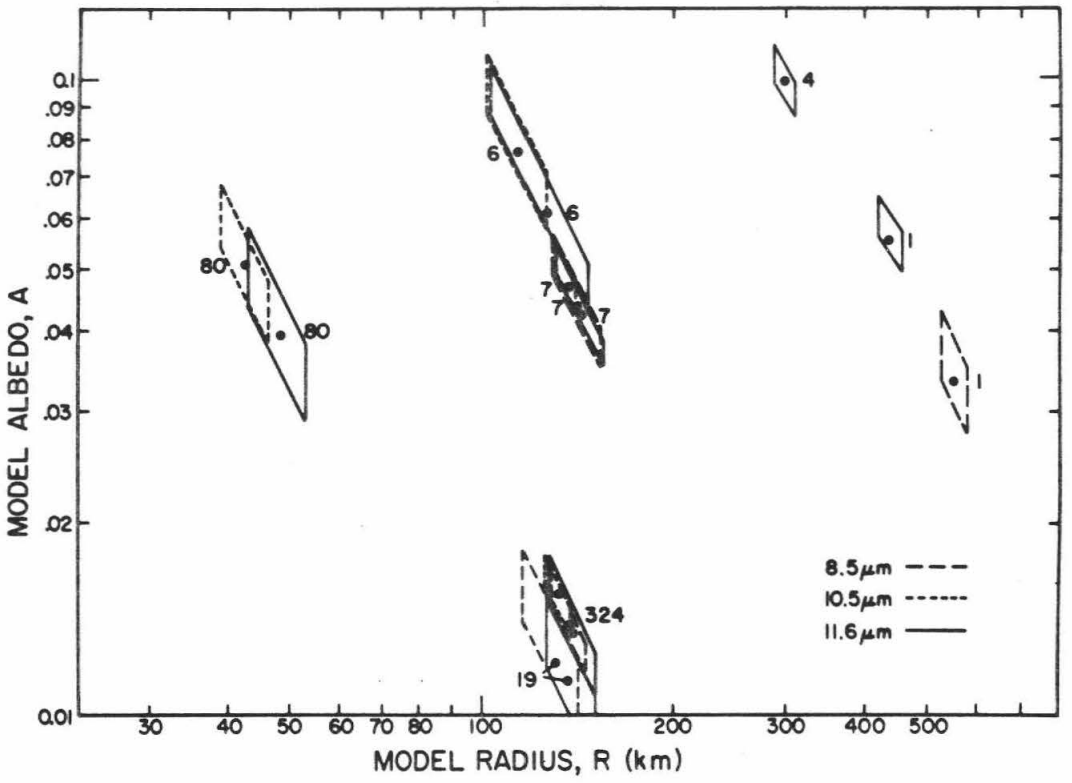
MODEL ALBEDO, A
0.1
.09
.08
.07
.06
.05
.04
.03
.02
0.01
30
40
50
60
70
80
100
200
300
400
500
MODEL RADIUS, R (km)
8.5μm
10.5μm
11.6μm
80
80
6
6
7
7
7
4
1
1
324
19

The situation for (1) Ceres has yet to be resolved as the 11.6 μm and the 8.5 μm data yield different model parameters.[1] Allen (1971) uses 6 observations to compute an infrared radius of 580 ± 40 km which overlaps with the 8.5 μm datum in Fig. 34. On the basis of polarimetry, Veverka (1970c) obtains a geometric albedo that lies between 0.03 and 0.05. It is quite possible that this low a geometric albedo is in conflict with the infrared data (Veverka 1971, private communication, and this author). Clearly, further study and observation of (1) Ceres are needed.

In conclusion, Figs. 33 and 34 show that there are clear and distinct differences between asteroids. These differences are relative and hold true even if the model radius systematically differs from the actual radius. The bolometric Bond albedo for real asteroids apparently has a range of at least an order of magnitude. Of the large asteroids ($R > 200$ km), (4) Vesta has the highest albedo. (324) Bamberga is extremely dark and also is much larger ($R \sim 125$ km) than hitherto suspected.

---

[1] (1) Ceres was observed twice at 11.6 μm and once at 8.5 μm (Table 1).

V. DISCUSSION

This section opens with a discourse on the relative importance of composition versus morphology in determining the albedo of an asteroid. The observed asteroid and satellite albedo distribution is discussed. Finally, the state of knowledge about the density of these objects is reviewed.

Surface Morphology and Composition

It is presumed that impact is the important on-going process that governs an asteroid's surface morphology. Asteroids are envisioned as being impacted regularly by particles of debris. In the limiting case, these collisions occur at supersonic velocities. The surface of the asteroid is pock-marked by craters and is mantelled by the ejecta which falls back to the surface. For Vesta it has been estimated that this fall-back amounts to more than 95 percent of the amount excavated originally from each crater (p. 91, this thesis). The corresponding number for a 100-km radius asteroid (with Vesta's density) is $\sim$60-70%.

There is evidence that both (4) Vesta and (8) Flora have developed regoliths. The observed polarization implies either fine porous or particulate surfaces. The observations, however, do not establish that the material is particulate and unfettered as opposed to being merely porous as is a tuff or cemented as is a conglomerate. That conclusion is supplied by the impact hypothesis. With a large percentage of the ejecta recovered as fall-back breccia on the surfaces of large asteroids, there is ample opportunity to rework it by

repeated impact before it finally escapes from the asteroid.

Not only does the impact hypothesis supply the fine particulate material required by the polarization data but it may also explain the observed lack of color changes across the surfaces of many asteroids. On asteroids the horizontal transport of impact debris is many times more significant than it is on the Moon or on the Earth. Not only is an asteroid's surface considerably smaller in surface area but the gravitational acceleration is also weaker. Consequently, each impact distributes throw-out over a large fraction of the entire surface. The trend, then, is toward the development of a global regolith that has a rather uniform texture and composition.

The impact hypothesis provides the basis for thinking that asteroids of comparable size tend to have similar surface morphologies. Of course, this is a statistical statement and there will be some variation. The major exceptions are expected to be the smaller objects which have recently been involved in cataclysmic collisions and those asteroids with high inclinations which give them a much lower probability for encountering debris. With these concepts, then, it is very difficult to explain the range of asteroidal albedos other than by compositional differences.

The darkening of the lunar surface is a process which at first may appear to clash with the above conclusion. It is likely that this process is due to the presence of dark glass in the lunar soil (Adams and McCord 1970). A second process that could be involved (in the sense that it cannot be ruled out) is the

coating of individual grains by opaque material of unknown composition, but presumably originating from solar wind sputtering and/or vapor deposition from meteorite impact (Hapke et al 1970). However, both of these possibilities are an expression of surface chemistry, and the previous conclusion stands.

In an attempt to identify compositional variations, a tentative albedo classification scheme is drawn up from the available data and presented as Table 7. In the sample observed, the extremely dark objects are clearly separated from the other objects (Figs. 33 and 34). On the other hand, the division between the "dark" and the "lunar" albedo classes is somewhat arbitrary inasmuch as here the data do not show a hiatus. The high albedo class is reserved for the Galilean satellites and Johnson's (1970, 1971) values are used.

(324) Bamberga and Other Dark Objects

Apparently Bamberga has the lowest (reliable) albedo yet measured for a solar-system object; thus relieving Phobos of this distinction. The Bond albedo for Phobos is not known but Smith (1970) has reported its geometric albedo to be about 0.065. Assuming that the lunar value for the phase integral is close to the correct value for Phobos, then the Bond albedo is probably in the range of 0.03 to 0.04, making Bamberga darker.

It is not immediately obvious why (324) Bamberga should be so dark. Not only must its surface material be intrinsically of low reflectivity but the morphology of Bamberga's surface must be such that very little scattered light escapes. This suggests a soil or regolith in which the particles are opaque. It is felt that

TABLE 7. ALBEDO CLASSIFICATION SCHEME
(numbers refer to Bond albedo)

Class:	Extremely Dark	Dark	Lunar	High Albedo**	
Type locality:	(324) Bamberga	(7) Iris	Moon	??	??
Members:	(324) Bamberga ~0.01 - 0.02	(7) Iris ~0.035 - 0.055	Moon ~0.07	(J4) Callisto ~0.15	(J1) Io ~0.46
	(19) Fortuna (?) ~0.012 (?)	(M1) Phobos* ~0.03 - 0.04	(4) Vesta ~0.1		(J2) Europa ~0.47
	(1) Ceres ?? ⟷	(1) Ceres ? ~0.03 - 0.04?	(6) Hebe ? ~0.045 - 0.1?	(J3) Ganymede ?? ⟷	(J3) Ganymede ~0.36
		(80) Sappho? ⟷ ~0.03 - 0.07?	(80) Sappho??		
		(68) Leto?? ~0.025 - 0.055	(20) Massalia?? ~0.07 - 0.11		

? Classification Tentative
?? Classification Speculative

*Using Smith's (1970) geometric albedo
**Satellite data from Johnson (1970, 1971)

both composition and morphology must be utilized in order to realize such a low albedo. By way of comparison, in the laboratory certain preparations of carbon black can have albedos this low or lower (Weast 1965).

Few measurements of meteorite albedos have been made. However, it is possible that some of the dark chondrites can have albedos as dark as that of Bamberga. Krinov (1960) has summarized his work during the 1930's and that of N.N. Sytinskaya which was carried out during 1952. The darkest meteorite which Krinov measured (the carbonaceous chondrite Staroe Boriskino) had a normal reflectivity of 4-5%. N.N. Sytinskaya measured 83 stony meteorites and she found 13 to have values in the 0.026 - 0.075 range.[1] More recent laboratory measurements have been made by Holt (1971, private communication) of the U.S. Geological Survey. He has studied the reflectivity of the carbonaceous chondrites Murray[2] and Mokoia[2]. At zero degrees phase angle, the reflectivities are ~0.05 and ~0.06 respectively. At thirty degrees, the corresponding values are ~0.04 and ~0.05.

It appears from these laboratory data than certain chondrites provide a plausible natural material that is also dark enough to match the

---

[1]The numbers quoted here are believed to refer to normal reflectivity averaged over the spectrum. The differing laboratory and astronomical geometries make intercomparison only approximate for any of the data.

[2]Samples provided by C. Moore from the collection at Arizona State University, Tempe, Arizona. The author is indebted to Dr. Holt for use of his unpublished data.

low albedo of Bamberga. Because of Bamberga's extreme darkness it is argued that the telescopic observations can be compared with the equivalent laboratory parameters for fresh surfaces. In favor of this argument are the facts that the laboratory and telescope measurements yield about the same values and that both Bamberga and the dark chondrites are at the bottom of their respective albedo scales. If the particles that compose Bamberga's regolith were originally opaque, it seems unlikely that significant darkening could occur either by the formation of glass as on the Moon (Adams and McCord 1970) or by thin coatings placed on individual grains by sputtering or by impact-produced vapors (Hapke et al 1970).

As has been mentioned before, the data for (19) Fortuna is not beyond question and the situation for (1) Ceres is unsettled. In the "dark" category, the data are good for both (7) Iris and Phobos with some uncertainty due to the phase integral of the latter.

The crucial question about the low albedo objects is their number and distribution. In the past the only way to estimate size and mass has been to assume values for the albedo and the density and to proceed by using the absolute magnitudes. If there is indeed a large number of dark and very dark asteroids, then our ideas about asteroids will have to be revised. For example, the mass estimates will be increased. As another example, if the Apollo family of asteroids has a common Bond albedo of several percent, then calculations of the probability for their impact with the Earth-Moon system will be revised upward.

From the available albedo and orbit information it appears that the dark objects are distributed throughout the asteroid belt: 1 Ceres (semimajor axis = 2.8 AU), 19 Fortuna (2.4 AU), 324 Bamberga (2.7 AU), Phobos (Mars: 1.5 AU), 7 Iris (2.4 AU), 80 Sappho (2.3 AU) and 68 Leto (2.8 AU). Since the sample of observed objects is heavily biased, no significance is given to the lack of distances greater than 3 AU. It is entirely possible that dark material could be abundant.

Anders (1964) has discussed Bamberga as a potential source of meteorites. He noted that the perihelion of Bamberga's orbit and the aphelion of Mars differ by only ~0.11 AU. However, the change in velocity required to transport ejecta from Bamberga into a Mars crossing orbit is large enough that the meteorites so produced would be significantly shocked. Anders concluded that Bamberga did not contribute appreciably to the earthward flux of the lightly shocked meteorites.

The fact that there are two dark objects, Bamberga and Phobos, near Mars, suggests the speculation that some other asteroids in this neighborhood also have low albedos. Presumably, a few of these asteroids will be close enough to Mars that low velocity ejecta from their surfaces can be perturbed into Mars crossing orbits and thence redirected on an Earth crossing trajectory. The details of this mechanism have been discussed by Anders (1964, 1971 and by authors therein cited). The contribution of Bamberga and Phobos is to place low albedo material very near, but not in, the source area for this particular mechanism.

Lunar Type Objects

The lunar class of objects contains the asteroids with the highest (precisely) measured albedos. Other asteroids might have higher albedos but this has yet to be demonstrated. The objects of this class are thought to resemble the Moon in many of their surface properties. (4) Vesta is the only asteroid which is firmly established as a member of this group and (6) Hebe and (20) Massalia are included only upon the basis of their albedos. (80) Sappho is a borderline case and probably is a member of the dark group typified by (7) Iris.

(4) Vesta is essentially spherical. Its bolometric Bond albedo is ~0.1 but the error bars do not rule out the lunar average value of ~0.07. The phase and opposition effects for these two bodies are very similar. Colorimetry data identify the surface composition (at least in part) as being consistent with the composition of certain basaltic achondrites (McCord et al 1970). The emissivity limit of $\varepsilon > 0.7$ found in this thesis is certainly compatible with any type of silicate composition. Frosts appear to be ruled out as a significant surface constituent both on the basis of the colorimetry which in that case should have detected a different spectrum and on the basis of the stability of volatiles (Watson et al 1963).

High Albedo Class

The members of the high albedo class are the Galilean satellites of Jupiter. No type localities are given because each of these objects is unique in its optical properties.

The high albedo class is suggestive of either a frost and ice surface or one composed of silicates with high albedo. Johnson and McCord (1970) have discussed the reflection spectrum of the Galilean satellites and have been unable to identify the surface composition on the basis of data from the 0.30 -1.10 μm region. Veverka (1971) concludes from the polarimetry and photometry data that J1, J2 and J3 have surfaces consisting of bright multiply-scattering material, such as a frost. J4 he finds to have a darker surface with the possibility of frost patches or a mixture of ice and dark silicates. Moroz (1966) discovered that in the region of 0.8 - 2.5 μm the spectra of J2 and J3 show structure that is characteristic of the reflection spectrum of a "snow cover". Recently this work has been confirmed by Johnson and McCord (1971). Furthermore, the absence of typical structure in the 0.8 - 2.5 μm spectrum of J1 and J3 does not rule out the possibility of frosts or ices (Johnson, 1971, private communication).

Currently there is no laboratory data available about the 8-14 μm appearance of frosts (Kieffer 1971, private communication). It is not obvious what the thermal emission observations mean (especially those of J4) and interpretation may have to await laboratory studies.

It is interesting to speculate that there may be asteroids with albedos as high as those of J1 and J2. (944) Hidalgo and the Trojans are a few of the asteroids that can retain frozen volatiles on their surfaces. If this is true, then asteroidal albedos could span a range of two orders of magnitude.

Densities

Hertz (1968) has derived a value for the mass of Vesta by studying perturbations of the asteroid (197) Arete. This mass is tabulated in Table 8 along with its formal error. Densities can be computed by using both the disk measurement and the photometric model radii. Schubart (1971) has used what he considers to be the best disk measurement (Dollfus' radius of 210 km) and finds the density to be near 5 g cm^{-3}. A lower density is obtained by using the photometric model radius and this value is entered near the bottom of Table 8. Allen (1971) has already published such a value and it differs only slightly from the present determination. However, the significance of these densities has not been previously discussed.

Upon inspection of Tables 8 and 9 it is obvious that the mass determination is forcing an important decision. On one hand the density implied by the disk measurement leads to reasoning that the composition of Vesta may be similar to stony iron meteorites or to that of terrestrial planets. On the other hand, the photometric model radius leads to the conclusion that Vesta is more closely related to (J4) Callisto or perhaps to the Moon.

TABLE 8. (4) VESTA DATA

Property	Value	Notes	Reference
Mass	$(1.20 \pm 0.08) \times 10^{-10} M_{\odot}$		Hertz 1968
	$(2.39 \pm 0.16) \times 10^{23}$ g		
Density	5 g cm^{-3}	1	Schubart 1971
	2.1 ± 0.9 g cm^{-3}	2	This thesis

[1]Using Dollfus' radius of 210 km

[2]Using the photometric model radius of 300 km

TABLE 9. DENSITY RANGE OF METEORITE TYPES*

Meteorite Type	Density
Stone	2.95 - 3.90 g cm^{-3}
Iron	7.7 - 7.9 g cm^{-3}
Stony Iron	4.6 - 4.9 g cm^{-3}

*data from Wood (1963)

Vesta is now compared with the Galilean satellites using a plot first published by Johnson (1970, 1971). The purpose of the plot, Fig. 35, is to compare objects in terms of their surface (geometric albedo) and bulk (density) properties. The Vesta data are converted to geometric albedo because it is felt that the assumption of $q = 0.585$ (the lunar value) fits the available asteroid data better than it fits the Galilean satellite data.

Great care must be exercised in drawing conclusions from this particular plot. Veverka (1970c) has also studied this matter and he prefers to use the masses determined by de Sitter (1931) and the diameters from the double image micrometer measurements by Dollfus (1970). The densities that result are then (J1):2.5, (J2):3.0, (J3):1.7 and (J4):1.3 g cm^{-3}. Veverka's values for J1 and J3 are lower than the extent of the error bars drawn in Fig. 35. There are also other difficulties with this plot.

Brian Marsden (1971 private communication) points out that the mass determinations for J4 have a range of about a factor of 2. He notes that de Sitter's 1931 determination is based upon data obtained since 1890. If earlier data are considered then larger values are obtained for the mass. De Sitter's value is favored by Marsden although this matter is not completely closed. Marsden also notes that the mass situation for J1 is perhaps more serious. Though the range of the individual determinations is less (about a factor of one-and-one-half, discarding some of the earliest determinations), the cause of the variation for J1 has yet to be identified.

Fig. 35. Geometric albedo versus density after Johnson (1970, 1971). The point for each satellite represents the mean values of p and ρ for Johnson's choice of diameter. For the satellites, the density error bar gives the range of Sampson's and de Sitter's mass determinations (see de Sitter 1931 for data and references). The geometric albedo range is determined from the rotation variation measured by Johnson. The regions indicated for each satellite indicate the limits of the given error bars for the range of diameters considered by Johnson. The position plotted for Vesta corresponds to the photometric model radius of 300 km and model albedo of 0.1 The infrared data are interpreted as indicating that Vesta is closest in both bulk and surface properties to either (J4) Callisto or, possibly, the Moon. $q = 0.585$ is assumed for Vesta.

Fig. 35

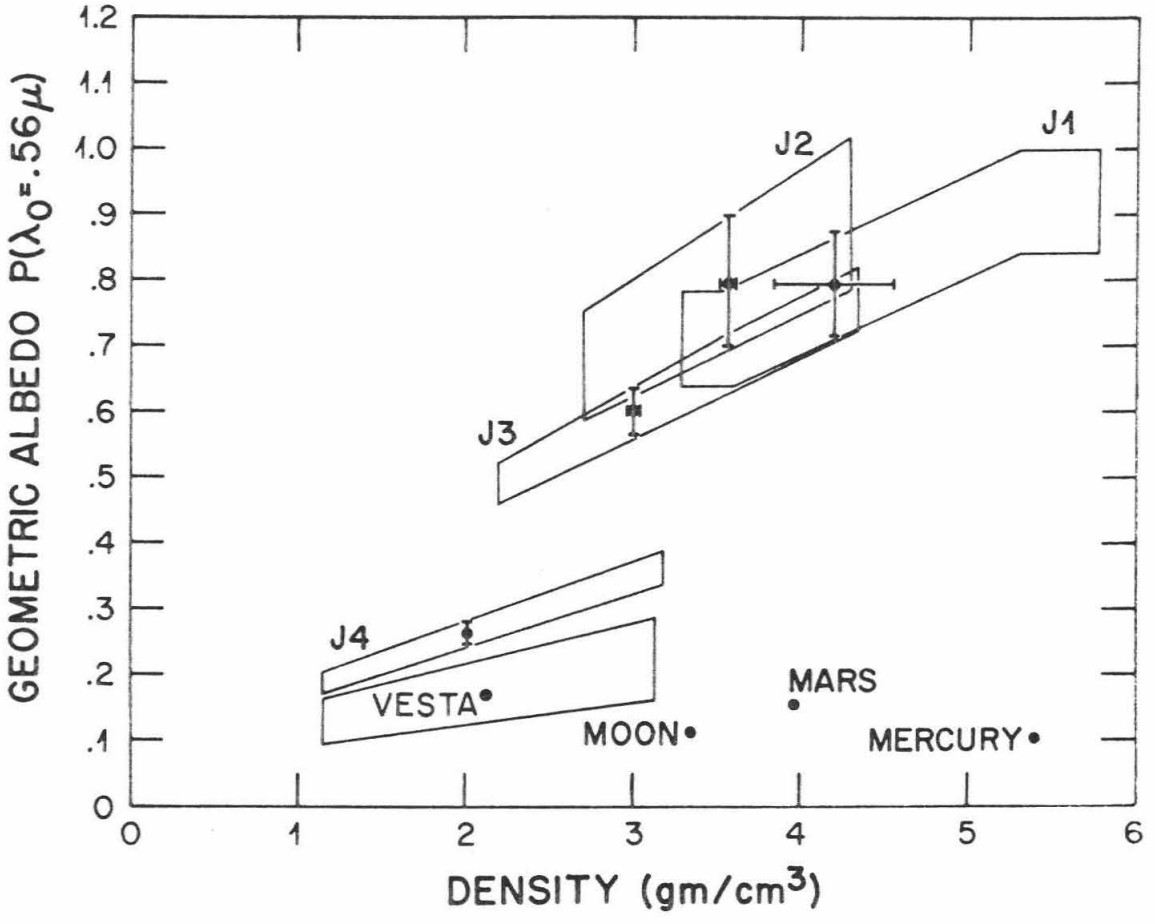
GEOMETRIC ALBEDO P(λ0=.56μ)
1.2
1.1
1.0
.9
.8
.7
.6
.5
.4
.3
.2
.1
0
0
1
2
3
4
5
6
DENSITY (gm/cm3)
J1
J2
J3
J4
VESTA
MOON
MARS
MERCURY

With the low densities which Veverka assigns, a solar abundance mixture of ices and chondritic materials is certainly possible for the bulk composition of J3 and J4. However, the present errors in density also admit a lunar-like density ~ 3.3 g cm^{-3}. With Johnson's (1970, 1971) values, which are plotted in Fig. 35, ice is plausible for J4 but so is a silicate composition. The lunar density is also agreeable with the data for J1 and J2 (the error bars for J1 are now larger than those drawn in Fig. 35 due to the range of the various J1 mass determinations).

The error bars for Vesta in Fig. 35 are obtained by (1) tripling the formal error in the mass determination and (2) assuming that the error in volume of the photometric model is 45 percent. While Vesta could have the same density as the Moon, the data suggest that the actual value is probably somewhat less. If the true density is near this higher value, then silicates are the likely bulk composition. If the actual value should be at a low value near ~ 1.1 g cm^{-3} then ices are indicated. In this case, the bulk and surface compositions would be vastly different, as a surface of basaltic achrondrite composition suggests that the individual particles have a density of ~ 3 g cm^{-3}.

In conclusion, the infrared data show that Vesta's surface and bulk properties probably lie somewhere between those of the Moon and (J4) Callisto.

VI. FUTURE WORK

The fundamental questions about the smaller bodies in the solar system cannot be fully answered until more is known about the asteroids. For example: "What are the asteroids? How are they related to comets and to meteorites?"

The important observational work in the immediate future is to continue to survey the asteroids both by infrared photometry and by visible-wavelength colorimetry. The work should be oriented toward identification of compositional classes. How many different types of asteroids are there and how many of them have extremely low albedos? Can any objects be found that require low values of effective emissivity (e.g. iron) in order to explain the infrared data? Thus, in order to characterize the asteroids as a whole, the 50 brightest minor planets should be observed.

There are several specific groups of asteroids that have special significance due to their relationship to particular problems. The asteroids close to Mars should be observed because of their proximity to the source area for one of the mechanisms for delivering meteorites to the Earth. The Mars crossers listed by Öpik (1963) are the most desirable of these targets but they are by and large very faint and only some of the brightest members can be investigated with presently available equipment.

The origin of asteroidal families may be a question that can be answered by telescopic observations. This type of study would sample two or three of the

brightest families, measuring all members within the reach of observational technology. If families are homogeneous, but differences exist between different families then breakup of a parent object would be strongly suspected. On the other hand, if the objects within a family differ one from the other, then breakup is not disproved because the parent object could have been differentiated. In this case too, dynamical processes that cause clumping of asteroids might also be suspected.

The observational distinction between comets and asteroids is fuzzy. It will be recalled that the comets P/Arend-Rigaux and P/Neujmin 1 showed slight but definite cometary activity only upon their discovery apparitions. At all other times they have been completely asteroidal in appearance. Thus, in the present classification scheme, all burned-out comets would be asteroids. On the basis of the dynamical parameters of orbits, Marsden (1971) has compiled a list of objects which may be defunct comets. The brightest objects on Marsden's list should be observed as soon as a sample of normal asteroids is available for comparison. Hopefully, these measurements will yield a good observational criterion that separates the defunct comets from "normal" asteroids. (944) Hidalgo, which is always mentioned in this context, is on this list and it is doubly interesting because Arnold (1965) found from his Monte Carlo calculations that it was highly probable that (944) Hidalgo had formerly been a long-period comet. Unfortunately its mean opposition magnitude is +19.

The ground-based study of asteroidal surface morphologies is more difficult because the observable effects are smaller. Visible-wavelength polarimetry is presently the important tool for detecting a porous or particulate surface layer. Under favorable circumstances the infrared photometry can yield estimates for the thermal inertia and the colorimetry can provide evidence for a thin or poorly developed regolith if it finds color differences across the surfaces of individual asteroids. A theoretical study of the surface morphology that arises in the case of hypervelocity impact is indicated. This study would characterize the morphological sequence of regolith types as a function of the parent body's mass. Such a theoretical study is important because of the very limited types of data that show up the differences in morphology and the difficulty of interpreting the available data in terms of soil parameters.

VII. SUMMARY

The purpose of this summary is to briefly draw together some of the original contributions of Part 2 of this thesis.

The infrared lightcurve and phase effect data presented in the observation section is the only information on these effects that is available for thermally emitted radiation from the asteroids. The infrared lightcurves yield only several minor conclusions because the effect is small (for the particular asteroids that were observed), and is probably less than the scatter of the data. The thermal emission phase effect for a rapidly rotating ($\sim 5^h$ period) asteroid at wavelengths near 10 μm is small and is less pronounced than the corresponding visible-wavelength phase effect. Special color diagrams are introduced in order to display the observational data and to compare the reflected and emitted light from asteroids. These diagrams are very important because they allow variations in surface properties between different asteroids to be detected without recourse to model-dependent assumptions. As a result, it was discovered that there are real differences between the surfaces of (324) Bamberga on one hand and (7) Iris, (80) Sappho, (192) Nausikaa and perhaps (313) Chaldaea on the other. (6) Hebe and (20) Massalia are found to differ from (19) Fortuna and (145) Adeona. (19) and (145) also are distinct from (7) Iris.

A detailed thermal model is explained in section III. Justification for using this lunar-type model is given and the model is used to compute typical phase functions (beam patterns) and spectra for a hypothetical asteroid.

In the fourth section the data for (J3) Ganymede, (J4) Callisto, (4) Vesta, (324) Bamberga and (7) Iris are analyzed with the model just developed and with other, less complicated models. A short, digressive analysis of disk measurements is made in order to obtain diameters to use for the modelling of the first three objects. (J3) Ganymede is found to have a bolometric Bond albedo of about 0.12 ± 0.10. This is the first estimate for this quantity that involves no assumption about the visible-wavelength phase integral, q. For (J4) Callisto, it is found that the present observations cannot be satisfied by a lunar-type model.

The analysis for (4) Vesta finds that the infrared data and the disk diameter measurements are incompatible. The only remedy is to reject the disk measurements because no model using the disk diameters could be found that satisfied all of the available infrared and visible photometry, colorimetry and polarization data. On the basis of this thesis and the concurrent work of D.A. Allen (1970), (4) Vesta is thought to have a bolometric Bond albedo near 0.10 ± 0.03, a true radius near the model value of 300^{+50}_{-30} km. Any value for emissivity greater than 0.7 is found to be compatible with the infrared data.

The analysis for (7) Iris and (324) Bamberga finds that the model parameters for these asteroids are about $A \sim 0.04 - 0.05$, $R \sim 130 - 150$ km and $A \sim 0.013 - 0.018$, $R \sim 120 - 140$ km respectively. It is found that the error propagation for very low albedo objects is favorable and that (324) Bamberga's actual bolometric Bond albedo is probably less than 0.03 even if the several types of errors act in fortuitous combination.

From plots of model albedo versus model radius, it is found that most of the asteroids analyzed (which constitute a very biased sample) have model albedos between 0.03 and 0.1. Several objects, (324) Bamberga, (19) Fortuna and perhaps (1) Ceres, appear to be extremely dark with albedos in the 0.01 - 0.03 range.

It is felt that impact is the important on-going process on asteroidal surfaces. For (4) Vesta, it is estimated that more than 95 percent of the ejecta returns to that asteroid's surface. Thus there is ample opportunity to rework the surface material by repeated impact and to distribute it over the entire surface of the asteroid. The impact hypothesis also provides the basis for thinking that asteroids of equal mass tend to have similar surface morphologies. This leads to the conclusion that albedo differences between asteroids are largely an expression of compositional differences.

In an attempt to isolate some of the prospective compositional types, objects are classified according to albedo: extremely dark, dark, lunar, and high albedo. (324) Bamberga is so dark that it is difficult to find laboratory data for comparison. Carbonaceous chondrites are made of a plausible, naturally occurring material that appears to be dark enough that it could explain the (324) Bamberga data. Other possibilities might exist but laboratory data are lacking. On the basis of the present observations there is no reason not to believe that the dark asteroids are uniformly distributed within the asteroid belts, so it is entirely possible that dark material could be abundant.

It is interesting to note that both (324) Bamberga and the small satellite, Phobos, are both low albedo objects in the vicinity of Mars. They are both close to, but not in, the source area of one particular mechanism for delivering (lightly shocked and unshocked) meteorites to the Earth via perturbation of their orbits upon close approach to Mars (as discussed by Anders 1964, 1971 and by authors therein cited).

Using Hertz's (1968) mass, a density can be computed for (4) Vesta. When a 300-km radius is used, Vesta's density is 2.1 ± 1.0 g cm^{-3}. Considering both Vesta's surface albedo and density, it is suggested that this asteroid is more analogous to (J4) Callisto or perhaps even to the Moon than it is to the terrestrial planets.

REFERENCES

Adams, John B. and Thomas B. McCord, (1970), Remote Sensing of Lunar Surface Mineralogy: Implications from Visible and Near-Infrared Reflectivity of Apollo 11 Samples, Proceedings of the Apollo 11 Lunar Science Conference, 3, 1937-1945 (Geochimica et cosmochimica, ACTA, Supplement 1).

Ahmad, Imam I. (1954), Photometric Studies of Asteroids. IV. The Light-Curves of Ceres, Hebe, Flora, and Kalliope, Ap. J. 120, 551-559.

Allen, C.W., (1963), Astrophysical Quantities, 2nd edition, Athlone Press, London.

Allen, David A., (1970), Infrared Diameter of Vesta, Nature 227, 158-159.

Allen, David A. (1971), Infrared Diameters of Asteroids, in Physical Studies of Minor Planets, T. Gehrels, ed. (Proceedings of the 12th Colloquium of the I.A.U., Tucson, Arizona, March 8-10, 1971).

Anders, Edward (1964), Origin, Age and Composition of Meteorites, Space Sci. Rev. 3, 583-714.

Anders, Edward, (1971) Interrelations of Meteorites, Asteroids, and Comets, in Physical Studies of Minor Planets, T. Gehrels, ed. (Proceedings of the 12th Colloquium of the I.A.U., Tucson, Arizona, March 8-10, 1971).

Arnold, James R., (1965a), The Origin of Meteorites as Small Bodies, II. The Model, Ap. J. 141, 1536-1547.

Arnold, James R., (1965b), The Origin of Meteorites as Small Bodies, III. General Considerations, Ap. J. 141, 1548-1556.

Buhl, David, William J. Welch and Donald G. Rea, (1968a), Reradiation and Thermal Emission from Illuminated Craters on the Lunar Surface, JGR 73, 5281-5295.

Buhl, David, William J. Welch and Donald G. Rea (1968b), Anomalous Cooling of a Cratered Lunar Surface, JGR 73, 7593-7608.

Cailliatte, Charles, (1965), Contribution a L'Etude des Asteroides Variables, Bull. Astr. Paris 20, 283.

Chapman, Clark R., Torrence V. Johnson, and Thomas B. McCord, (1971), A Review of Spectrophotometric Studies of Asteroids, in Physical Studies of Minor Planets, T. Gehrels, ed. (Proceedings of the 12th Colloquium of the I.A.U., Tucson, Arizona, March 8-10, 1971).

de Sitter, W. (1931), Jupiter's Galilean Satellites, MNRAS 91, 706.

Dollfus, A., (1970), Diametres des Planetes et Satellites, Chapter 2 of Surfaces and Interiors of Planets and Satellites, Dollfus, Ed. Academic Press.

Dunlap, J.L., (1971), Laboratory Work on the Shape of Asteroids, in Physical Studies of Minor Planets, Editor T. Gehrels (Proceedings of the 12th Colloquium of the I.A.U., Tucson, Arizona, March 8-10, 1971).

Dunlap, J.L., and T. Gehrels, (1969), Minor Planets, III. Lightcurves of a Trojan Asteroid, Ap. J. 74, 796-803.

Gault, Donald E., Eugene M. Shoemaker and Henry J. Moore (1962), Spray Ejected from the Lunar Surface by Meteoroid Impact, NASA Technical Note D-1767.

Gehrels, Thomas, (1956), Photometric Studies of Asteroids, V. The Light-Curve and Phase Function of 20 Massalia. Ap. J. 123, 331-338.

Gehrels, Thomas, (1957), Photometric Studies of Asteroids, VI. Photographic Magnitudes, Ap. J. 125, 550-570.

Gehrels, Thomas, (1967a), Minor Planets, I. The Rotation of Vesta. Ap. J. 72, 929-938.

Gehrels, Thomas, (1967b), Minor Planets, II. Photographic Magnitudes, Ap. J. 72, 1288-1291.

Gehrels, Thomas, (1970), Photometry of Asteroids, Chapter 6 of Surfaces and Interiors of Planets and Satellites, Ed. Dollfus, Academic Press, 317-375.

Gehrels, Thomas, T. Coffeen, and D. Owings, (1964), Wavelength Dependence of Polarization III. The Lunar Surface, A. J. 69, 826-852.

Gehrels, Thomas and D. Owings, (1962), Photometric Studies of Asteroids. IX. Additional Light-Curves, Ap. J. 135, 906-924.

Gillett, F.C., K.M. Merrill, and W.A. Stein, (1970), Albedo and Thermal Emission of Jovian Satellites I-IV, Astrophys Letters 6, 247-249.

Gold, T., J.J. Campbell, and B.T. O'Leary, (1970), Optical and High-Frequency Electrical Properties of the Lunar Sample, Science 167, 707-709.

Hapke, B.W., A. J. Cohen, W. A. Cassidy and E. N. Wells, (1970) Solar Radiation Effects on the Optical Properties of Apollo 11 Samples, Proceedings of the Apollo 11 Lunar Science Conference, 3, 2199-2212 (Geochimica et cosmochimica ACTA, Supplement 1).

Harris, Daniel L., (1961), Photometry and Colorimetry of the Planets and Satellites, Chapter 8 of Planets and Satellites, G.P. Kuiper and B.M. Middlehurst, eds., University of Chicago Press, Chicago.

Hertz, Hans G., (1968), Mass of Vesta, Science 160, 299-300.

Ingrao, Hector C., Andrew T. Young, and Jeffrey L. Linsky, (1966), A Critical Analysis of Lunar Temperature Measurements in the Infrared, Chapter 10 in Nature of the Lunar Surface, Hess et al, ed., The Johns Hopkins Press, Baltimore.

Jaeger, J.C., (1953a), Conduction of Heat in a Solid with Periodic Boundary Conditions, with an Application to the Surface Temperature of the Moon, Proc. Camb. Phil. Soc. 49, 355-359.

Jaeger. J. C., (1953b), The Surface Temperature of the Moon, Australian Journal of Physics 6, 10-21.

Jaeger, J.C., and Harper, A.F.A. (1950) Nature of the Surface of the Moon, Nature 166, 1026.

Johnson, H. L., (1963), Photometric Systems, Chapter 11 in Basic Astronomical Data (Stars and Stellar Systems Vol. III), K. Aa. Strand, Ed., University of Chicago Press, Chicago.

Johnson, Torrence Vaino, (1970), Albedo and Spectral Reflectivity of the Galilean Satellites of Jupiter, Ph.D. Thesis, California Institute of Technology, 58.

Johnson, Torrence V., (1971), Galilean Satellites: Narrowband Photometry 0.30 to 1.10 Microns, Icarus 14, 94-111.

Johnson, T.V. and T.B. McCord, (1970), Galilean Satellites: The Spectral Reflectivity 0.30 - 1.10 Microns, Icarus 13, 37-42.

Johnson, T.V. and T.B. McCord, (1971), Spectral Geometric Albedo of the Galilean Satellites - 0.3 to 2.5 μ, presented at American Astronomical Society, Division for Planetary Science, February 1-3, 1971, Tallahassee, Florida.

KenKnight, C.E., D.L. Rosenberg, and G.K. Wehner, (1967) Parameters of the Optical Properties of the Lunar Surface Powder in Relation to Solar Wind Bombardment, JGR 72, 3105-3129.

Krinov, E.L. (1960), Principles of Meteoritics, translated from the Russian by Irene Vidziunas and Harrison Brown, Pergamon Press, New York.

Labs, Dietrich, and Heinz Neckel, (1968), The Radiation of the Solar Photosphere from 2000 Å to 100μ, Zeitschrift für Astrophysik 69, 1-73.

Linsky, Jeffrey L. (1966), Models of the Lunar Surface Including Temperature-Dependent Thermal Properties, Icarus 5, 606-634.

Low, Frank J., (1965), Planetary Radiation at Infrared and Millimeter Wavelengths (sic), Lowell Obs. Bull., Vol. 6, 184-187.

Low, Frank J., (1970), Sky Survey, Semi-Annual Technical Report, Air Force Cambridge Research Laboratories, AFCRL-70-0179.

Marsden, B.G., (1970), On the Relationship between Comets and Minor Planets, Ap. J. 75, 206-217.

Marsden, B.G., (1971), Evolution of Comets into Asteroids? in Physical Studies of Minor Planets, Ed. T. Gehrels (Proceedings of the 12th Colloquium of the I.A.U. Tucson, Arizona, March 8-10, 1971).

McCord, Thomas B., John B. Adams, and Torrence V. Johnson, (1970), Asteroid Vesta: Spectral Reflectivity and Compositional Implications, Science, 168, 1445-1447.

Moroz, V.I. (1966), Infrared Spectrophotometry of the Moon and the Galilean Satellites of Jupiter, Soviet Astronomy, AJ 9, 999-1006.

Morrison, D., D.P. Cruikshank, R.E. Murphy, T.Z.Martin, J.G.Beery, and J.H.Shipley, (1971), Thermal Inertia of Ganymede from 20 Micron Eclipse Radiometry, preprint.

Murcray, Frank H., (1965), The Spectral Dependence of Lunar Emissivity, JGR 70, 4959-4962.

Murray, Bruce C., Robert L. Wildey, James A. Westphal, (1965), The Eclipse Cooling of Ganymede, Ap. J. 141, 1590-1592.

Murray, Bruce C., Robert L. Wildey, James A. Westphal, (1964), Observations of Jupiter and the Galilean Satellites at 10 Microns, Ap. J. 139, 988-993.

Nicodemus, F.E., (1970), Reflectance Nomenclature and Directional Reflectance and Emissivity, App. Opt. 9, 1474-1475.

Oetking, Phillip, (1966), Photometric Studies of Diffusely Reflecting Surfaces with Applications to the Brightness of the Moon, JGR 71, 2505-2513.

O'Leary, T.B., and D.G. Rea, (1968), The Opposition Effect of Mars and its Implications, Icarus 9, 405-428.

Opik, E.J., (1963), Survival of Comet Nuclei and the Asteroids, Adv. in Astronomy and Astrophysics 2, 219-262, Academic Press, New York.

Richardson, P.D. and Y.M. Shum, (1968), Surface Temperatures of the Galilean Satellites of Jupiter, Nature 220, 897-898.

Saari, J.M., and R.W. Shorthill, (1967), Review of Lunar Infrared Observations, in Physics of the Moon, Singer, ed., AAS, Science and Technology Series, 13, 57.

Schubart, Joachim, (1971), Asteroid Masses and Densities, in Physical Studies of Minor Planets, ed. T. Gehrels (Proceedings of the 12th Colloquium of the I.A.U., Tucson, Arizona, March 8-10, 1971).

Smith, Bradford A., (1970), Phobos: Preliminary Results from Mariner 7, Science 168, 828-830.

Stebbins, J., (1927), The Light Variations of the Satellites of Jupiter and their Application to the Measures of the Solar Constant, Lick Obs. Bull. 13, 1.

Stebbins, J. and T.S. Jacobsen, (1928), Further Photometric Measures of Jupiter's Satellites and Uranus, with Tests for the Solar Constant, Lick Obs. Bull. 13, 180.

Taylor, R.C., (1971), Photometric Observations and Reductions of Light-curves of Asteroids, in Physical Studies of Minor Planets, T. Gehrels ed. (Proceedings of the 12th Colloquium of the I.A.U., Tucson, Arizona, March 8-10).

U.S.S.R., Academy of Sciences, Institute for Theoretical Astronomy, Leningrad, 1969-70, Ephemerides of Minor Planets.

Vesely, Carl D., (1971), Summary of Orientations of Rotation Axes in Physical Studies of Minor Planets, T. Gehrels, ed. (Proceedings of of the 12th Colloquium of the I.A.U., Tucson, Arizona, March 8-10, 1971).

Veverka, J., (1970a), Photopolarimetric Observations of the Minor Planet Flora, Cornell University Center for Radiophysics and Space Research CRSR 417 (submitted to Icarus).

Veverka, J., (1970b), The Polarization Curve and the Absolute Diameter of Vesta, Cornell University Center for Radiophysics and Space Research, CRSR 421.(submitted to Icarus).

Veverka, J., (1970c), Photometric and Polarimetric Studies of Minor Planets and Satellites, Ph.D. Thesis, Harvard.

Veverka, J. , (1971a), Brightness - and Polarization - Phase Relationships, in Physical Studies of Minor Planets, T. Gehrels, ed. (Proceedings of the 12th Colloquium of the I.A.U., Tucson, Arizona, March 8-10, 1971).

Veverka, J., (1971b), Polarization Measurements of the Galilean Satellites of Jupiter, Icarus 14, 355-359.

Veverka, J., and W. Liller, (1969), Observations of Icarus: 1969, Icarus 10, 441-444.

Watson, Kenneth, (1964), I. The Thermal Conductivity Measurements of Selected Silicate Powders in Vacuum from 150° - 350°K. II. An Interpretation of the Moon's Eclipse and Lunation Cooling as Observed Through the Earth's Atmosphere from 8-14 Microns, Ph.D. Thesis, California Institute of Technology.

Watson, Kenneth, Bruce C. Murray and Harrison Brown, (1963), The Stability of Volatiles in the Solar System, Icarus 3, 317-327.

Weast, Robert C. ed., (1965), Handbook of Chemistry and Physics, 46th Edition, The Chemical Rubber Co. Cleveland.

Wesselink, A.J., (1948), Heat Conductivity and Nature of the Lunar Surface Material, B.A.N. 10, 351-363.

Widorn, Thomas, (1967), Zur photometrischen Bestimmung der Durchmesser der Kleinen Planeten, Annalen der Universitäts-Sternwarte, Wien 27, 112-119.

Winter, D.G. and J.A. Krupp, (1970), Directional Characteristics of Infrared Emission from the Moon, Boeing Scientific Research Laboratory Document DI-82-0987; also, The Moon 2, 279-292 (1971).

Winter, D.F. and J.M. Saari, (1969), A Particulate Thermophysical Model of the Lunar Soil, Ap. J. 156, 1135-1151.

Wood, J.A., (1963), Physics and Chemistry of Meteorites, Chapter 12 in The Moon, Meteorites and Comets, G.P. Kuiper and B.M. Middlehurst, eds., University of Chicago Press, Chicago.

APPENDICES

APPENDIX I.

ASTEROID DATA TABLES

These tables tabulate the data discussed
in Part 2 of this thesis

TABLE 1. 4 VESTA, LIGHTCURVE DATA

Date 1969-70 U.T.		λ (μm)	Wt.	$E \cdot \Delta^2$ W $cm^{-2} \mu m^{-1}$ $\times 10^{-15}$	Fractional Period
Dec.	2.503	11.6	1	2.86±0.46	0.118
	2.509	11.6	1	2.49±0.41	0.146
	4.480	11.6	1	2.45±0.36	0.000
	4.518	11.6	1	2.40±0.41	0.172
	4.539	11.6	1	2.65±0.4	0.268
Jan.	13.469	8.5	1/2	1.92±0.20	0.149
	13.493	8.5	1	1.90±0.20	0.254
Feb.	7.393	11.6	1	2.83±0.33	0.428
	7.441	11.6	1	2.57±0.29	0.641
	8.367	11.6	1	2.83±0.34	0.817
	8.377	8.5	1	1.86±0.21	0.859
	8.404	11.6	1	2.67±0.32	0.982
	8.422	8.5	1	1.81±0.19	0.063
Apr.	2.236	11.6	1	2.51±0.64	0.996
	2.249	11.6	1	2.68±0.61	0.056
	3.242	8.5	1	1.60±0.25	0.527
	3.250	10.5	1	2.00±0.25	0.565
	3.280	11.6	1	2.12±0.45	0.698
	4.140	11.6	1	2.71±0.34	0.573
	4.146	8.5	1	1.53±0.19	0.602
	4.152	10.5	1	2.15±0.31	0.628
	4.190	11.6	1	2.33±0.29	0.799
	4.199	8.5	1	1.59±0.18	0.839

(continued on next page)

- continued -

TABLE 1. 4 VESTA, LIGHTCURVE DATA

Date 1969-70 U.T.		λ (μm)	Wt.	$E \cdot \Delta^2$ W $cm^{-2}\mu m^{-1}$ $\times 10^{-15}$	Fractional Period
Apr.	4.208	10.5	1	1.83±0.28	0.881
	4.231	11.6	1	2.49±0.31	0.982
	4.238	8.5	1	1.65±0.20	0.016
	4.247	10.5	1	1.85±0.28	0.057
	4.268	11.6	1	2.47±0.31	0.149
	4.278	8.5	1	1.59±0.22	0.195
	4.287	10.5	1	2.04±0.34	0.237
	4.310	11.6	1	2.98±0.40	0.338
	4.320	8.5	1	1.65±0.26	0.385
	4.332	10.5	1/2	1.76±0.37	0.426
	5.153	10.5	1/2	2.25±0.42	0.135
	5.162	11.6	1	2.86±0.34	0.177
	5.172	8.5	1	1.61±0.20	0.731
	5.221	11.6	1	2.75±0.53	0.443
	5.227	11.6	1	2.84±0.34	0.470
	5.238	8.5	1	1.53±0.62	0.520
	5.249	10.5	1/2	1.78±0.37	0.570

TABLE 2. 7 IRIS, LIGHTCURVE DATA

Date 1969-70 U.T.		λ (μm)	Wt.	$E \cdot \Delta^2$ W $cm^{-2}\mu m^{-1}$ $\times 10^{-15}$	Fractional Period
Aug.	23.501	10.5	1	1.02±0.16	0.000
	23.514	11.6	1/2	1.19±0.18	0.042
	23.525	8.5	1	.79±0.13	0.081
	24.476	8.5	1	.86±0.40	0.286
	24.478	11.6	1	1.08±0.20	0.293
	24.480	10.5	1	.98±0.13	0.300
	25.430	10.5	1	1.02±0.17	0.505
	25.458	10.5	1	1.14±0.17	0.598
	25.487	10.5	1	.92± 0.14	0.699
	27,466	11.6	1	1.15±0.20	0.373
	27.472	11.6	1	1.07±0.13	0.391
	27.505	11.6	1/2	.91± 0.13	0.503
Sept.	18.417	10.5	1/2	1.01±0.11	0.411
	18.425	11.6	1	1.29±0.16	0.439
	18.433	8.5	1	1.07±0.16	0.465
	18.485	10.5	1/2	.97±0.11	0.641
	19.266	10.5	1	1.13±0.13	0.284
	19.367	10.5	1	1.05±0.12	0.616
	19.425	10.5	1	1.18±0.14	0.812
	19.432	11.6	1	1.43±0.18	0.833
	19.437	8.5	1	1.15±0.16	0.850
Oct.	12.393	11.6	1	1.36±0.20	0.281

(continued on next page)

- continued -

TABLE 2. 7 IRIS, LIGHTCURVE DATA

Date 1969-70 U.T.		λ (μm)	Wt.	$E \cdot \Delta^2$ W $cm^{-2}\mu m^{-1}$ $\times 10^{-15}$	Fractional Period
Dec.	1.234	11.6	1	1.37±0.26	0.398
	2.268	11.6	1	.89±0.15	0.885
	2.291	11.6	1	.86±0.13	0.962
	3.228	11.6	1	1.05±0.10	0.123
	3.249	11.6	1	1.07±0.08	0.195
	4.168	11.6	1	.92±0.14	0.295
	4.189	11.6	1	1.39±0.15	0.365
	4.285	11.6	1	1.03±0.15	0.690

TABLE 3. 6 HEBE, LIGHTCURVE DATA

Date 1969-70 U.T.		λ (μm)	Wt.	$E \cdot \Delta^2$ W $cm^{-2}\mu m^{-1}$ $\times 10^{-15}$	Fractional Period
Oct.	12.550	11.6	1	0.43±0.12	0.500
Dec.	4.398	11.6	1	0.88±0.14	0.322
	4.420	11.6	1	0.72±0.15	0.396
	4.440	11.6	1/2	0.56±0.10	0.460
	4.469	11.6	1/2	0.29±0.07	0.556
	4.510	11.6	1/2	0.58±0.11	0.694
Jan.	13.383	8.5	1/2	0.41±0.06	0.595
	13.411	8.5	1	0.32±0.03	0.684
Feb.	7.310	11.6	1/2	0.59±0.12	0.060
	7.329	11.6	1	0.36±0.08	0.113
	8.341	8.5	1	0.23±0.09	0.165
	8.347	11.6	1	0.74±0.16	0.185
	8.356	11.6	1	0.22±0.09	0.214
	8.426	11.6	1	0.63±0.10	0.446
	8.437	8.5	1	0.31±0.09	0.482

TABLE 4. 324 BAMBERGA, LIGHTCURVE DATA

Date 1969-70 U.T.		λ (μm)	Wt.	$E \cdot \Delta^2$ W $cm^{-2}\mu m^{-1}$ $\times 10^{-15}$	Fractional Period
Aug.	24.395	11.6	1	1.42±0.21	0.000
	24.399	10.5	1/2	1.04±0.12	0.312
	24.402	8.5	1	0.97±0.11	0.015
	25.403	10.5	1	1.29±0.19	0.033
	26.287	10.5	1	1.04±0.12	0.702
	26.348	11.6	1	1.37±0.32	0.897
	26.355	10.5	1	1.17±0.13	0.037
	26.360	8.5	1	1.21±0.17	0.877
	26.293	8.5	1	1.18±0.16	0.058
	26.402	10.5	1/2	1.20±0.14	0.912
	26.409	11.6	1/2	1.55±0.34	0.012
	27.412	11.6	1	1.11±0.09	0.077
Oct.	12.237	11.6	1	1.26±0.18	0.935
Dec.	1.189	11.6	1	1.30±0.30	0.204
	4.142	11.6	1	0.85±0.15	0.085

TABLE 5. VALUES USED IN DATA REDUCTION

(Tables 3 through 6)

NAME		U.T. DATE 1969/1970		Δ (A U)	r (A U)	Φ (Deg.)
(4)	VESTA	DEC	2.5	2.035	2.490	22.7
			4.5	2.011	2.487	22.2
		JAN	13.5	1.566	2.455	12.8
		FEB	7.4	1.452	2.433	2.0
			8.4	1.451	2.433	1.7
		APR	2.2	1.732	2.382	21.5
			3.2	1.742	2.381	21.7
			4.2	1.752	2.380	21.9
			5.2	1.762	2.379	22.1
(6)	HEBE	OCT	12.5	1.963	2.148	27.6
		DEC	4.4	1.491	2.264	19.2
		JAN	13.4	1.384	2.356	5.0
		FEB	7.3	1.525	2.404	12.6
			8.3	1.532	2.404	12.9
(7)	IRIS	AUG	23.5	1.145	1.954	23.5
			24.5	1.135	1.952	23.2
			25.5	1.126	1.950	22.8
			27.5	1.107	1.947	22.2
		SEPT	18.4	0.951	1.908	13.3
			19.4	0.946	1.907	12.9
		OCT	12.4	0.885	1.874	6.7

(continued on next page)

-continued-

TABLE 5. VALUES USED IN DATA REDUCTION

NAME		U.T. DATE 1969/1970		Δ (A U)	r (A U)	Φ (Deg.)
(7)	IRIS	DEC	1.2	1.036	1.836	27.0
			2.3	1.043	1.836	27.3
			3.2	1.051	1.836	27.5
			4.2	1.058	1.884	27.8
(324)	BAMBERGA					
		AUG	24.4	0.860	1.861	6.5
			25.4	0.856	1.858	6.0
			26.4	0.853	1.856	5.6
			27.4	0.850	1.854	5.1
		OCT	12.2	0.926	1.787	22.6
		DEC	1.2	1.326	1.786	32.8
			4.1	1.355	1.790	32.8

TABLE 6. ASTEROID PHOTOMETRY DATA

Date 1969/70 U.T.	λ (μm)	Wt.	$E \cdot \Delta^2$ W cm^{-2} μm^{-1} $\times 10^{-15}$	Δ (AU)	r (AU)	Φ (Deg.)	B(1,0) (Mag.)
(1) CERES							
69 Dec 4.1064	11.6	1	3.55±0.54	3.092	2.986	18.6	4.11
70 Jul 27.5049	11.6	1	3.20±0.96	2.747	2.919	20.3	
27.5150	8.5	1	3.20±0.47				
(2) PALLAS							
69 Aug 27.2278	11.6	1	0.43±0.24	2.323	3.297	6.5	5.18
69 Sep 18.1830	10.5	1/2	1.31±0.55	2.354	3.271	8.5	
18.1968	10.5	1	0.31±0.28				
19.1546	10.5	1	0.72±0.18				
19.1629	10.5	1	0.42±0.30				
19.1851	11.6	1/2	0.94±0.32				
19.1913	8.5	1	0.70±0.17	2.360	3.170	8.7	
70 Jul 25.3921	11.6	1	1.19±0.22				
25.4046	8.5	1	1.00±0.22	2.533			
25.4568	11.6	1	0.06±0.36				
25.4653	11.6	1	1.32±0.25				

(continued on next page)

- continued -

TABLE 6. ASTEROID PHOTOMETRY DATA

1969-70 U.T.	λ (μm)	Wt.	$E \cdot \Delta^2$ W cm^{-2} μm^{-1} × 10^{-15}	Δ (AU)	r (AU)	Φ (Deg.)	B (1,0) (Mag)
(2) PALLAS							
70 Jul 27.4099	11.6	1	1.29±0.23	2.513			
27.4362	11.6	1/2	1.47±0.28				
(3) JUNO							
69 Aug 27.2597	11.6	1	0.09±0.27	1.579	2.062	28.3	6.43
27.2611	11.6	1	1.08±0.32				
27.2659	11.6	1	0.11±0.35				
69 Oct 12.1417	11.6	1	0.10±0.32	2.856	2.866	20.1	
70 Jul 25.5071	11.6	1	1.67±0.30	2.980	2.094	10.9	
(5) ASTRAEA							
69 Dec 3.2650	11.6	1	0.12±0.08	1.443	2.395	8.2	8.00
(8) FLORA							
70 Apr 2.5245	11.6	1	0.17±0.24	1.745	2.544	16.5	7.48
(9) METIS							
70 Jul 26.1947	10.5	1	0.16±0.07	1.930	2.670	17.7	7.27
(15) EUNOMIA							
70 Apr 2.3442	11.6	1	0.18±0.14	2.105	3.035	8.3	6.29

(continued on next page)

- continued -

TABLE 6. ASTEROID PHOTOMETRY DATA

Date 1969-70 U.T.	λ (μm)	Wt.	$E \cdot \Delta^2$ W cm^{-2} μm^{-1} x 10^{-15}	Δ (AU)	r (AU)	Φ (Deg.)	B (1,0) (Mag)
(16) PSYCHE							
69 Aug 27.4225	11.6	1	0.06±0.13	1.772	2.696	10.7	6.89
(18) MELPOMENE							
70 Apr 5.5248	11.6	1	0.13±0.13	1.975	2.675	18.2	7.79
(19) FORTUNA							
70 Jul 27.3482	11.6	1	0.59±0.10	1.464	2.451	8.0	8.35
27.3685	8.5	1	0.36±0.07				8.35
(20) MASSALIA							
70 Apr 2.3585	11.6	1	0.15±0.09	1.359	2.362	1.3	7.48
4.3684	11.6	1	0.19±0.05	1.362	2.398	1.1	
(25) PHOCAEA							
69 Oct 12.4817	11.6	1	0.08±0.06	1.248	2.206	9.7	9.07
(27) EUTERPE							
70 Apr 5.4998	11.6	1	0.11±0.08	1.580	2.540	10.9	8.56
(39) LAETITIA							
69 Aug 25.5165	10.5	1/2	0.06±0.22	2.168	2.480	24.0	7.41
69 Oct 12.5246	11.6	1	0.19±0.23	1.688	2.512	15.8	
69 Dec 4.3176	11.6	1	0.25±0.07	1.644	2.558	10.0	

(continued on next page)

TABLE 6. - continued - ASTEROID PHOTOMETRY DATA

Date 1969-70 U.T.		λ (μm)	Wt.	$E \cdot \Delta^2$ W cm^{-2} μm^{-1} $\times 10^{-15}$	Δ (AU)	r (AU)	Φ (Deg.)	B (1,0) (Mag)
(39) LAETITIA								
69 Dec	4.3446	11.6	1	0.04±0.06				
70 Jan	13.1904	8.5	1	0.70±0.22	2.028	2.598	20.0	
	13.1973	8.5	1/2	0.27±0.14				
	13.2145	8.5	1/2	0.74±0.15				
	13.2374	8.5	1	0.35±0.07				
	13.2540	8.5	1/2	0.22±0.10				
	13.2723	8.5	1	0.04±0.29				
(44) NYSA								
70 Apr	2.4861	11.6	1	0.15±0.07	1.515	2.417	13.9	8.02
(68) LETO								
69 Oct	12.4401	11.6	1	0.22±0.06	1.316	2.311	2.5	8.29
(80) SAPPHO								
69 Sep	18.4676	10.5	1	0.12±0.02	0.882	1.837	14.1	9.29
	19.3797	10.5	1	0.10±0.02	0.882	1.837	14.1	
	19.3921	11.6	1/2	0.13±0.02				
69 Oct	12.2781	11.6	1/2	0.16±0.04				

(continued on next page)

TABLE 6. - continued - ASTEROID PHOTOMETRY DATA

Date 1969-70 U.T.	λ (μm)	Wt.	$E \cdot \Delta^2$ W $cm^{-2}\mu m^{-1}$ $\times 10^{-15}$	Δ (AU)	r (AU)	Φ (Deg.)	B (1,0) (Mag)
(145) ADEONA							
70 Jan 13.4376	8.5	1/2	0.30±0.04	1.339	2.291	7.8	8.93
70 Apr 2.2008	11.6	1	0.58±0.22	1.832	2.314	24.5	
3.1770	11.6	1	0.26±0.14	1.845	2.3148	24.6	
3.2130	11.6	1	0.29±0.13				
(163) ERIGONE							
70 Jan 13.3184	8.5	1	0.15±0.02	1.015	1.922	15.67	10.47
(192) NAUSIKAA							
70 Jul 26.4674	11.6	1	0.25±0.18	1.035	1.966	16.2	8.40
27.4912	11.6	1	0.26±0.07	1.028	1.964	15.7	
27.4679	11.6	1	0.22±0.05				
(313) CHALDAEA							
70 Apr 2.2808	11.6	1	0.08±0.04	1.025	2.021	17.0	9.69
2.3139	11.6	1	0.01±0.09				
3.3024	11.6	1	0.16±0.04	1.032	2.023	17.4	
(674) RACHELE							
70 Apr 5.2094	11.6	1	0.08±0.03				8.49

TABLE 7. (J3) GANYMEDE DATA

Date 1969-70	U.T.	λ (μm)	$E \cdot \Delta^2$ W cm^{-2} μm^{-1} × 10^{-15}	Wt.	θ Degrees	Δ (AU)
Jan	13.546	8.5	1.37±0.70	1	82.	5.558
	13.570	8.5	2.90±0.69	1	82.	5.558
	13.597	8.5	2.69±0.93	1/2	82.	5.558
Feb	7.478	11.6	14.6 ±3.4	1	258.	5.155
	7.578	11.6	10.7 ±1.4	1/2	258.	5.155
	8.505	8.5	2.41±0.50	1	305.	5.139
	8.512	11.6	9.0 ±1.6	1	305	5.139
Apr	2.426	11.6	6.3 ±2.1	1	140.	4.501
	3.344	11.6	9.2 ± 1.5	1	186.	4.496
	3.496	8.5	0.64±0.53	1	194.	4.496
	4.423	11.6	11.7 ±1.5	1/2	245.	4.490
	4.447	8.5	1.6 ±0.60	1	242.	4.490
	4.515	10.5	4.1 ±0.77	1/2	245.	4.490
	5.324	11.6	11.4 ±1.5	1	287.	4.484
	5.355	8.5	2.05±0.54	1	287.	4.484
	5.411	10.5	5.9 ±1.2	1	290.	4.484
	5.447	11.6	13.5 ±1.6	1	290.	4.484
Jul	28.176	11.6	8.9 ±1.5	1	210.	5.452
	28.189	11.6	5.3 ±1.5	1	210.	5.452
Mean		8.5	2.17±0.61			
		10.5	5.0±1.2			
		11.6	10.1±2.9			

TABLE 8. (J4) CALLISTO DATA

Date 1969-70	U.T.	λ (μm)	$E \cdot \Delta^2$ W cm^{-2} μm^{-1} $\times 10^{-15}$	Wt.	θ Degrees	Δ (AU)
Jan	13.532	8.5	3.08±0.69	1	292.	5.558
Feb	7.491	11.6	20.1 ±2.6	1	105.	5.139
	7.590	11.6	21.0 ±2.7	1	107.	5.139
Apr	2.459	11.6	15.1 ±3.6	1	212.	4.501
	3.359	11.6	17.5 ±2.8	1	231.	4.496
	3.506	8.5	5.50±1.1	1	234.	4.496
	4.422	11.6	17.5 ±2.2	1	256.	4.490
	4.430	8.5	2.55±0.64	1	254.	4.490
	4.518	10.5	9.1 ±1.3	1	256.	4.490
	5.315	11.6	18.2 ±2.1	1/2	275.	4.484
	5.384	8.5	1.6 ±0.4	1	275.	4.484
	5.433	10.5	7.9 ±1.5	1	276.	4.484
	5.459	11.6	16.3 ±2.0	1/2	276.	4.484
Jul	27.200	11.6	11.4 ±1.7	1	174.	5.437
	28.167	11.6	10.2 ±1.7	1	195.	5.452
Mean		8.5	32. ±1.7			
		10.5	8.50±0.84			
		11.6	16.4 ±3.6			

APPENDIX II. AN INFRARED ASTRONOMICAL PHOTOMETER FOR THREE COLOR OBSERVATIONS THROUGH THE 8-14μ ATMOSPHERIC WINDOW

Dennis L. Matson

Bruce C. Murray

Sol L. Giles, and

Gordon Hoover

INTRODUCTION

Astronomical instruments employed in the study of far-infrared radiation differ in important ways from equipment used to study visible light. This paper describes an astronomical photometer that was designed for observing in the 8-14 micron region of the spectrum. This instrument has been used for more than a year on the Mt. Wilson 0.61m and 1.52m (24-inch and 60-inch) telescopes of the Hale Observatories.

It is difficult to do accurate ground-based astronomical photometry at far-infrared wavelengths because of the severe constraints imposed by the Earth's environment. All observations must be made through "windows" in the atmosphere. These "windows", such as the one from 8 to 14 microns, are spectral regions where the extinction of extraterrestrial radiation is relatively small. If this extinction changes too quickly in time or varies spatially in an unexpected way (e.g. due to "clouds"), photometric work cannot be done.

The thermal radiation emitted by a room temperature blackbody is at a maximum near ten microns. Thus the structural members of the telescope, the photometer, and the other equipment emit a very large amount of thermal radiation. The photometer's optics must be designed so that radiation from these bright objects

does not reach the detector and swamp the signals from faint sources in space. The earth's atmosphere also emits an appreciable amount of energy at ten microns and special techniques are required to separate the extraterrestrial signals from this background. The magnitude and the variability of the atmospheric background radiation do not permit the successful operation of a conventional photometer with a single field of view. Modern instruments make a differential measurement between two fields of view. One field contains the object to be observed plus the radiation from the atmosphere and the other field contains only atmospheric radiation. Typically the two fields of view are compared and the differences are measured many times a second. The first modern semiconductor-detector photometer was built and described by Westphal et al in 1963.[1] Since that time, a number of other instruments have been built and their descriptions and other information can be found in the literature.[2-5] Of particular interest is Low's discussion of special purpose infrared telescopes.[5] Compared to photomultiplier tubes, all present far-infrared detectors have poor signal to noise ratios and they must be used at cryogenic temperatures.

THE PHOTOMETER

The mechanical structure of the photometer is basically a sturdy skeleton frame to which modular parts, holding the various optical elements, are fastened by built-in clamps. This design was used so that maintenance and testing at the telescope could be carried out with a minimum of effort.

The instrument uses a single detector which alternately views two different fields in the plane of the sky. The switching from one field to the other is done by means of a rotary optical chopper (as shown in Fig. 1). By chopping at a rate of 30 Hz the photometer alternately samples and compares light from two separate parts of the telescope's focal plane. Converging f/16 light from the telescope is brought to focus at the photometer's entrance aperture. Because the two incoming beams have different optical lengths their resulting focal planes are not the same, but the focus of an f/16 beam on a large telescope has enough depth that compensation is not necessary when the path difference is only a few millimeters.

The focal plane aperture is situated inside the vacuum vessel of the dewar that holds the liquid hydrogen coolant. The aperture is inclined at forty-five degrees to the optical axis. A combined dichroic plate and long-wavelength-pass filter is attached to its front surface. At the dichroic plate, rays of visible light are reflected and

exit the vessel through a window where they reach an observer with an eyepiece, who sees a real image of the star to use for guiding. A thin, aluminized, microscope-slide cover slip with a hole in it is fastened just in front of the filter and indicates the position of the true aperture. Infrared radiation with wavelengths longer than about 7.5μ passes through both the blocking filter and the aperture and on to a wheel which places filters, one at a time, in the optical path to obtain the three narrow bandpasses. A fourth position in the filter wheel has no filter, and allows 8-14μ wideband photometry. The filter wheel and its detent (for precise, repeatable positioning of the wheel) are operated through the wall of the vacuum vessel by two pairs of magnets. A KRS-5 lens behind the filter wheel forms the bundle of diverging rays into an image of the primary mirror of the telescope. As the distance between this lens and the entrance aperture is increased, more of the stray rays (in this case rays diverging faster than f/16) tend not to reach the lens. This is only a precautionary measure and is not the chief means for rejecting off-axis rays. The maximum permissible distance is fixed by the diameters of the aperture and the KRS-5 lens. The requirement to form a real image of the primary mirror on the detector determines the focal length of the lens and the permissible amount of aberration gives the focal ratio, thus

fixing the lens diameter.

A pupil immediately in front of the detector allows only the geometric rays from the image of the primary mirror to reach the detector. All parts of the image (except for focused starlight, if it passes through the center of the photometer's aperture) are blurred by diffraction due to the entrance aperture. To eliminate diffracted thermal radiation from the primary mirror supports, part of the light near the perimeter of that mirror's image must be discarded. If the photometer's aperture were smaller, diffraction effects would be greater and it would be necessary to make the pupil smaller. Correspondingly more starlight would be rejected. The size of this pupil is the primary means of rejecting off-axis rays and adjusting the angular response of the instrument.

The detector is housed in a gold-plated, highly reflective cavity immediately behind the pupil. This cavity intercepts light which passes entirely through the detector and reflects it back for another pass. The detector is a 2 x 2 millimeter crystal of mercury-doped germanium (Ge:Hg). Indium solder fastens the crystal to a copper heat sink (not shown in Fig. 1). Heat flowing from this fitting reaches the liquid hydrogen reservoir and is removed by evaporation. Should the power absorbed by the detector or its immediate environment be too great, the temperature of the crystal will rise, its responsivity and impedance will

change, and the response of the system will no longer be linear. This effect must be kept in mind when measuring sources of large irradiance and also when comparing faint sources observed under different background conditions.

The angular response of the detector and the optics inside the dewar was measured by placing a test source of chopped thermal radiation at numerous locations in the field of view. The contoured response is displayed in Fig. (2).

Fig. (3) shows the normalized instrumental response as a function of wavelength. This response was obtained using the measured spectral transmission data for each filter, published spectral transmission curves for the other optical elements, and published spectral response curves for Ge:Hg photoconductors. The overall response of the photometer to an extraterrestrial source of radiation depends both upon the intrinsic spectral response of the instrument and the instantaneous transmission spectrum of the atmosphere. Advantage can be gained by using bandpasses that avoid the major absorption features. The lack of detector response beyond about 13.5μ provides the long-wavelength cut-off for the instrument.

The photometer was tested in the laboratory for light leakage by comparing the theoretical responses to the responses

observed for fields of view at several different temperatures but at approximately a constant level of illumination in the visible. Additional leakage tests were performed at the telescope by observing the response to bright, early-type stars which emit very little energy at ten microns. Within experimental error, neither type of test detected a light leak. The photometer's aperture was also checked at the telescope. By trailing a bright infrared star along a raster pattern it was found that the central part of the aperture gave a uniform response to within the testing precision of a few percent.

Mechanical tests were made to verify that the optical elements of the photometer did not shift significantly with respect to each other. This was done by applying static loads to the various structural parts in generous excess of what they would experience at the telescope.

Extreme care must be taken when setting up any far-infrared astronomical equipment because these instruments receive thermal radiation from the telescope and the atmosphere, as well as from any extraterrestrial source to be observed. For example, if the photometer shifts position as the telescope is moved from one setting to another, a spurious signal will result which originates totally within the equipment. In setting up the photometer the beam pattern from the optical chopper is centered on the secondary mirror of the telescope and then

the fixed mirror is set coplanar with the chopper. The photometer and all optical elements in it are then checked to make sure that each is held rigidly and is in its proper position.

ELECTRONICS

As shown in Figs. (4) and (5) the modulated optical beam induces a variation in the number of charge carriers in the Ge:Hg photoconductor. This variation causes a fluctuation in the bias current which produces a voltage variation across the load resistor, R_L. The voltage of the signal at point 1, as shown in Fig. (5), is preamplified at the photometer and sent by cable to an electronics rack where the signal is amplified and demodulated synchronously with respect to the phase of the chopper.

The angular position of the optical chopper is determined when its rotating blades interrupt a small beam of light that is directed at a photoresistor. The voltage across the photoresistor is amplified and used to operate the demodulator as well as to control a relay which briefly grounds the input of the amplifier whenever an edge of the optical chopper's blades passes through the detector's field of view. This latter process is necessary because thermal radiation emitted from "warm" parts of the photometer is scattered into the detector by the edge of each blade. Electrical signals at several locations in the circuit are displayed in Fig. (5). The electronic

switching of the demodulator leads the mechanical switching of the relay, but the amount of electrical signal confusion is negligible.

The synchronous demodulator converts the ac output signal from the amplifier to a dc voltage which is fed into a voltage-to-pulse-frequency converter. The generated pulses are counted over a fixed time interval by an electronic counter and after the end of each interval a printer prints the total on a paper tape. The output of the amplifier is continuously monitored by an oscilloscope, and a strip chart recorder continuously plots the output from the demodulator. These monitors are extremely useful for detecting irregularities during observations.

In the operation of this equipment on Mt. Wilson, a considerable amount of effort was required to eliminate the electrical interference from numerous nearby radio and television stations. This was necessary because the locations and amplitudes of standing radio frequency waves on the equipment changed with time and with each setting of the telescope. Long signal cables were particularly vulnerable and in this particular case satisfactory results were obtained only after careful attention was paid to adjusting the lengths of the cable shields in an attempt to use the dominant standing waves on one shield to cancel those on the other shield.

Empirically it was found that a detector bias voltage of six and one half volts yields the best signal to noise ratio. This voltage was determined under actual observing conditions on Mt. Wilson using Mars as a test object. The bias voltage and other properties vary greatly between individual detectors.[1,3]

RESULTS

Some sample strip chart traces made with this equipment are shown in Fig. (6) and (7). Two different observational techniques were used and both are explained in the captions.

The noise seen in these traces is from several types of sources found (1) in the telescope-photometer combination, (2) in the earth's atmosphere, and (3) in the Ge:Hg detector. The noise in the telescope-photometer system can be due to several effects. Because surfaces of the optical chopper blades are not exactly coplanar each blade projects the beam pattern, Fig. (2), in a slightly different direction and the resulting composite pattern cannot be perfectly matched by single pattern projected off the fixed mirror. Thus cancellation of radiation emitted by the telescope is imperfect. When the amount of thermal radiation from the telescope varies, perhaps due to a slight change of the surface temperature of a structural member, a deflection can result on the

strip chart. Other things being held constant, the actual signal voltage, and thus the pen position, is a function of the algebraic sum of all errors in matching the patterns of beams 1 and 2. Different effects arise because the two incoming beams diverge continuously from the primary mirror of the telescope, where they are coincident, to the optical chopper, where they are completely separated. First, the optical through-put of the two beams is not equal because they are not reflected by the identical mirror surfaces and because the chopper spreads the beam pattern. If the level of the atmospheric background radiation changes a deflection will result on the strip chart due to the difference in optical through-put between the two beams. The second effect is the very small variation that arises from differences in thermal emission from the optical surfaces that are not common to both beams. In practice, this effect is made negligible by keeping the mirror coatings fresh.

Another type of noise has its origin in the atmosphere. Fig. (7) illustrates noise due to small changes in the extinction of radiation from Mars. The correction of observations for the effects of extinction is a difficult problem and will be taken up in future articles about observations made with this photometer.

As one might suspect, the background radiation from the atmosphere is neither uniform in time nor space. When the amount of radiation received by one beam changes with respect to that received by the other, a "noise" signal is produced. When irregular clouds pass through the beams this effect is very large. One can easily find the locus of points in the atmosphere where the photometer is sensitive. By retracing all the rays that reach the detector the locus for the 1.52m (60-inch) telescope is found to be two diverging frusta, one corresponding to each beam. Both apex angles are 17.8 seconds of arc, a value governed by field and the first minimum of the Airy disk. The frusta have a common truncation at the telescope's primary mirror and their axes diverge at an angle of one minute of arc. At an altitude of 9,200m (7,450m plus the height of Mt. Wilson) the frusta cease to overlap. At this height they have a diameter of approximately 2.1 meters. Thus this atmospheric noise is caused by spatial emission differences separated horizontally by only about a meter. Vertically, however, the noise can originate anywhere from just outside the dome to very high in the atmosphere.

At the telescope the detector noise was estimated to be, typically, one third to one fourth of the total noise level on an average night. This estimate was made on several occasions by noting

the noise level when a piece of cardboard was placed between the chopper and the entrance aperture. For discussions of noise in photoconductors the reader is referred to the literature.[6-8]

By using the dichroic plate in the aperture assembly, the precision with which images (that are bright enough for guiding) can be centered is independent of the object's stellar magnitude. A 2mm diameter entrance aperture was chosen so that at the Cassegrain focus of the Mt. Wilson 1.52m (60-inch) telescope, the aperture would geometrically subtend about 16 seconds of arc on the sky. Using Rayleigh's criterion for the 1.52m (60-inch) mirror, diffraction at 12μ is 1.8 seconds of arc. Thus, for a point source the effective infrared aperture subtends about 14 seconds of arc. On the other hand, it is possible for some background atmospheric radiation from a 19 second of arc field to also reach the detector.

"Seeing" typically spreads the image of a star by one to four seconds of arc. Precise centering and the aperture's large size contribute to minimizing the photometric errors due to this effect.

This instrument has been used successfully for more than a year on Mt. Wilson at the 0.61m and 1.52m (24-inch and 60-inch) telescopes of the Hale Observatory. Asteroids and some bright stars were observed. Results of these two observational programs will be discussed in articles appearing elsewhere. Observing with the method

described in the caption for Fig. (6) signals have been integrated for times much longer than those illustrated here by the strip chart traces. Obtaining bias free measurements for astronomical sources is observationally difficult and tricky and will be discussed in a subsequent paper.

Acknowledgments

We thank James Westphal, Frank Low and Eric Becklin for many helpful discussions at various stages of this project. Victor Nenow and DeVere Smith advised and helped us with the electronic problems. George Jones helped in the construction and the extended field testing of the photometer. We thank Barton Instruments for the gift of a fine set of vacuum bellows and the staff of the Santa Barbara Research Center for assistance concerning detectors.

This work was supported by the National Aeronautics and Space Administration Grant NGL 05-002-003.

REFERENCES

1. J.A. Westphal, B.C. Murray, and D.E. Martz, Appl. Opt. 2, 749 (1963)

2. F.J. Low and H.L. Johnson, Ap. J. 139, 1130 (1964)

3. J.M. Saari and R.W. Shorthill, Isothermal and Isophotic Atlas of the Moon (NASA CR-885, 1967)

4. F.C. Gillett, F.J. Low and W.A. Stein, Ap. J. 154, 677 (1968)

5. F.J. Low, Science 164, 501 (1969)

6. P.W. Kruse, L.D. McGlauchlin, and R.B. McQuistan, Elements of Infrared Technology: Generation, Transmission, and Detection (John Wiley and Sons, Inc., New York, 1962)

7. R.A. Smith, F.E. Jones, and R.P. Chasmar, The Detection and Measurement of Infrared Radiation (The University Press, Oxford, 1957)

8. W.L. Wolf, Ed., Handbook of Military Infrared Technology (Office of Naval Research, Department of the Navy, Washington D.C., 1965)

9. A.F.H. Goetz, Infrared 8-13 Spectroscopy of the Moon and Some Cold Silicate Powders (Ph.D. thesis, California Institute of Technology, 1967).

CAPTIONS

Figure 1

A cutaway and slightly exploded view of the optical elements in the photometer. The coverslip and everything above it are cooled by the liquid hydrogen. The bandpass filter is one of the three filters mounted in a cold filter wheel. Black Nextel velvet coating (Minnesota Mining and Manufacturing Co.) paint was used inside the dewar's optical train to absorb scattered light.

Figure 2

Beam pattern of the detector and optics inside the dewar. The contours show the normalized response as a function of angular position in the field of view. The maximum response was used for the normalization. The width of the pattern is determined chiefly by the size of the pupil in front of the detector.

Figure 3

The relative laboratory spectral response of the instrument and the relative transmission of the 8-14μ window as measured by Goetz[9]. The atmospheric transmission depends on weather conditions including smog. Thus at any given time the relative spectral

response of the photometer to an extraterrestrial source is determined by the relative laboratory response spectrum and the instantaneous atmospheric spectrum. However, shifts in effective wavelengths are in fact small. The filter bandpasses are normalized to the detector's response at 10μ. The difference from unity is due to absorption and other losses in the optics. The 8-14μ bandpass (BP1, not shown) is essentially the atmospheric spectrum shown above. Resolution is about 0.08μ.

Figure 4

Functional diagram of the electronics. The Ge:Hg photoconductor is inside the dewar and is at a temperature of about 20°K. The circuits in the photometer are connected to an electronics rack near the telescope by the "transmission lines." The circled numbers refer the reader to wave forms in Fig. (5).

Figure 5

Sketch of the ideal (no noise) waveforms at locations numbered in Fig. (4). The top line represents the response when radiation from an infrared bright star arrives via beam 1. The spikes occur when radiation from within the photometer is scattered to the detector from the edges of the chopper blades. The bottom line shows this same

signal (at a different vertical scale) as seen on the monitor oscilloscope. By this stage the spikes have been discarded and the signal is ready for the synchronous demodulator.

Figure 6

Traces of strip chart records obtained at the Mt. Wilson 1.52m (60-inch) telescope. The recorder plots beam 1 minus beam 2. First the object is placed in beam 1 giving a (+) deflection. After the count is printed the object is placed in beam 2, giving a (-) deflection. One peak-to-peak deflection is a measurement. Instrumental constants must be included in any color ratio, thus the fact that the α Orionis trace for Bandpass No. 3 is of less amplitude does not mean that the star is fainter at that bandpass. This method of observing was introduced by Low.

Figure 7

Strip chart trace for Mars as seen at the 0.61m (24-inch) telescope. The observational technique here differs from the one used in Fig. (6). First Mars is placed in beam 1 and a count is taken. After the count is printed Mars is moved out and another count is taken with both beams on the sky. The relative units used in this figure are the same as those used in Fig. (6). The insert shows

the effect of atmospheric extinction (as seen with a 0.5 sec time constant) compared with the noise when both beams are on the sky.

Fig. 1

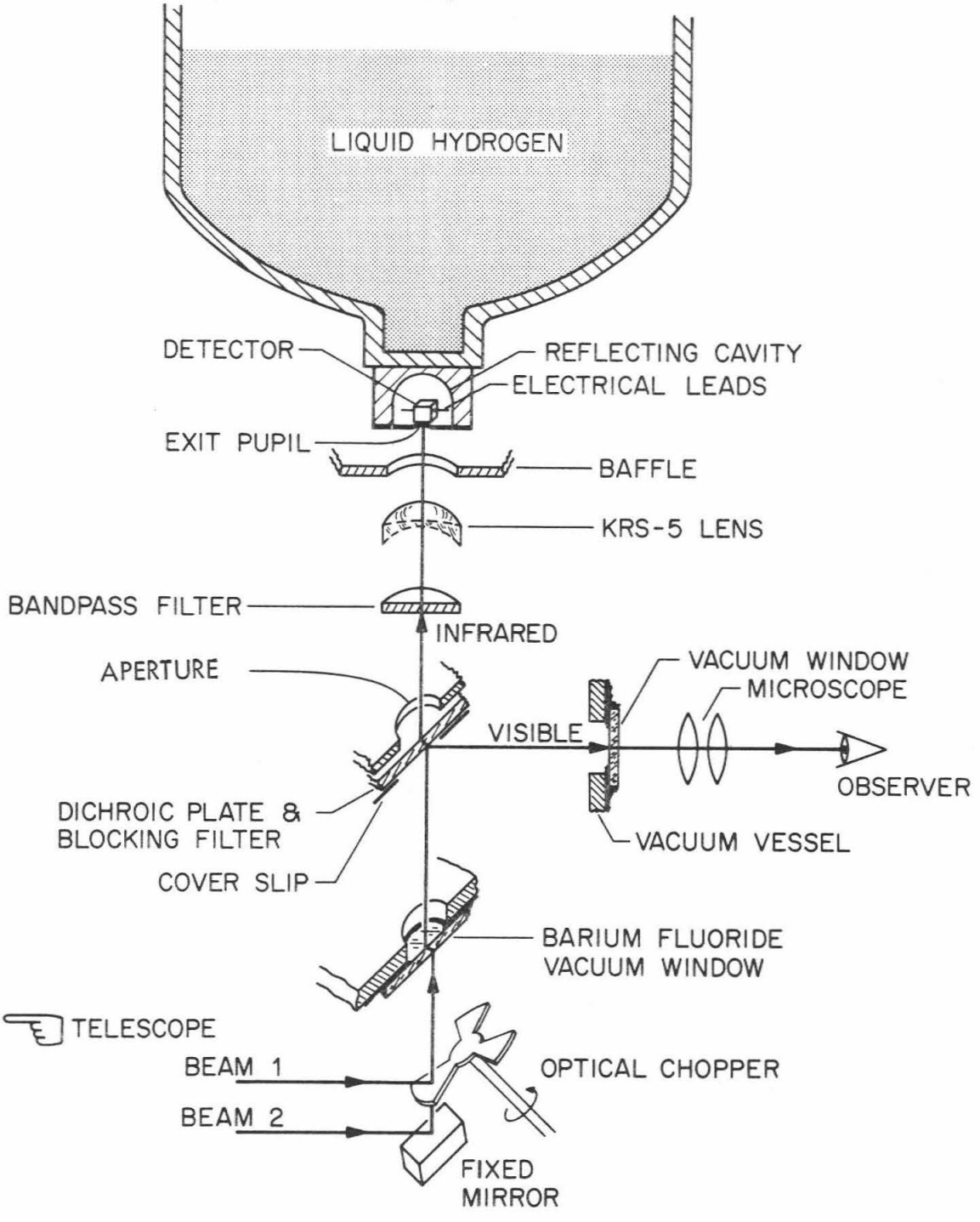
LIQUID HYDROGEN
DETECTOR
REFLECTING CAVITY
ELECTRICAL LEADS
EXIT PUPIL
BAFFLE
KRS-5 LENS
BANDPASS FILTER
INFRARED
APERTURE
VACUUM WINDOW
MICROSCOPE
VISIBLE
OBSERVER
DICHROIC PLATE &
BLOCKING FILTER
VACUUM VESSEL
COVER SLIP
BARIUM FLUORIDE
VACUUM WINDOW
TELESCOPE
BEAM 1
OPTICAL CHOPPER
BEAM 2
FIXED
MIRROR

Fig. 2

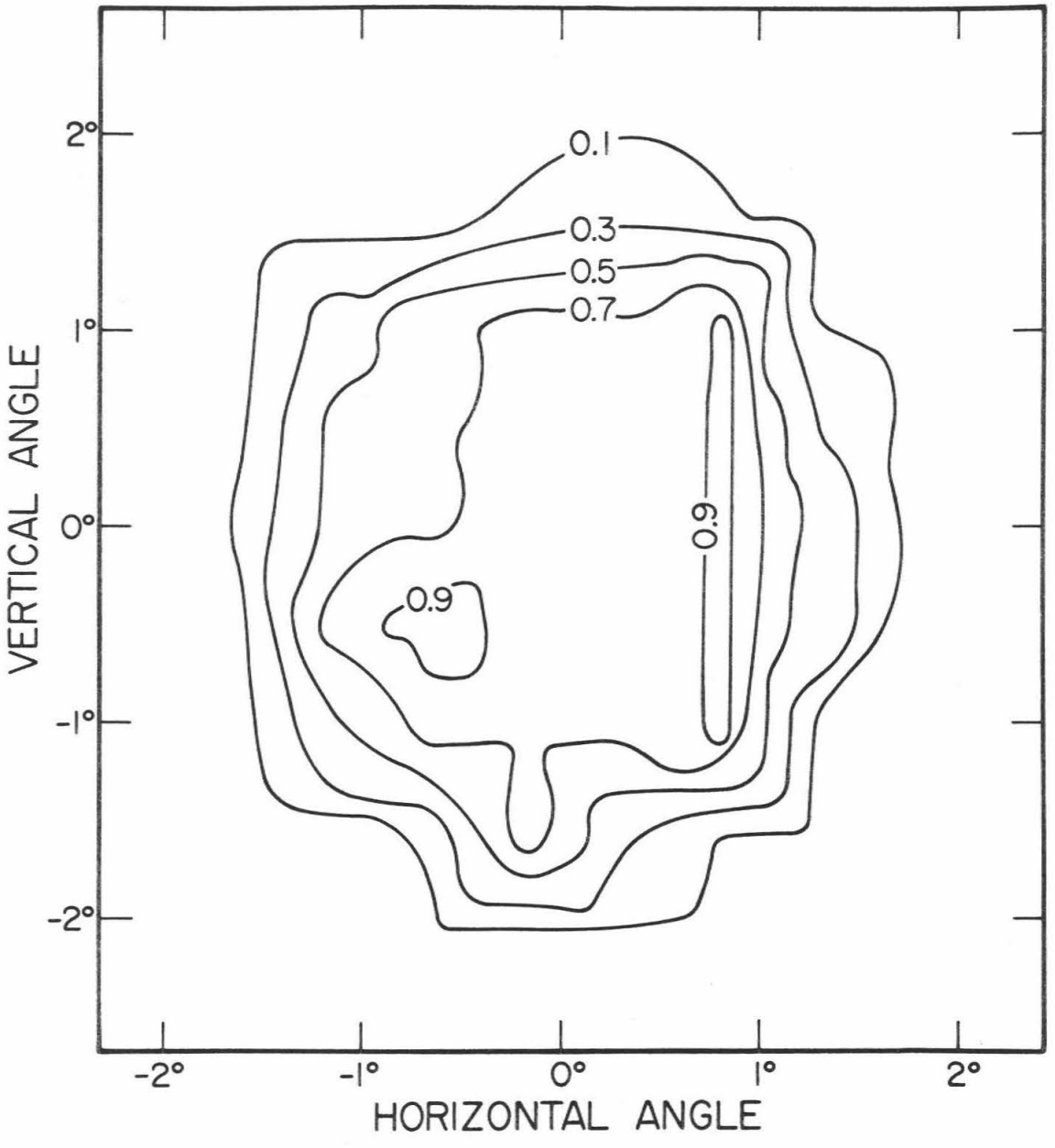
0.1
0.3
0.5
0.7
0.9
0.9
2°
1°
0°
-1°
-2°
VERTICAL ANGLE
-2°
-1°
0°
1°
2°
HORIZONTAL ANGLE

Fig. 3

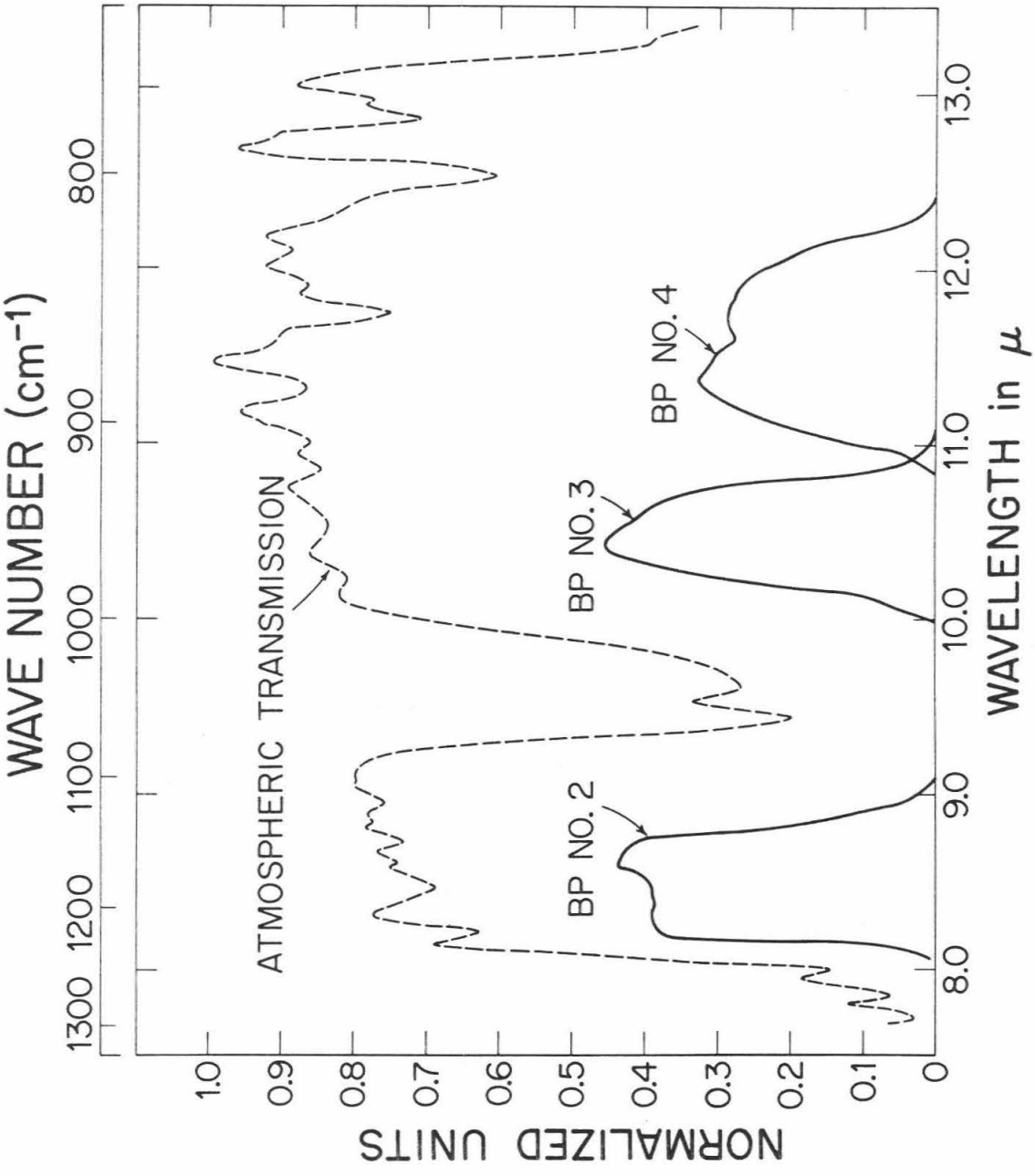
WAVE NUMBER (cm⁻¹)
1300 1200 1100 1000 900 800
WAVELENGTH in μ
8.0 9.0 10.0 11.0 12.0 13.0
NORMALIZED UNITS
0 0.1 0.2 0.3 0.4 0.5 0.6 0.7 0.8 0.9 1.0
ATMOSPHERIC TRANSMISSION
BP NO. 2
BP NO. 3
BP NO. 4

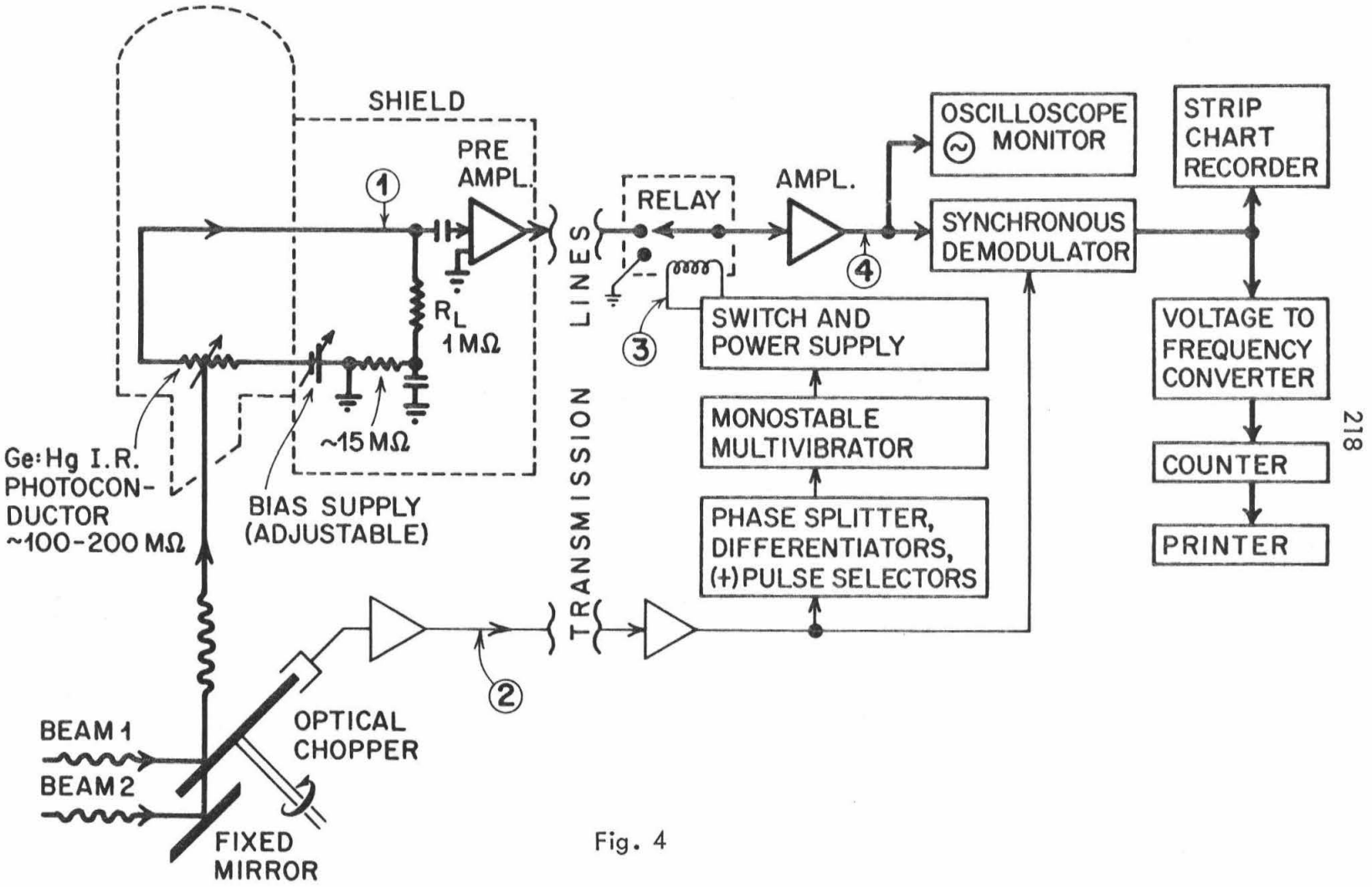
SHIELD
PRE AMPL.
1
R_L 1 MΩ
~15 MΩ
Ge:Hg I.R. PHOTOCONDUCTOR ~100-200 MΩ
BIAS SUPPLY (ADJUSTABLE)
BEAM 1
BEAM 2
OPTICAL CHOPPER
FIXED MIRROR
2
TRANSMISSION LINES
RELAY
3
AMPL.
4
OSCILLOSCOPE MONITOR
SYNCHRONOUS DEMODULATOR
SWITCH AND POWER SUPPLY
MONOSTABLE MULTIVIBRATOR
PHASE SPLITTER, DIFFERENTIATORS, (+)PULSE SELECTORS
STRIP CHART RECORDER
VOLTAGE TO FREQUENCY CONVERTER
COUNTER
PRINTER

Fig. 4

Fig. 5

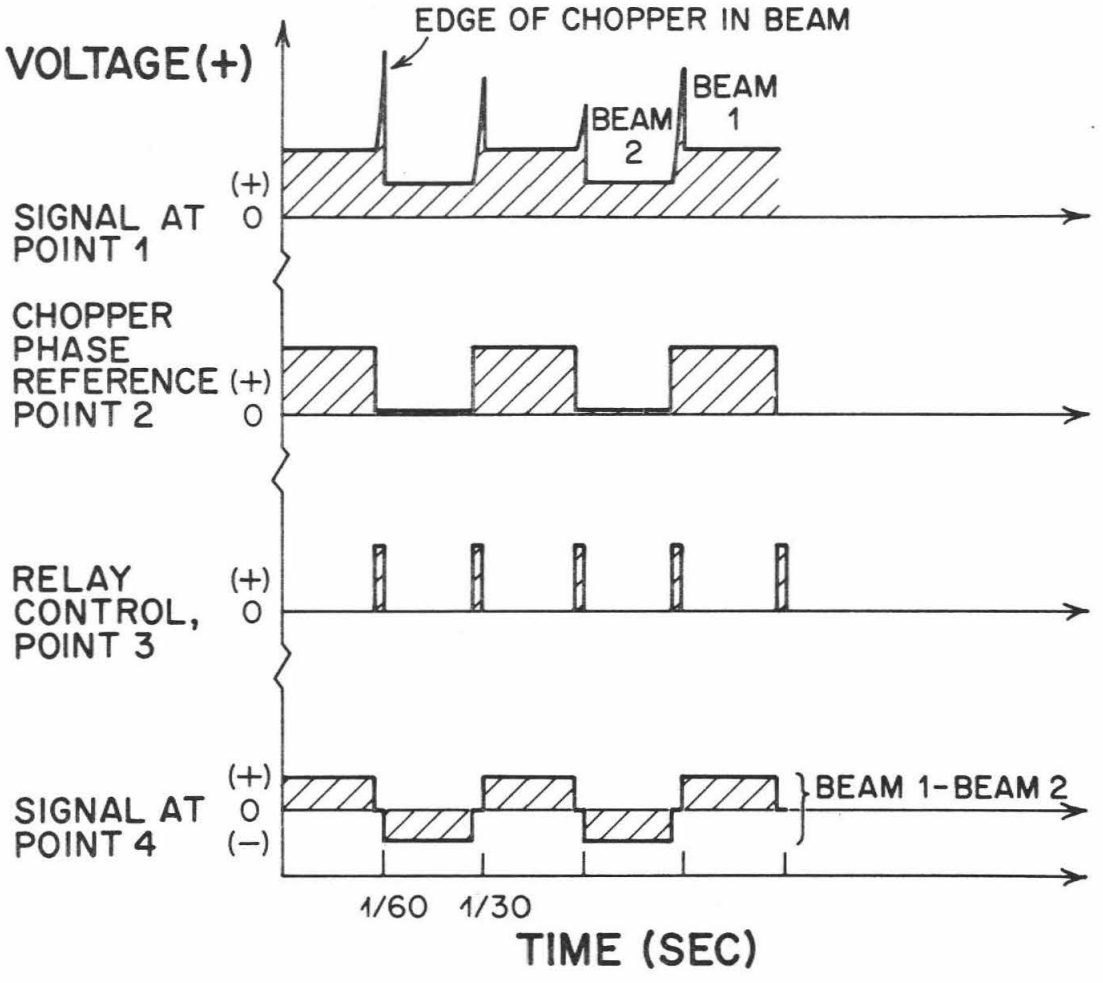
EDGE OF CHOPPER IN BEAM
VOLTAGE(+)
BEAM 2
BEAM 1
(+)
0
SIGNAL AT POINT 1
CHOPPER PHASE REFERENCE POINT 2
(+)
0
RELAY CONTROL, POINT 3
(+)
0
SIGNAL AT POINT 4
(+)
0
(−)
BEAM 1-BEAM 2
1/60
1/30
TIME (SEC)

Fig. 6

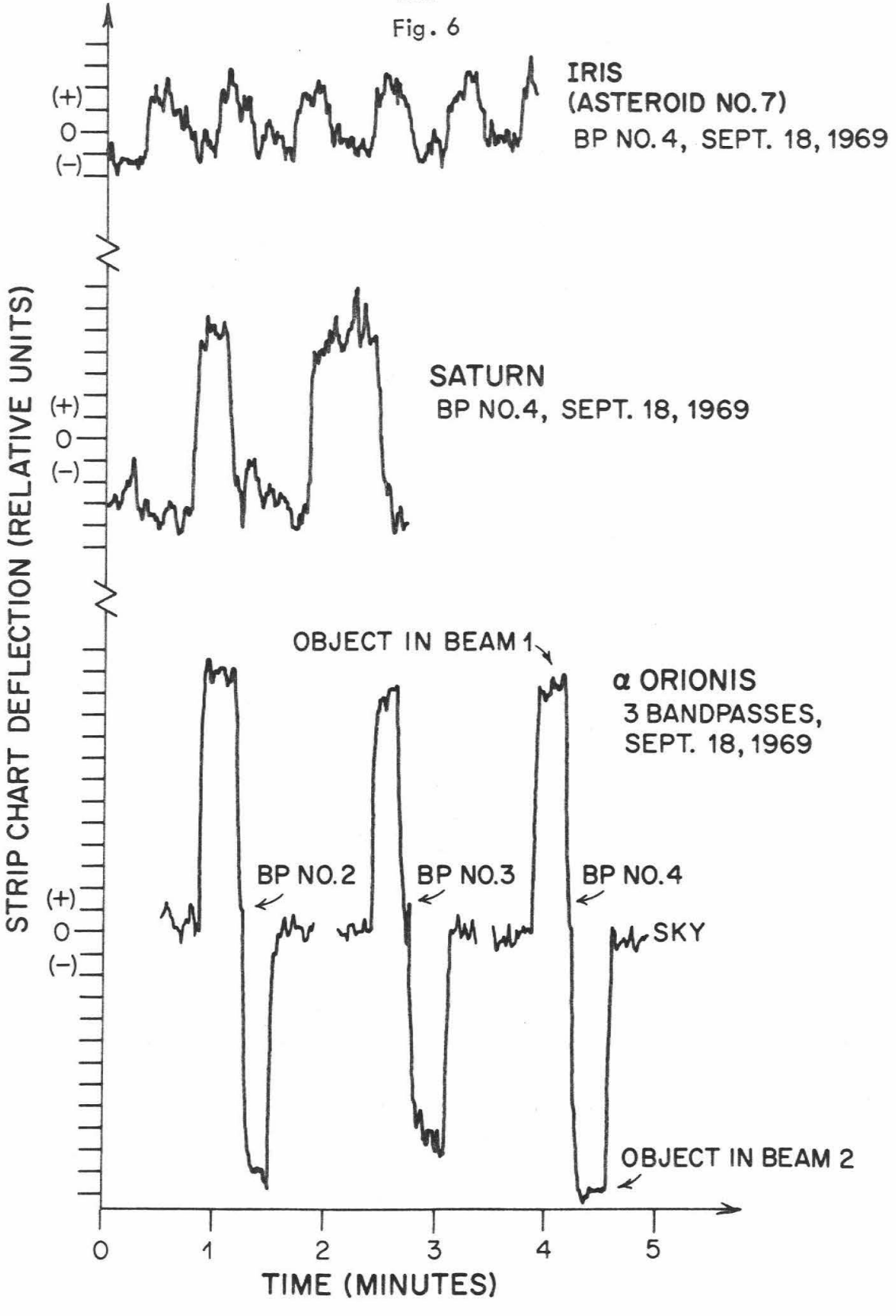
IRIS
(ASTEROID NO. 7)
BP NO. 4, SEPT. 18, 1969
SATURN
BP NO. 4, SEPT. 18, 1969
OBJECT IN BEAM 1
α ORIONIS
3 BANDPASSES,
SEPT. 18, 1969
BP NO. 2
BP NO. 3
BP NO. 4
SKY
OBJECT IN BEAM 2
(+)
0
(−)
STRIP CHART DEFLECTION (RELATIVE UNITS)
0
1
2
3
4
5
TIME (MINUTES)

Fig. 7

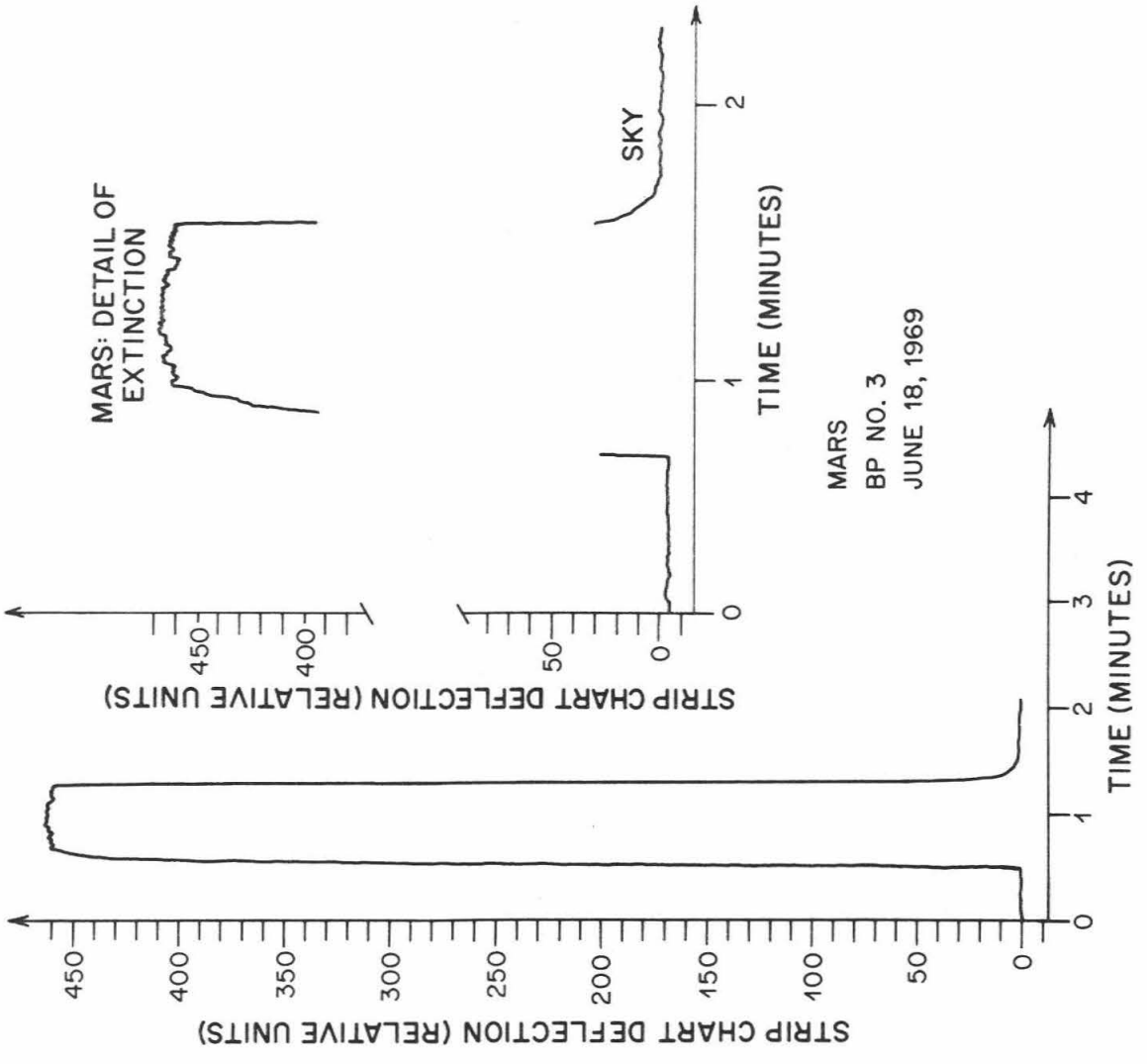
STRIP CHART DEFLECTION (RELATIVE UNITS)
450
400
350
300
250
200
150
100
50
0
0
1
2
3
4
TIME (MINUTES)
MARS
BP NO. 3
JUNE 18, 1969
STRIP CHART DEFLECTION (RELATIVE UNITS)
450
400
50
0
SKY
0
1
2
TIME (MINUTES)
MARS: DETAIL OF EXTINCTION

APPENDIX III

INFRARED OBSERVATIONS OF ASTEROIDS

by

Dennis L. Matson

Presented at the
Twelfth Colloquium of the International Astronomical Union
"Physical Studies of Minor Planets"
8, 9, 10 March 1971
Tucson, Arizona

This paper is a brief, preliminary report about a program of reconnaissance photometry designed to study the thermal radiation emitted from asteroids. Observations of thermal radiation, and their subsequent interpretation, can provide new knowledge that presently cannot be gained by any other method. The emitted thermal power is by and large that portion of the insolation which is absorbed. Part of the asteroid's emission spectrum can be observed through windows in the Earth's atmosphere. With the aid of models for the details of energy transfer at the asteroid's surface, and accurate visible photometry, reliable estimates can be made for some of the important parameters in the models. Of particular interest are Bond albedo, size, emissivity, and thermal inertia.

Infrared observations were made through bandpasses centered at 8.5, 10.5, and 11.6 μm ($\Delta\lambda$=0.5, 0.5, and 1.0 μm, respectively). The observations were made from July 21, 1969, to July 27, 1970, using the Hale Observatories' 1.52 m telescope at Mt. Wilson. A total of 26 objects was observed: 1 Ceres, 2 Pallas, 3 Juno, 4 Vesta, 5 Astraea, 6 Hebe, 7 Iris, 8 Flora, 9 Metis, 15 Eunomia, 16 Psyche, 18 Melpomene, 19 Fortuna, 20 Massalia, 25 Phocaea, 27 Euterpe, 39 Laetitia, 44 Nysa, 68 Leto, 80 Sappho, 145 Adeona, 163 Erigone, 192 Nausikaa, 313 Chaldaea, 324 Bamberga, and 674 Rachele. Most of the program asteroids were observed through the 11.6μm bandpass, and bright objects were measured at all three wavelengths. The observational coverage varies from good for the bright objects, which were observed at a number of phase angles, to poor for those asteroids observed only once.

Phase data for 4 Vesta and 7 Iris are shown in Fig. 1 and Fig. 2. Each point represents the weighted nightly mean. The curve in each of these figures is the average using both the 4 Vesta and 7 Iris data. This curve is used to correct all the 11.6 μm thermal emission observations to zero phase angle. For any given angle, the phase variation is a function of the temperature distribution, which in turn is a function of the thermal properties of the asteroidal surface, the orbit, the rotational period, and the aspect geometry. The regions on each side of opposition where the phase angle is large are the two most important critical regions for testing thermal models. Under the proper circumstances, additional critical regions can be provided by aspect differences from one opposition to another.

The ordinate on the phase plots is calibrated by the assumption that α-Bootis has a flux per unit area at the Earth of 4.1, 1.8, and 1.2×10^{-15} W cm^{-2} μm^{-1} for 8.5, 10.5, and 11.6 μm, respectively. The accuracy of this calibration is not known. The calibrations currently for use in the 8 to 14μm region have a range of about 20 percent.

All measurements reported here were made with respect to three new stellar photometry systems that were established from observations obtained concurrently with the asteroid program and using the same equipment (Matson, 1971).

The scatter shown by the 7 Iris data is due to the lightcurve variation of that asteroid. In fact, enough data are available to construct a composit

lightcurve of the thermal emission at 10.5 μm. Correlation of these data with the phase of the visible lightcurve will enable one to differentiate between a spotted asteroid and an irregularly shaped object. This can also be accomplished with the infrared data alone by using observations from two bandpasses to obtain the color temperature as a function of the rotational phase angle. For this method the propagation of observational errors is not as favorable as when using the visible and infrared data.

The error bars on the two phase variation plots represent the propagation of all random and nominal errors incurred in transferring the asteroid observation to α-Bootis. The bounds are intended to delimit the region where the probability of the "true value" is two-thirds or greater.

Table I tabulates some simple models that have been used to analyze the same 4 Vesta data. The parameters, as it can be seen, vary as the model is changed. The common assumption of the models in Table I is that each elemental area on the surface radiates like a blackbody. Phase effects, other than for the corrections applied to the observational data, have been ignored. The albedo parameter has been assumed to be independent of wavelength. This parameter is a weighted average over the solar spectrum. The weight is the amount of energy absorbed at each wavelength.

The albedos provided by the models are surprisingly low and the corresponding sizes are large compared to disk measurements. The models and the

absolute calibration of the photometry have a systematic error of unknown size and it is premature to assume that the albedo anomaly is due to some unexpected property of asteroidal surfaces. Currently, detailed thermal models that take rotation and the direction of the pole into account are being examined. The simple models (Table I) err chiefly in their treatment of the infrared phase integral and are used only for a differential comparison of the data.

Table I shows that the changes in parameters from model to model are small enough that it is safe to draw some conclusions at this time. For this purpose, the "rough," nonrotating sphere model is employed because it represents the Moon better than the other two. Normalization to 4 Vesta enables a differential comparison to be made between asteroids. The arbitrary normalization is set at 210 km radius and 0.3 albedo. In this way systematic errors from many diverse sources are mitigated, but other errors are introduced. For example, error from the visible phase integral q for 4 Vesta is introduced if the result is interpreted as the Bond albedo. The 11.6 μm infrared data are corrected to zero phase angle and the visible data, B(1,0) are taken from Gehrels (1970). The resulting model radius and model albedo are plotted in Fig. 3.

The first things to note are the infrared points for 1 Ceres and 2 Pallas. Already they are in reasonable agreement with published data. Part of the difference is the result of the adopted normalization and the model.

The asteroids vary in the albedo parameter from about 0.03 for 324 Bamberga to about 0.3 for several objects. 324 Bamberga is extremely dark. Presently it is the darkest member of a group of large, dark asteroids. By contrast, 4 Vesta appears to be unique — the only known large, light-colored asteroid. Objects of comparable albedo are not encountered until the 50 to 90 km radius interval is reached. Type I bias is the discrimination against small, dark asteroids. 313 Chaldaea was obtained near the end of the program when a small number of objects that were thought to be too faint for detection were observed. Considering this bias, it seems likely that there exist small, dark asteroids comparable in size and albedo to Phobos. Infrared observations of Phobos are extremely important. This control point will help to remove distortion in the radius and albedo scales due to differences in surface morphology between large and small asteroids.

At the other extreme of the albedo range is type II bias. Here objects are unduly favored by observational selection. It is surprising that more of them were not discovered. This implies that they are not particularly abundant in the time and space regions sampled.

At this time 20 Massalia and 39 Laetitia are the asteroids with the highest albedo. Their data are dispersed because of their lightcurves. In this reduction, their albedo is in the same class as 4 Vesta and perhaps J3, using Johnson's (1970) lunar-model values for the Bond albedo.

For the large bodies without atmospheres, the trend in the inner part of the solar system is one of low albedo. The Moon, Mercury, and perhaps J4 can be thought of as part of a branch of large, dark objects. The light objects appear to be singular with no trend except for the sheer size of the Galilean satellites of Jupiter. At a radius of about 100 km the dark asteroids continue but they are now joined by objects with higher albedos.

Considering the errors in the model and in the data, it would be risky to draw conclusions about any of the smaller features of Fig. 3.

Infrared observations also have other applications that are not related to the main thrust of this project. For example, they can aid in the study of rotating asteroids. Consider a rotating, spherical asteroid with an absolutely uniform albedo. Fig. 4 shows how the visible and infrared fluxes will be related. Before opposition, warm material is still seen after it crosses the evening terminator. After opposition, the morning terminator of the asteroid is viewed and cool material on the night side contributes only a small amount to the infrared radiation.

ACKNOWLEDGMENTS

The author thanks Bruce C. Murray for suggestions, encouragement, and discussions throughout the course of this project. Gordon Hoover assisted with all of the observations and was indispensable to the program. A special thanks goes to the staff of the Hale Observatories for the many courtesies that they rendered. This work was supported by the National Aeronautics and Space Administration Grant NGL 05-002-003.

REFERENCES

Allen, C. W. 1963, Astrophysical Quantities. Athlone Press. London.

Allen, David A. 1790, Infrared Diameter of Vesta, Nature 227, 158-159.

Gehrels, T. 1970, Photometry of Asteroids. Surface and Interiors of Planets and Satellites (ed., Dollfus), ch. 6, pp. 317-375. Academic Press, Inc. New York.

Gehrels, T., Roemer, E., Taylor, R. C., and Zellner, B. H. 1970, Minor Planets and Related Objects. IV. Asteroid (1566) Icarus. Astron. J. 75, 186-195.

Johnson, Torrence Vano. 1970, Albedo and Spectral Reflectivity of the Galilean Satellites of Jupiter, p. 58. Ph.D. Thesis, Calif. Inst. of Tech.

Matson, Dennis L. 1971, Ph.D. Thesis, in preparation.

Smith, Bradford A. 1970, Phobos: Preliminary Results from Mariner 7. Science 168, 828-830.

Veverka, J., and Liller, W. 1969, Observations of Icarus: 1968. Icarus 10, 441-444.

Figure 1. - Phase data for 4 Vesta. The curve through the 11.6μm data is the phase function used for the reduction of the data presented in Figure 3. Errors for some of the data are less than the size of the plotted symbol. Allen's (1970) data for the same opposition have not yet been reduced to the present photometry systems.

Figure 2. - Phase data for 7 Iris. Some of the scatter is due to the lightcurve.

Figure 3. - Differential comparison of the model parameters for selected asteroids. The error bars are for the infrared photometry only. The errors in albedo and radius are correlated and lie along trajectories defined by B(1,0) = constant. Errors in B(1,0) and the phase correction are not plotted. The lightcurves appear to be responsible for much of the scatter of values for the smaller asteroids. The ordinate for the data from the literature is the Bond albedo, which is approximately equivalent to the normalized model albedo. Data for Icarus are from Gehrels et al. (1970) and Veverka and Liller (1969).

Figure 4. - Infrared flux as a qualitative function of visible flux for a rotating, spherical minor planet with uniform albedo and zero obliquity.

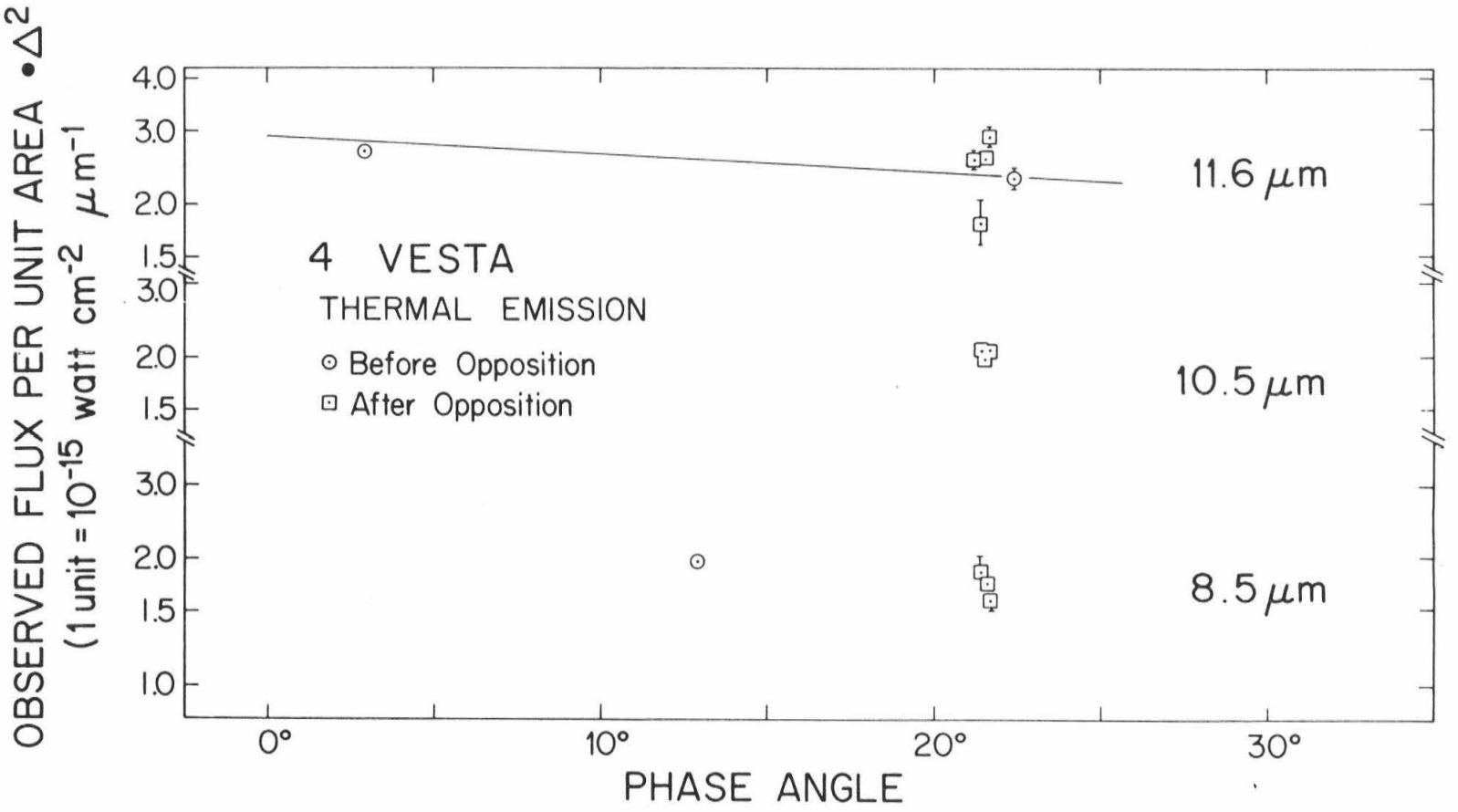
OBSERVED FLUX PER UNIT AREA • Δ²
(1 unit = 10⁻¹⁵ watt cm⁻² μm⁻¹
4.0
3.0
2.0
1.5
3.0
2.0
1.5
3.0
2.0
1.5
1.0
4 VESTA
THERMAL EMISSION
⊙ Before Opposition
⊡ After Opposition
11.6 μm
10.5 μm
8.5 μm
0°
10°
20°
30°
PHASE ANGLE

Fig. 1

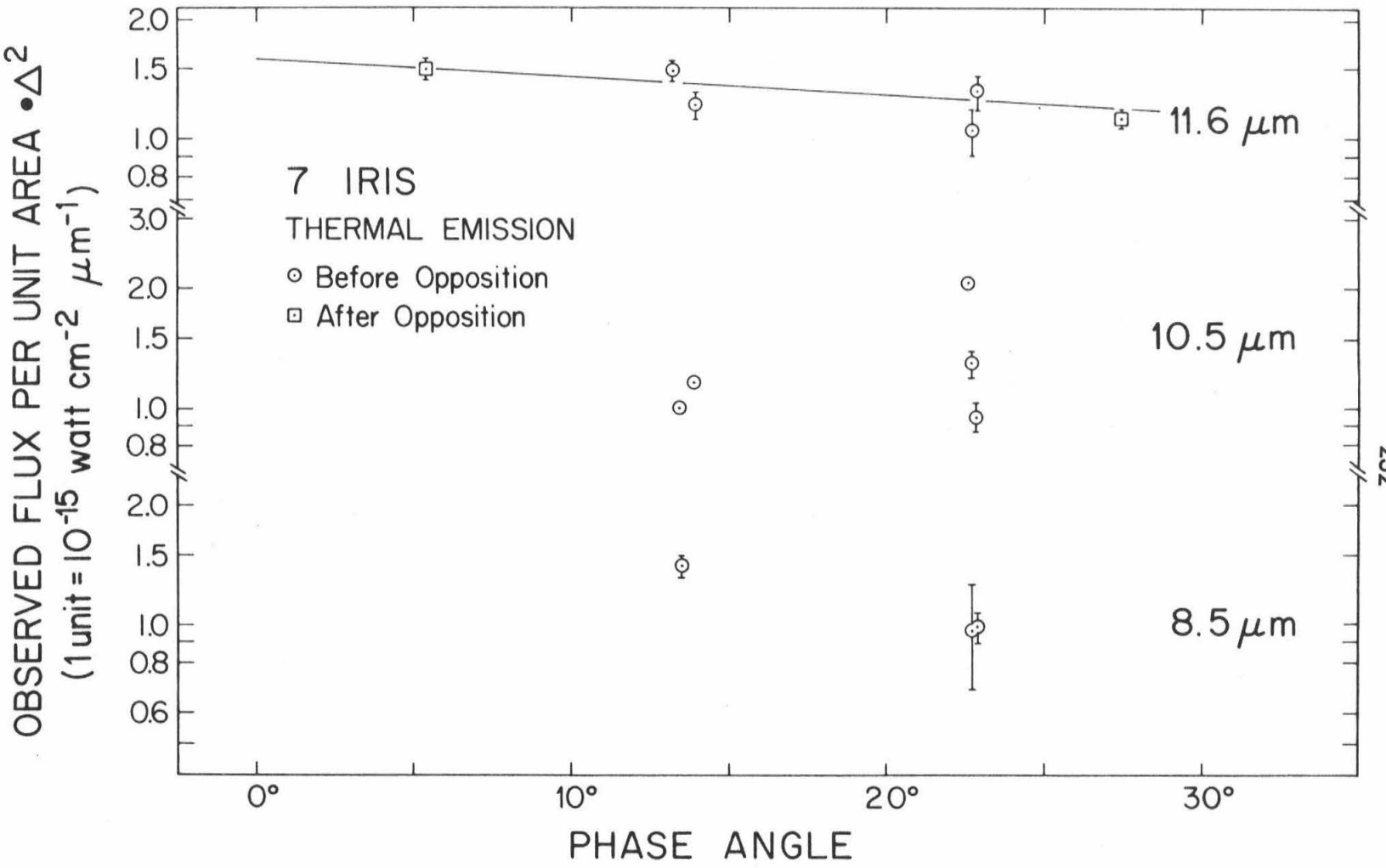
OBSERVED FLUX PER UNIT AREA •Δ²
(1 unit = 10⁻¹⁵ watt cm⁻² μm⁻¹)
7 IRIS
THERMAL EMISSION
⊙ Before Opposition
⊡ After Opposition
11.6 μm
10.5 μm
8.5 μm
PHASE ANGLE
0°
10°
20°
30°
232

Fig. 2

Fig. 3

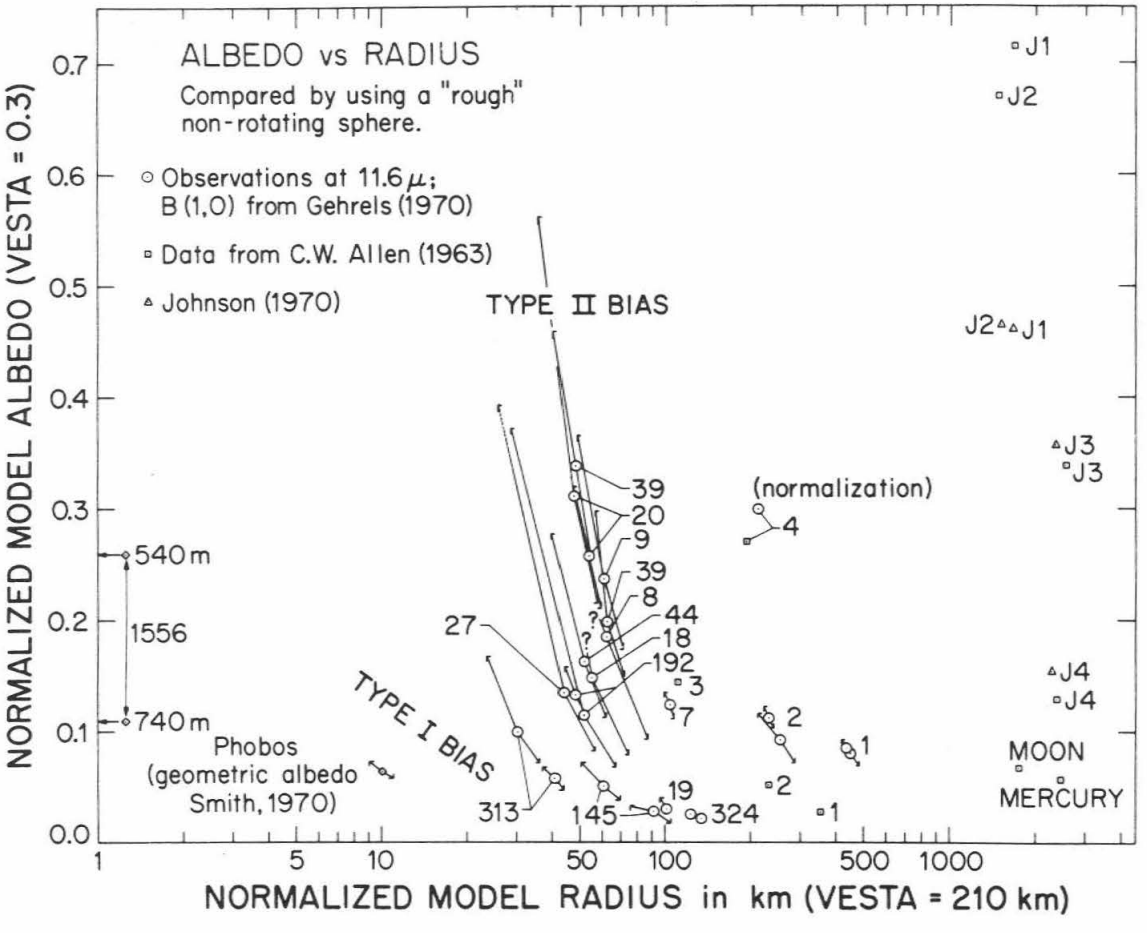
ALBEDO vs RADIUS
Compared by using a "rough" non-rotating sphere.
Observations at 11.6μ; B(1,0) from Gehrels (1970)
Data from C.W. Allen (1963)
Johnson (1970)
TYPE II BIAS
TYPE I BIAS
(normalization)
Phobos (geometric albedo Smith, 1970)
MOON
MERCURY
J1
J2
J3
J4
540 m
1556
740 m
NORMALIZED MODEL ALBEDO (VESTA = 0.3)
NORMALIZED MODEL RADIUS in km (VESTA = 210 km)

Fig. 4

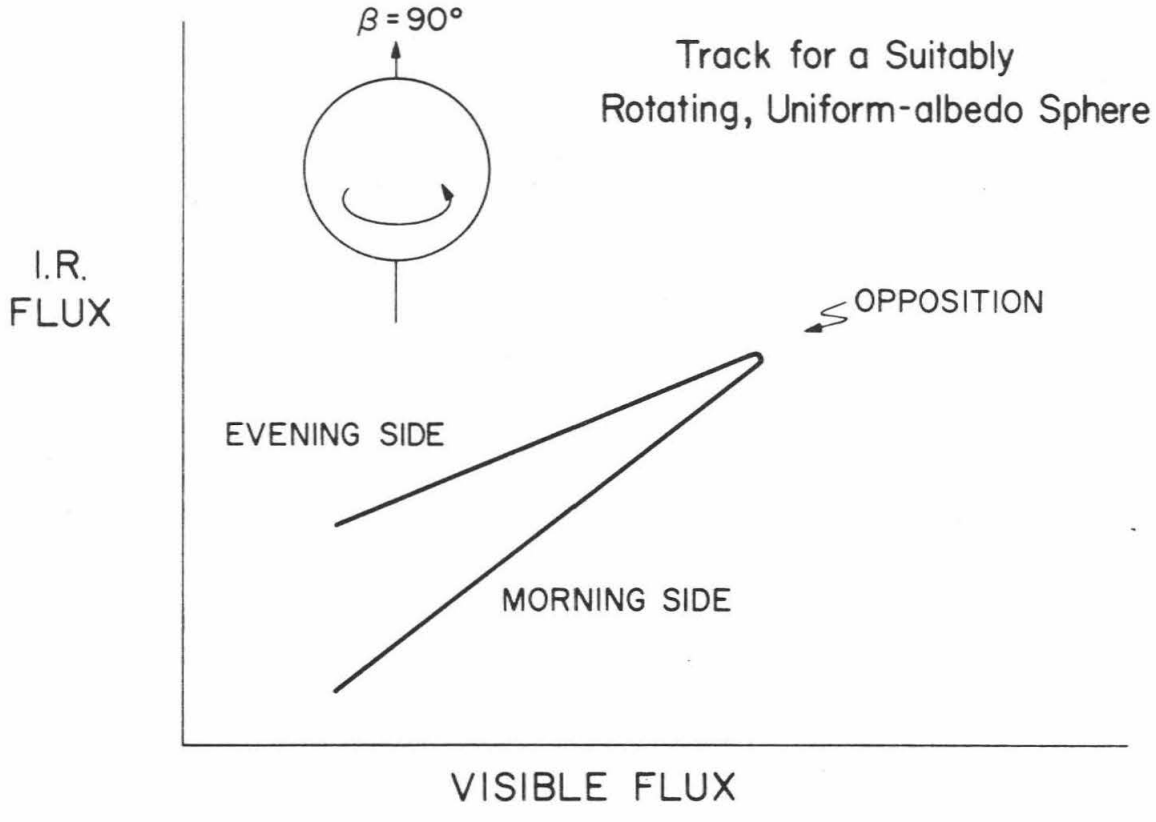
β = 90°
Track for a Suitably
Rotating, Uniform-albedo Sphere
I.R.
FLUX
OPPOSITION
EVENING SIDE
MORNING SIDE
VISIBLE FLUX

TABLE I. SIMPLE MODELS FOR 4 VESTA

Description	Method of handling temperature, T, distribution	Model albedo	Model radius, km
Flat disk	T = constant	0.13	264
Smooth, nonrotating sphere	$T = \left[\frac{(1-a)S\cos\varphi}{\sigma}\right]^{1/4}$	0.085	328
"Rough," nonrotating sphere	$T = \left[\frac{(1-a)S}{\sigma}\right]^{1/4}(\cos\varphi)^{1/6}$	0.098	306

σ = Stefan-Boltzmann constant; φ = angle between heliocentric radius vector and local surface normal; and S = solar constant at the asteroid.